

# MMS Observations of Field Line Resonances Under Disturbed Solar Wind Conditions

G. Le<sup>1</sup>, P. J. Chi<sup>2</sup>, R. J. Strangeway<sup>2</sup>, C. T. Russell<sup>2</sup>, J. A. Slavin<sup>3</sup>, B. Anderson<sup>4</sup>, R. Nakamura<sup>5</sup>,  
F. Plaschke<sup>5</sup>, R. Torbert<sup>6</sup>, and F. Wilder<sup>7</sup>

<sup>1</sup> Heliophysics Science Division, NASA Goddard Space Flight Center, Greenbelt, Maryland

<sup>2</sup> Department of Earth and Space Sciences, University of California, Los Angeles, California

<sup>3</sup> Department of Climate and Space Sciences and Engineering, University of Michigan, Ann Arbor, Michigan

<sup>4</sup> Johns Hopkins University Applied Physics Laboratory, Laurel, Maryland

<sup>5</sup> Space Research Institute, Austrian Academy of Sciences, Graz, Austria

<sup>6</sup> University of New Hampshire, Durham, New Hampshire

<sup>7</sup> Laboratory for Atmospheric and Space Physics, University of Colorado, Boulder, Colorado

Correspondence to: G. Le ([Guan.Le@nasa.gov](mailto:Guan.Le@nasa.gov))

Submitted to J. Geophys. Res. Space Physics

Paper Number 2020JA028936

## Key Points:

1. Evidence for both external and internal energy sources of FLRs under disturbed solar wind conditions
2. Characteristics of azimuthal wave numbers with different energy sources
3. Characteristic of frequency changing with L for toroidal and poloidal waves

This is the author manuscript accepted for publication and has undergone full peer review but has not been through the copyediting, typesetting, pagination and proofreading process, which may lead to differences between this version and the [Version of Record](#). Please cite this article as [doi: 10.1029/2020JA028936](https://doi.org/10.1029/2020JA028936).

This article is protected by copyright. All rights reserved.

## Abstract

We report an observational study of magnetospheric field-line resonances (FLRs) using multi-point data from the Magnetospheric Multiscale (MMS) mission. We examine well-defined FLR events in the frequency range  $\sim 2$ -10 mHz observed under disturbed solar wind conditions, such as high-speed solar wind streams and solar wind pressure pulses. We focus on their azimuthal wave numbers (m-numbers) and spatial variations of the wave frequencies; and compare their occurrence characteristics and wave properties for insights into their energy sources. Under disturbed solar wind conditions, we have found supporting observations for both external and internal energy sources for the generation of FLRs. The FLRs associated with different energy sources appear to have different wave characteristics. Although mode coupling is very common (i.e., waves generally have both toroidal and poloidal components with variable relative amplitudes), our observations show that solar wind disturbances directly drive low-m, toroidal mode dominated FLRs, but internal energy sources are inferred for high-m, poloidal mode dominated FLRs. The frequencies of the toroidal and poloidal waves have different spatial variations as a function of the L-value. The frequency of the toroidal mode waves can change continuously with L while the frequency of poloidal waves exhibits discrete spatial structure along L.

## 1. Introduction

Field line resonances (FLRs) in the magnetosphere are standing waves along the Earth's magnetic field lines. The oscillations of the magnetic field lines have two modes: the toroidal mode with azimuthal magnetic field perturbations and plasma velocity, and the poloidal mode with radial (meridional) magnetic field perturbations and plasma velocity. For toroidal mode waves, each magnetic field line can oscillate independently with its own eigenfrequency [Chen and Hasegawa, 1974; Southwood, 1974], and thus the wave frequency changes with  $L$  in the magnetosphere. For poloidal mode waves, the magnetic field lines oscillate radially in the meridian plane and need to move in sync with neighboring  $L$ -shells, and thus the wave frequency cannot change with  $L$  easily to sustain the wave power. Previous observations (mostly during quiet times) showed that poloidal mode waves could maintain nearly constant frequency across many  $L$  shells [Takahashi et al., 1987; Denton et al., 2003; Chi and Le, 2015], a feature predicted by the global poloidal mode theory [Vetoulis and Chen, 1994, 1996, Denton and Vetoulis, 1998].

Recently, we reported a storm-time high azimuthal wave number ( $m$ -number) poloidal mode FLR event which exhibited distinct frequency characteristics [Le et al., 2017]. Our multiple spacecraft/mission observations established the global extent of the wave occurrence for this storm-time FLR event, whereas high-resolution wave frequency data revealed discrete spatial structures along the  $L$  direction. Specifically, the wave frequency exhibited a general decreasing trend as a function of  $L$ , but the change of frequency occurred discretely along  $L$ . The frequency was steady within each discrete  $L$  shell. This observation clearly demonstrated the difference in the wave frequency characteristics for storm-time poloidal mode waves from the quiet time observations, implying different energy sources and generation mechanisms.

Herein we report a follow-up study of FLRs using multipoint magnetic field data from Magnetospheric Multiscale (MMS) mission, taking advantage of their unique capabilities. The focus of the study is to examine the wave properties such as the azimuthal wave number and frequency characteristics to understand FLRs generated by different energy sources. The MMS data are uniquely suitable for the study because (1) highly accurate multiple point measurements allow for direct calculation of azimuthal wave numbers for all wave events, and (2) MMS's highly elliptical orbits are ideal for studying spatial variations along L for long-lasting events.

Although the toroidal mode (as transverse Alfvén waves) and the poloidal mode (as compressional fast waves) can be independent in a uniform plasma, analytical and numerical studies indicate that the two modes are always coupled in a dipole field geometry [Kivelson and Southwood, 1985; Lee and Lysak, 1991]. This is indeed the case as we will demonstrate in our observations. Thus, our FLR wave events are identified based on wave signals in both the poloidal and toroidal components in surveying the MMS magnetic field and electric field data. The waves are thus grouped into either toroidal or poloidal events based on the dominant wave power. The toroidal events are those with the dominant wave power in the toroidal component and the poloidal events in the poloidal component.

ULF waves associated with FLRs are common in the magnetosphere. They generally occur in the Pc3-5 frequency band depending on the distance from the Earth, ranging from nearly monochromatic waves to broadband fluctuations. In this study, we focus on long-lasting, quasi-monochromatic waves in the frequency range  $\sim 2 - 10$  mHz that span at least  $3 R_E$  along L. As a controlled study, we examine the solar wind plasma and interplanetary magnetic field (IMF) conditions to determine if a potential external energy source in the solar wind can be identified, such as sudden changes in the solar wind dynamic pressure and periods of high-speed solar wind

streams (HSSWS). We also examine the geomagnetic conditions to determine if the waves occur during active periods, such as geomagnetic storms. As HSSWS event generally lasts for days, we examine the magnetospheric pre-conditions and the evolution of the wave activity following through the entire event. In this paper we present four wave events in details, three occurred during the passage of HSSWS and one under solar wind pressure pulses. We attempt to determine the source of energy for the wave generation through a detailed analysis, presented in following sections.

## **2. Observations**

### **2.1. MMS Data**

We survey the MMS magnetic field data [Russell et al., 2016] inside the magnetosphere to identify the wave events. Since the inner magnetosphere is not the primary science region of interest for the MMS mission, the instrument suite is generally operating in survey modes. For some events at larger L, the magnetic field data in fast survey mode are available. For majority of the wave intervals, the magnetic field data are in slow survey mode. Nevertheless, the magnetic field data remain to be highly accurate even in slow survey mode. The magnetic field data are sampled at 16 Hz in fast survey mode and 8 Hz in slow survey mode, that are more than adequate for the study of ULF waves with periods in a few minutes. For some events, high quality electric field data [Torbert et al., 2016] are also available. However, the particle data from MMS plasma instruments are generally not available. We focus on the observations from the magnetic and electric fields only in this study.

### **2.2. Poloidal Wave Event Observed During December 2016 HSSWS**

A long-lasting HSSWS originating from a coronal hole (CH) was observed starting on 21 December 2016, which caused a moderate geomagnetic storm [Gerontidou et al., 2018]. Figure 1 shows the 5-min resolution OMNI data for the IMF, the solar wind conditions, and the SYM-H index for 20-30 December. The HSSWS arrived at  $\sim 06$  UT on 21 December. The solar wind speed was  $\sim 400$  km/s prior to the HSSWS and reached to over 700 km/s after the arrival of HSSWS. Starting on 26 December, the solar wind speed started to decrease gradually and reached to pre-HSSWS level around 30 December. The Dst index for the moderate storm caused by the HSSWS was -52 nT at the minimum.

During this HSSWS period, the apogee of the MMS orbit was in the subsolar region, with outbound legs of the orbit passing through the dayside magnetosphere in the morning sector and inbound legs in the afternoon sector. Figure 2 shows the spectrograms of the By GSM component for inbound (left) and outbound (right) passes from 20 to 30 December (Supporting Information S1 provides the spectrograms of the other components). The two panels in the top row labeled 2016/12/20 are before the arrival of HSSWS and the rest (2016/12/21-2016/12/29) during the HSSWS period. MMS observed enhanced ULF wave activity after the arrival of HSSWS, with a variety of ULF wave activity in the dayside magnetosphere, both in the morning and afternoon sectors. The wave activity occurred in a wide frequency range (Pc1-2, Pc3-4 and Pc4-5 waves). Some wave intervals appeared to be nearly monochromatic but enhanced broadband fluctuations were almost everywhere. In the dayside morning sector during the outbound passes, the waves in the Pc4-5 band ( $\sim 10$  mHz), present before the HSSWS arrival, were greatly enhanced by the increased solar wind speed (2016/12/21 – 2016/12/26). When the solar wind speed returned to its nominal value, so did the wave intensity.

The event of interest, however, is a long interval of nearly monochromatic Pc4-5 waves (~ 5-10 mHz) in the afternoon sector during the inbound pass on 29 December (bottom left panel of Figure 2). This wave interval, highlighted in yellow in Figure 1, occurred in the late recovery phase of the small storm when the solar wind speed has decreased to its nominal value. Thus, the waves in this interval were not directly triggered or intensified by the HSSWS. It is more likely that internal plasma instabilities were at work in generating these waves.

Figure 3 is an overview of the aforementioned wave event. The top panel shows the spacecraft trajectory for 29 December with the wave interval in red. The bottom panels show the MMS magnetic field (Panels *b-d*), electric field (Panels *e-g*) and calculated Poynting flux (Panels *h-j*) for the three-hour interval encompassing the waves (1630-1930 UT). The vector data of the fields and Poynting flux are rotated into the field-aligned ( $\mu$ ), toroidal ( $\varphi$ ), and poloidal ( $\nu$ ) directions. The magnetic field ( $b_\mu$ ,  $b_\varphi$ ,  $b_\nu$ ) are detrended wave data using an 8-min window running average to remove the rapidly increasing background magnetic field as the spacecraft move inward toward the Earth, where  $b_\mu$  is along the background magnetic field direction,  $b_\nu$  radially outward and perpendicular to the background magnetic field, and  $b_\varphi$  azimuthally eastward perpendicular to both the background magnetic field and the radially outward direction. The waves occurred in ~ 1700-1910 UT, spanning a large L range along the spacecraft trajectory. It is evident that the dominant wave power was in the poloidal magnetic field component  $b_\nu$  and the azimuthal electric field component  $E_\varphi$ . The Poynting flux, calculated from the magnetic and electric field data, was mainly in the field-aligned direction, but oscillated between parallel and anti-parallel directions. The average Poynting flux (red traces) was nearly zero, confirming that these were indeed standing waves. An examination of the phase relationship between  $b_\nu$  and  $E_\varphi$  reveals that the magnetic wave lagged the electric wave by  $90^\circ$ . As the spacecraft was located

slightly north of the equator, the observed phase relationship is consistent with what we would expect for the even harmonic of standing waves [Singer et al., 1982; Takahashi et al., 2011]. They are mostly likely to be the 2<sup>nd</sup> harmonic FLRs based on the observed wave frequency in comparison with the expected eigenfrequencies based on local measurements of plasma density profiles in the inner magnetosphere [e.g., Nosé et al., 2015, Le et al., 2017].

We apply the same techniques used in Le et al. [2017] to determine the azimuthal wave number (m-number) using cross-correlation analysis and examine the spatial variation of the wave frequency using Wigner-Ville distribution. The cross-correlation analysis is the technique to measure the correlation of two time series as a function of the displacement of one relative to the other. The second time series is time-shifted to compare with the first time series to determine what time lag would result in the best match, or the maximum correlation coefficient between the two time series. Chi and Russell [2008] provide detailed discussions about Wigner-Ville Distribution (WVD) and its application to different types of ULF waves.

In Figure 4, Panel *a* shows the poloidal components of the waves from four MMS satellites. Although the spacecraft separations were very small (< 10 km) for this interval, accurate magnetic field data were able to detect very small phase shifts (time lags) of the poloidal waves between any pair of MMS satellites that are separated longitudinally. Panels *b* and *c* show the observed phase shifts as a function of longitudinally separations for two wave packets, with the least square fits in red. The estimated m-numbers for the two wave packets are found to be -244 and -314, respectively. The negative sign is for westward azimuthal wave vector, which is in the same direction of the ion drift in the inner magnetosphere.

Panels *d* and *e* are the frequency spectrograms from the Wigner-Ville Distribution (WVD) for the toroidal and poloidal waves, respectively. The WVD enables us to effectively detect



changes in the instantaneous wave frequency by providing the highest possible resolution in the time-frequency plane [Chi and Russell, 2008]. As the spacecraft moved inward from  $L \sim 8$  to  $L \sim 5$ , the toroidal and poloidal waves exhibited different changing characteristics. The frequency of the toroidal waves changed freely across L-shells (Panel *d*). But the poloidal waves had the tendency to maintain constant frequency along L, and the changes occurred discretely, similar to our previous observations [Le et al, 2017]. This is particularly true for the waves in the interval  $\sim 1700$ -1800 UT (spanning  $\sim 1.2 R_E$  in radial extent). We note that WVD spectrogram provides the best possible resolution in the time-frequency domain but at the same time inevitably includes interference components of wave energy, such as the fine cell-like patterns in the diagram. The vertical stripes in the WVD spectrograms are associated with sharp changes in the time series, which are real and tend to be strongly suppressed and smoothed in the more conventional Fourier and wavelet spectrograms. To properly interpret the WVD results with confidence, we also compared the spectrograms made by more conventional Fourier and wavelet spectrograms (not shown).

### 2.3. Toroidal Wave Event Observed During January-February 2017 HSSWS

In January 2017, multiple HSSWS originating from CHs were reported from ACE measurements of the solar wind speed [Garton et al., 2018]. Figure 5 shows the 5-min resolution OMNI data for the IMF, solar wind and geomagnetic conditions for three HSSWS starting on 18 January, following  $\sim 4$  days of slow solar wind. For the three HSSWSs, the peak solar wind speed reached over 600 km/s on 19 and 26 January and near 800 km/s on 1 February, respectively. The three HSSWS also caused strong pressure pulses with  $\sim 3$  to 4 fold increases in the solar wind dynamic pressure.

During this period, the apogee of the MMS orbit was in the morning sector shifting westward, which started at  $\sim 11$  hr local time and ended at  $\sim 9$  hr local time. The outbound leg of the orbit passed through the dayside magnetosphere in the morning sector and inbound leg close to the local noon. Figure 6 shows the spectrograms of the Bx GSM component for inbound (left) and outbound (right) passes from 17 January to 3 February (Supporting Information S2 provides the spectrograms of the other components). The two top panels (2017/01/17) are before the arrival of HSSWS and the rest are during the HSSWS period. Starting from 2<sup>nd</sup> panels from top (2017/01/18), it is evident that the HSSWS resulted in much enhanced ULF wave activity in the dayside magnetosphere. Similar to the previous case, MMS observed a variety of ULF waves, both nearly monochromatic waves and broadband fluctuations, and in wide frequency ranges (Pc1-2, Pc3-4 and Pc4-5 waves).

In the dayside morning sector, a long-lasting and narrow-band wave event appeared in the first outbound pass immediately after the arrival of the 1<sup>st</sup> HSSWS and the associated strong pressure pulse, as evident in the spectrogram for 2017/01/18 (2<sup>nd</sup> panel from top on the right in Figure 6). The waves started around  $\sim 1920$  UT and had an initial frequency  $\sim 30$  mHz. The frequency gradually decreased to Pc4-5 band as the spacecraft moved outbound towards the magnetopause. The waves lasted for more than 3 hours and the frequency decreased to  $\sim 5$  mHz in the end of the interval. The wave amplitudes were variable and appeared to be stronger in  $\sim 2030 - 2130$  UT in this pass when the geocentric distance of the spacecraft was  $\sim 5-7 R_E$ . The same narrow-band waves were present for the following 5 outbound passes (2017/01/19 – 2017/01/23), which were coincident with the entire duration of the first HSSWS (Figure 5). It is reasonable to assume that that the waves were present for the entire duration of the first HSSWS even when the spacecraft were not in the dayside morning sector. The waves were largely

weakened or nearly absent for the next two outbound passes, 2017/01/24 and 2017/01/25, when the solar wind slowed down to its nominal speed at the pre-HSSWS value. As soon as the 2<sup>nd</sup> HSSWS arrived on 2017/01/26, similar narrow-band waves were significantly enhanced again in the same region. Between the 2<sup>nd</sup> and 3<sup>rd</sup> HSSWS, there was about one day (2017/01/30) when the solar wind speed decreased to  $\sim 400$  km/s but there was a pressure pulse due to the solar wind density enhancement. Narrow-band waves were observed in every outbound pass during the 2<sup>nd</sup> and 3<sup>rd</sup> HSSWS. As examples, Figure 6 includes two passes during the 2<sup>nd</sup> HSSWS (the panels for 2017/01/26 and 2017/01/27) and two passes during the 3<sup>rd</sup> HSSWS (the panels for 2017/02/01 to 2017/02/03). Supporting Information S2 provides the spectrograms of for all passes for the entire interval. These observations clearly support the association of these long-lasting Pc 4-5 waves with the solar wind disturbances, in this case, the much-enhanced solar wind speed and some solar wind pressure pulses. In contrast to the likely internal energy source for the waves observed during the December 2016 HSSWS presented in 2.2, the energy source of these waves is most likely external.

The narrow-band waves observed in all these outbound passes occurred in the same general region in the dayside morning sector and had very similar wave properties. We now present the detailed wave analysis for two strong wave intervals observed on 2017/01/21 and 2017/02/03, respectively. These two intervals, highlighted in yellow in Figure 5, occurred during the 1<sup>st</sup> and 3<sup>rd</sup> HSSWS, respectively. Figure 7 is an overview of the two wave intervals. The top panel (panel *a*) shows the spacecraft trajectory with the wave interval in red for 2017/01/21 and blue for 2017/01/03, respectively. In the lower panels, the MMS magnetic field (b-d), electric field (e-g) and calculated Poynting flux (h-j) are shown on the left for 2017/01/21, and on the

right for 2017/02/03, respectively. Again, the vector data of the fields and Poynting flux are rotated into the field-aligned ( $\mu$ ), toroidal ( $\phi$ ), and poloidal ( $\nu$ ) directions.

For the wave interval on 2017/01/23, the solar wind velocity was  $\sim 500$  km/s. The waves occurred in  $\sim 2000$ - $2200$  UT as three wave packets spanning more than  $3 R_E$  in  $L$  along the spacecraft trajectory in the morning sector. In the lower left panels of Figure 7, it is evident that the toroidal component  $b_\phi$  had the dominant wave power and the poloidal component  $b_\nu$  was much weaker, which is very different from the December 2016 case. The field-aligned Poynting flux oscillated between parallel and anti-parallel directions; and the average Poynting flux (red traces) was insignificant in comparison with their peak values, confirming that these are standing waves. For the first wave packet ( $\sim 2000$ - $2050$  UT), the net Poynting flux was slightly negative (antiparallel to the magnetic field), so flowing into the southern hemisphere.

Figure 8 is in the same format as in Figure 4 but for the wave interval on 2017/01/21.

Panel *a* shows the poloidal components of the waves from four MMS satellites for determining the azimuthal wave number ( $m$ -number). In Panels *b* and *c*, the observed azimuthal phase shifts for the two wave packets are much smaller than those in the December 2016 event (Figure 4), although the spacecraft separations are similar in these two events. In particular for the 2<sup>nd</sup> wave packet in Panel *c*, we could not resolve any phase shift using the data with 8 Hz sampling rate, or 0.125 s time resolution. These observations indicate that the waves, predominately in toroidal mode, had very small azimuthal wave numbers, in contrast to the December 2016 poloidal event. Panels *d* and *e* of Figure 8 are the frequency spectrograms from the WVD to show the spatial variation of the instantaneous wave frequency. As the spacecraft moved outward from  $L \sim 7$  to  $L \sim 10.5$ , the frequency of the toroidal waves changed continuously across  $L$ -shells (Panel *d*), with the decreasing trend visible even within each wave packet. But the decreasing trend was not

apparent in the spectrogram of the poloidal component. The frequency of the poloidal waves (Panel *e*) maintained constant frequency within a wave packet, and the changes occurred discretely.

For the wave interval on 2020/02/03, the solar wind velocity reached over 600 km/s. As the spacecraft trajectory precessed westward, the waves were observed slightly downward in local time, as shown in the top panel of Figure 7. But the waves continued to be dominated by the toroidal wave power (lower right panels of Figure 7), which is true for all the wave intervals in other days during the entire HSSWS period. In this day, the poloidal component was even weaker and more limited spatially. The average Poynting flux is also consistent with being standing waves.

Figure 9 is also in the same format as in Figure 4 as we repeat the same analysis for the wave interval on 2017/02/03. Note that MMS had a series maneuvers to increase the spacecraft separations to  $\sim 50$  km in the end of January 2017. As a result, the spacecraft longitudinal separations for 2017/02/03 are larger in Figure 9 than those in Figure 8, but the observed azimuthal wave numbers are still similar to those in Figure 8. This observation reaffirms that toroidal-mode dominated waves have much smaller azimuthal wave numbers. Panels *d* and *e* of Figure 9 show the spatial variation of the instantaneous wave frequency for toroidal and poloidal components, respectively. The frequency of the toroidal component again changed continuously across L-shells as the spacecraft moved outward across L-shells with prominent decreasing trend (Panel *d*). However, the same decreasing trend is also visible in the poloidal component. Since this is an interval with much stronger toroidal component than poloidal component (panels *c* and *d* on the right of Figure 7), the small poloidal wave power is likely caused by the strong toroidal wave power showing up in the poloidal component, probably due to the uncertainties in

transforming the data into field-aligned coordinates. It is also likely the reason no discrete structures were detected in the poloidal component.

#### 2.4. Toroidal Wave Event Triggered by 6 November 2015 Solar Wind Pressure Pulse

We now present a toroidal wave event following a sudden increase of the solar wind dynamic pressure. Figure 10 shows the 5-min resolution OMNI data for the IMF, solar wind and geomagnetic conditions surrounding the November 2015 magnetic storm. The arrival of the storm sudden commencement (SSC),  $\sim 1815$  UT on November 6, immediately triggered ULF waves in the dayside magnetosphere (Figure 11), which clearly points to the external energy source for the wave generation.

The MMS orbit trajectory and the magnetic and electric fields observations are displayed in Figure 11, again in the same format of Figure 3. MMS was traveling inbound in the dayside afternoon sector when the waves were observed after the SSC arrival (Panel *a*). The waves generated by the SSC had both poloidal and toroidal components, but were dominated by the toroidal component of the magnetic field  $b_\phi$  (Panel *d*) and poloidal component of the electric field  $E_v$  (Panel *g*). The field-aligned Poynting flux oscillated, as expected for standing waves, but its averages were negative (antiparallel to the magnetic field) for two wave packets. Thus, the waves carried net Poynting flux poleward into the southern ionosphere as the spacecraft were located below the GSM equator.

Figure 12 is in the same format as in Figure 4 for determining the azimuthal wave number (m-number) and characterizing the change of instantaneous wave frequencies using the WVD. For both the wave packets identified in Panel *a*, we could not resolve any azimuthal phase shift using the data with 8 Hz sampling rate, or 0.125 s time resolution (Panels *b* and *c*). These

observations confirm that the waves triggered by the pressure pulses have nearly zero azimuthal wave numbers. In Panels *d* and *e*, the instantaneous frequencies of the waves exhibited similar changing profiles across L shells as in the two cases presented above. As the spacecraft moved inward across L shells from  $L \sim 8$  to  $L \sim 5$ , the frequency of the toroidal waves changed continuously across L-shells with an increasing trend clearly visible (Panel *d*), in contrast to the frequency of the poloidal waves (Panel *e*).

### 3. Summary and Discussion

In Le et al. [2017], we first reported the discrete spatial structures along L with step-like frequency changes across a wide range of L shells for a stormtime high-m poloidal FLR event. This peculiar feature distinguishes the stormtime observations from the nearly constant frequency global poloidal modes normally observed during quiet times [e.g., Takahashi et al., 1987; Chi and Le, 2015]. It is also in contrast to the frequency of toroidal FLRs which can change freely across L as each field line can oscillate independently. These observations suggest that internal plasma instability is the likely energy source since stormtime energetic particles can provide free energy to excite poloidal waves at local FLR frequency for a wide range of L shells.

To provide further evidence of contrasting characteristics of toroidal and poloidal FLRs and to establish causal relationship between the waves and different energy sources, we present in this paper a detailed study of three FLR events. All these events were observed during periods of enhanced solar wind disturbances, such as HSSWS or solar wind pressure pulses. Our observations demonstrate that the magnetosphere responds to strong solar wind forcing with a variety of ULF wave activity immediately after the arrival of solar wind disturbances. Here we

focus on the generation of FLRs in Pc 4-5 frequency range and the following is a summary of our observations.

- (1) We have found some evidence for both external and internal energy sources for the generation of FLRs under disturbed solar wind conditions. We find that the observed FLRs in some cases are directly triggered by the passage of solar wind disturbances, such as the toroidal wave events in January-February 2017 HSSWS and November 2015 pressure pulse. In other cases, such as the poloidal wave events in December 2016 HSSWS, as well as during June 2015 magnetic storm previously reported in Le et al. [2017], FLRs appear to be generated by internal plasma instability and not to be a direct response to the passage of solar wind disturbances.
- (2) The FLRs associated with different energy sources appear to have different wave characteristics. In all the cases identified as FLRs, we have confirmed their standing wave nature based on the oscillating Poynting flux along the magnetic field lines. We have also directly estimated the m-numbers using multi-point data for all these wave events to distinguish low-m and high-m waves. Although mode coupling is very common in the observed FLRs as the wave fields generally have both toroidal and poloidal components, our observations provide evidence that external solar wind disturbances trigger low-m, toroidal mode-dominated FLRs; and the poloidal mode-dominated events are generally high-m waves associated with internal plasma instabilities.
- (3) In our observations, we also demonstrate that the frequencies of the toroidal and poloidal waves have different behavior as a function of L. In all three events regardless of their energy sources, the instantaneous frequency of the toroidal



component can continuously vary across L shells, which means each field line can oscillate independently at its local resonance frequency. On the other hand, the frequency for the poloidal waves exhibits discrete structures along L and remains constant within each structure. The tendency to maintain constant frequency along L is the nature of poloidal oscillations because all field lines need to move in sync within the meridional plane.

Solar wind disturbances as external sources of magnetospheric FLRs have long been established based on in situ and ground-based observations and their theoretical interpretations. Observationally in event and statistical studies, both solar wind pressure pulses [e.g., Hudson et al., 2004; Eriksson et al., 2006; Takahashi and Ukhorskiy, 2007; Zhang et al., 2010] and Kelvin-Helmholtz (K-H) waves associated with high speed solar wind [e.g., Rae et al., 2005; Liu et al., 2009] have been identified as the energy sources.

In the first two cases with HSSWS (Figures 1 and 5) presented in this study, our observations show that FLRs were either directly triggered or significantly intensified by the HSSWS in the morning sector. In one of the two cases (December 2016, Figure 2), FLRs appeared only in the morning sector and no FLRs were observed during the period of high solar wind speed in the afternoon sector when the spacecraft's orbit cut through both the morning and afternoon sectors. This is consistent to the dawn-dusk asymmetry of K-H instability and its strong preference to the dawnside during the general Parker spiral orientation of the IMF (when IMF  $B_x$  and  $B_y$  have opposite signs) [e.g., Henry et al., 2017]. In the third case presented in this paper, the energy source of the wave is very clear. FLRs were directly triggered by the compression of the magnetosphere due to the solar wind pressure pulse. Although the

observations were made in the late afternoon sector, we expect the impact would be global as the pressure pulse front impinged on the magnetopause and propagated tailward.

On the other hand, the narrow-banded, poloidal-mode dominated FLRs observed in the afternoon sector on 29 December 2016 in the first HSSWS case are clearly not directly associated with any solar wind disturbances (the bottom left panel in Figure 2). They did not appear until after the solar wind speed returned to its nominal value. The likely mechanism for their generation is wave-particle interaction with energetic ions in the inner magnetosphere. As described in Southwood and Kivelson [1981, 1982], energetic particles in drift and bounce motion can interact resonantly with poloidal waves when the resonant condition is satisfied:  $\omega - m\omega_d = N\omega_b$ , where  $\omega$  is the wave frequency,  $m$  the azimuthal wave number,  $\omega_d$  and  $\omega_b$  the drift and bounce frequencies of the particles, respectively, and  $N$  an integer number associated with the bounce motion. In our observations, the poloidal mode waves were in the 2<sup>nd</sup> harmonic mode, and thus, their azimuthal electric field was asymmetric about the equator. The poloidal mode waves propagated westward, in the same direction of the ion drift. The resonant condition for drift instability ( $N=0$ ) or drift-bounce instability ( $N=\pm 2$ ) can be satisfied with energetic ions.

Zong et al. [2017] presented numerical solutions for the drift-bounce resonance energy of energetic particles with 10 mHz waves at L=5 (Figure 20 of Zong et al., 2017), which can be used to estimate the energy range for the resonant ions as these parameters are similar to those in our observations. For the drift resonant instability ( $N=0$ ), the westward propagating poloidal waves with  $m \sim 200-300$  would be in resonance with  $\sim 20-40$  keV protons. For the drift-bounce resonant instability, the resonant energy for the protons would be a few keV for  $N=-2$ , or  $\sim 200-400$  keV for  $N=2$ . Considering the waves occurred in a late recovery phase of a moderate storm and in the local time where the plasmaspheric plume forms, both the ring current ions ( $\sim 20-300$

keV) and plasmaspheric ions ( $\sim 1-10$  keV) are potentially available in this region, but we were not able to distinguish the two resonant mechanisms due to the lack of MMS plasma data in the inner magnetosphere.

The high- $m$  poloidal waves observed in Le et al. [2017] occurred globally in most local times, especially in the entire dayside magnetosphere, while the December 2016 poloidal wave event in this study was observed only in the inbound pass in the afternoon sector, and thus, appeared to be a local phenomenon. We note that the former waves occurred in the recovery phase of a large, long-lasting magnetic storm (minimum Dst  $\sim -207$  nT). But the storm associated with the December 2016 HSSWS was much weaker and the poloidal waves occurred near the end of the recovery phase (Figure 1). It is straightforward to think that the localized waves are caused by localized presence of the resonant particles. But the globally observed waves can be due to the presence of resonant particles in all these local times along the particle drift paths or/and the wave propagation from a localized source region with sustaining particle injections. For the globally observed poloidal waves in Le et al. [2017], the strongest waves were observed in the dusk and post-dusk sector, which is the same location energetic ions are injected into their drift paths and a strong partial ring current arises in the development of a strong storm. Understanding the conditions that control the longitudinal extent of the poloidal waves can provide more insights into the particle dynamics and wave-particle interactions, which will be a topic of our next follow-up study.

#### **4. Conclusions**

In this study, we examine nearly monochromatic, long-lasting FLR events observed under disturbed solar wind conditions, such as high-speed solar wind streams and solar wind pressure

pulse, and have found supporting evidence for both external and internal energy sources for the generation of FLRs. The FLRs associated with different energy sources appear to have different wave characteristics. Although mode coupling is very common (i.e., waves generally have both toroidal and poloidal components with variable relative amplitudes), our observations show that solar wind disturbances directly trigger low- $m$ , toroidal mode dominated FLRs. On the other hand, poloidal mode dominated FLRs with high  $m$  number are not directly associated with the enhanced solar wind speed, suggesting they have internal energy sources. The likely generation mechanism is the drift resonance or drift-bounce resonance with the ions in the inner magnetosphere. The frequencies of the toroidal and poloidal waves have different spatial variations as a function of the  $L$ -value. The frequency of the toroidal mode dominated waves can change continuously with  $L$  while the poloidal waves exhibit discrete spatial structure along  $L$ .

### **Data Availability Statement**

The MMS data are publicly available at the MMS Science Data Center at University of Colorado, <https://lasp.colorado.edu/mms/sdc/public/>. They are also available at the Coordinated Data Analysis Web (CDAWeb) at NASA Goddard Space Flight Center Space Physics Data Facility, <https://cdaweb.gsfc.nasa.gov/index.html/>. The IMF and solar wind data, as well as geomagnetic indices are available at the OMNIWeb at NASA Goddard Space Flight Center Space Physics Data Facility, <https://omniweb.gsfc.nasa.gov>.

### **References**

Chen, L., and A. Hasegawa (1974), A theory of long-period magnetic pulsations, 1. Steady state excitation of field line resonance, *J. Geophys. Res.*, 79(7), 1024-1032.

<https://doi.org/10.1029/JA079i007p01024>

Chi, P. J., and C. T. Russell (2008), Use of the Wigner-Ville distribution in interpreting and identifying ULF waves in triaxial magnetic records, *J. Geophys. Res.*, 113, A01218.

<https://doi.org/10.1029/2007JA012469>

Chi, P. J., and G. Le (2015), Observations of magnetospheric high-m poloidal waves by ST-5 satellites in low Earth orbit during geomagnetically quiet times. *J. Geophys. Res. Space Physics*, 120, 4776–4783. <https://doi.org/10.1002/2015JA021145>

Denton, R. E., and G. Vetoulis (1998), Global poloidal mode, *J. Geophys. Res.*, 103(A4), 6729–6739. <https://doi.org/10.1029/97JA03594>

Denton, R. E., M. R. Lessard, and L. M. Kistler (2003), Radial localization of magnetospheric guided poloidal Pc 4-5 waves, *J. Geophys. Res.*, 108(A3), 1105.

<https://doi.org/10.1029/2002JA009679>

Eriksson, P. T. I., L. G. Blomberg, S. Schaefer, and K.-H. Glassmeier (2006), On the excitation of ULF waves by solar wind pressure enhancements, *Ann. Geophys.*, 24, 3161-3172.

<https://doi.org/10.5194/angeo-24-3161-2006>

Garton, T. M., S. A. Murray, and P. T. Gallagher (2018), Expansion of high-speed solar wind streams from coronal holes through the inner heliosphere, *The Astrophysical Journal Letters*, 869:L12 (6pp).

<https://doi.org/10.3847/2041-8213/aaf39a>

Gerontidou, M., H. Mavromichalaki, and T. Daglis (2018), High-speed solar wind streams and geomagnetic storms during solar cycle 24, *Solar Phys.* **293**, 131.

<https://doi.org/10.1007/s11207-018-1348-8>

Henry, Z. W., Nykyri, K., Moore, T. W., Dimmock, A. P., & Ma, X. (2017). On the dawn-dusk asymmetry of the Kelvin-Helmholtz instability between 2007 and 2013. *Journal of Geophysical Research: Space Physics*, 122, 11,888–11,900.

<https://doi.org/10.1002/2017JA024548>

Hudson, M. K., R. E. Denton, M. R. Lessard, E. G. Miftakhova, and R. R. Anderson (2004), A study of Pc-5 UFL oscillations, *Ann. Geophys.*, 22, 289-302.

<https://doi.org/10.5194/angeo-22-289-2004>

Kivelson, M. G., and D. J. Southwood (1985), Resonant ULF waves: A new interpretation, *Geophys. Res. Lett.*, 12(1), 49-52. <https://doi.org/10.1029/GL012i001p00049>

Le, G., et al. (2017), Global observations of magnetospheric high-m poloidal waves during the 22 June 2015 magnetic storm, *Geophys. Res. Lett.*, 44, 3456–3464.

<https://doi.org/10.1002/2017GL073048>.

Lee, D.-H., and R. L. Lysak (1991), Impulsive excitation of ULF waves in the three-dimensional dipole model: The initial results, *J. Geophys. Res.*, 96(A3), 3479-3486.

<https://doi.org/10.1029/90JA02349>

Liu, W., T. E. Sarris, X. Li, S. R. Elkington, R. Ergun, V. Angelopoulos, J. Bonnell, and K. H. Glassmeier (2009), Electric and magnetic field observations of Pc4 and Pc5 pulsations in the inner magnetosphere: A statistical study, *J. Geophys. Res.*, 114, A12206.

<https://doi.org/10.1029/2009JA014243>

Nosé, M., et al. (2015), Formation of the oxygen torus in the inner magnetosphere: Van Allen Probes observations, *J. Geophys. Res. Space Physics*, 120, 1182–1196.

<https://doi.org/10.1002/2014JA020593>

Rae, I. J., et al. (2005), Evolution and characteristics of global Pc5 ULF waves during a high solar wind speed interval, *J. Geophys. Res.*, 110, A12211.

<https://doi.org/10.1029/2005JA011007>

Russell, C. T., et al. (2016), The Magnetospheric Multiscale magnetometers, *Space Sci. Rev.*, 199, 189–256. <https://doi.org/10.1007/s11214-014-0057-3>

Singer, H. J., W. J. Hughes, and C. T. Russell (1982), Standing hydromagnetic waves observed by ISEE 1 and 2: Radial extent and harmonic, *J. Geophys. Res.*, 87(A5), 3519–3529.

<https://doi.org/10.1029/JA087iA05p03519>

Southwood, D. J. (1974), Some features of field line resonances in the magnetosphere, *Planet. Space Sci.*, 22, 483-491. [https://doi.org/10.1016/0032-0633\(74\)90078-6](https://doi.org/10.1016/0032-0633(74)90078-6)

Southwood, D. J., and M. G. Kivelson (1981), Charged particle behavior in low-frequency geomagnetic pulsations: 1. Transverse waves. *J. Geophys. Res.* 86, 5643–5655.

<https://doi.org/10.1029/JA086iA07p05643>

Southwood, D. J., and M. G. Kivelson (1982), Charged particle behavior in low-frequency geomagnetic pulsations: 2. Graphical approach. *J. Geophys. Res.* 87, 1707–1710.

<https://doi.org/10.1029/JA087iA03p01707>

Takahashi, K., and A. Y. Ukhorskiy (2007), Solar wind control of Pc5 pulsation power at geosynchronous orbit, *J. Geophys. Res.* 112, A11205.

<https://doi.org/10.1029/2007JA012483>

Takahashi, K., J. F. Fennell, E. Amata, and P. R. Higbie (1987), Field-aligned structure of the storm time Pc 5 wave of November 14–15, 1979, *J. Geophys. Res.*, 92(A6), 5857–5864.

<https://doi.org/10.1029/JA092iA06p05857>

Takahashi, K., K.-H. Glassmeier, V. Angelopoulos, J. Bonnell, Y. Nishimura, H. J. Singer, and C. T. Russell (2011), Multisatellite observations of a giant pulsation event, *J. Geophys. Res.*, 116, A11223. <https://doi.org/10.1029/2011JA016955>

Torbert, R.B., C. T. Russell, M. Magnes, *et al.* (2016), The FIELDS Instrument Suite on MMS: Scientific Objectives, Measurements, and Data Products. *Space Sci Rev* **199**, 105–135. <https://doi.org/10.1007/s11214-014-0109-8>

Vetoulis, G. and Chen, L. (1994), Global structures of Alfvén-ballooning modes in magnetospheric plasmas. *Geophys. Res. Lett.*, 21: 2091–2094. <https://doi.org/10.1029/94GL01703>

Vetoulis, G., and L. Chen (1996), Kinetic theory of geomagnetic pulsations: 3. Global analysis of drift Alfvén-ballooning modes, *J. Geophys. Res.*, 101(A7), 15441–15456. <https://doi.org/10.1029/96JA00494>

Zhang, X. Y., Q.- G. Zong, Y. F. Wang, H. Zhang, L. Xie, S. Y. Fu, C. J. Yuan, C. Yue, B. Yang, and Z. Y. Pu (2010), ULF waves excited by negative/positive solar wind dynamic pressure impulses at geosynchronous orbit, *J. Geophys. Res.*, 115, A10221. <https://doi.org/10.1029/2009JA015016>

Zong, Q., R. Rankin, and X. Zhou (2017), The interaction of ultra-low-frequency pc3-5 waves with charged particles in Earth's magnetosphere, *Rev. Mod. Plasma Phys.* **1**, 10. <https://doi.org/10.1007/s41614-017-0011-4>



## Figure Captions

Figure 1. The 5-min resolution OMNI data for the IMF, the solar wind conditions, and the SYM-H index for 20-30 December 2016.

Figure 2. Spectrograms of the  $B_y$  GSM component for inbound (left) and outbound (right) passes from 20 to 30 December 2016.

Figure 3. An overview of the poloidal wave event on 29 December 2016, (a) The spacecraft trajectory with the wave interval in red, (b-d) the wave magnetic field, (e-g) electric field, and (h-j) the calculated Poynting flux for the three-hour interval encompassing the waves (1630-1930 UT).

Figure 4. (a) The poloidal component of the poloidal wave event on 29 December 2016 from the four MMS spacecraft. (b-c) The observed phase shifts as a function of longitudinal separations for the two wave packets. The red lines are least square fits. (d-e) The spectrograms from the Wigner-Ville Distribution (WVD) for the toroidal and poloidal waves, respectively.

Figure 5. The 5-min resolution OMNI data for the IMF, the solar wind conditions, and the SYM-H index from 16 January to 14 February 2017.

Figure 6. Selected spectrograms of the  $B_x$  GSM component for inbound (left) and outbound (right) passes from 17 January to 3 February 2017.

Figure 7. An overview of the toroidal wave event on 21 January 2017, (a) the spacecraft trajectory with the wave interval in red, (b-d) the wave magnetic field, (e-g) the electric field, and (h-j) the calculated Poynting flux for the three-hour interval encompassing the waves (1930 - 2230 UT).

Figure 8. (a) The poloidal component of the toroidal wave event on 21 January 2017 from the four MMS spacecraft. (b-c) The observed phase shifts as a function of longitudinally separations for the two wave packets. The red lines are least square fits. (d-e) The spectrograms from the Wigner-Ville Distribution (WVD) for the toroidal and poloidal waves, respectively.

Figure 9. (a) The poloidal component of the toroidal wave event on 3 February 2017 from the four MMS spacecraft. (b-c) The observed phase shifts as a function of longitudinally separations for the two wave packets. The red lines are least square fits. (d-e) The spectrograms from the Wigner-Ville Distribution (WVD) for the toroidal and poloidal waves, respectively.

Figure 10. The 5-min resolution OMNI data for the IMF, the solar wind conditions, and the SYM-H index for 6-8 November 2015.

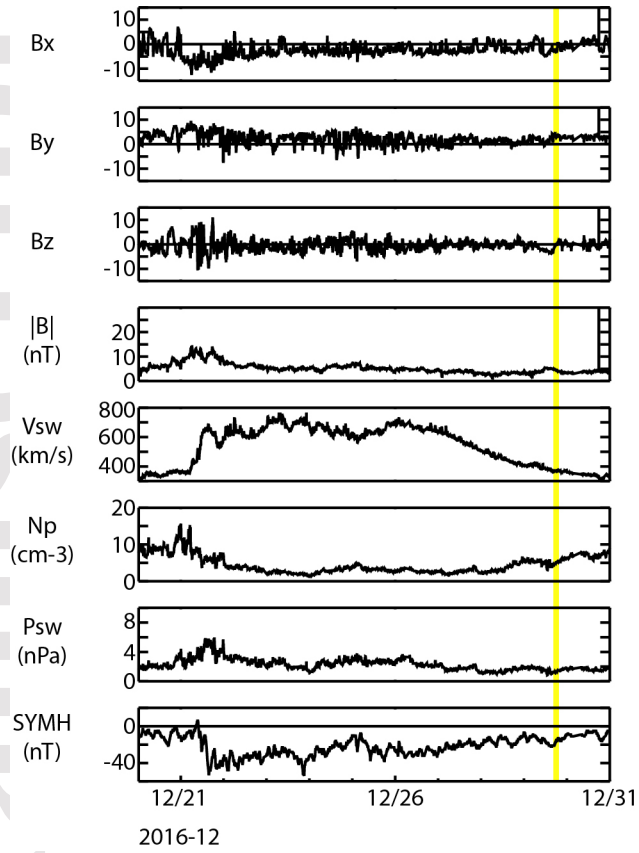
Figure 11. An overview of the toroidal wave event on 6 November 2015, (a) the spacecraft trajectory with the wave interval in red, (b-d) the wave magnetic field, (e-g) the electric field, and (h-j) the calculated Poynting flux for the three-hour interval encompassing the waves (1800-2100 UT).

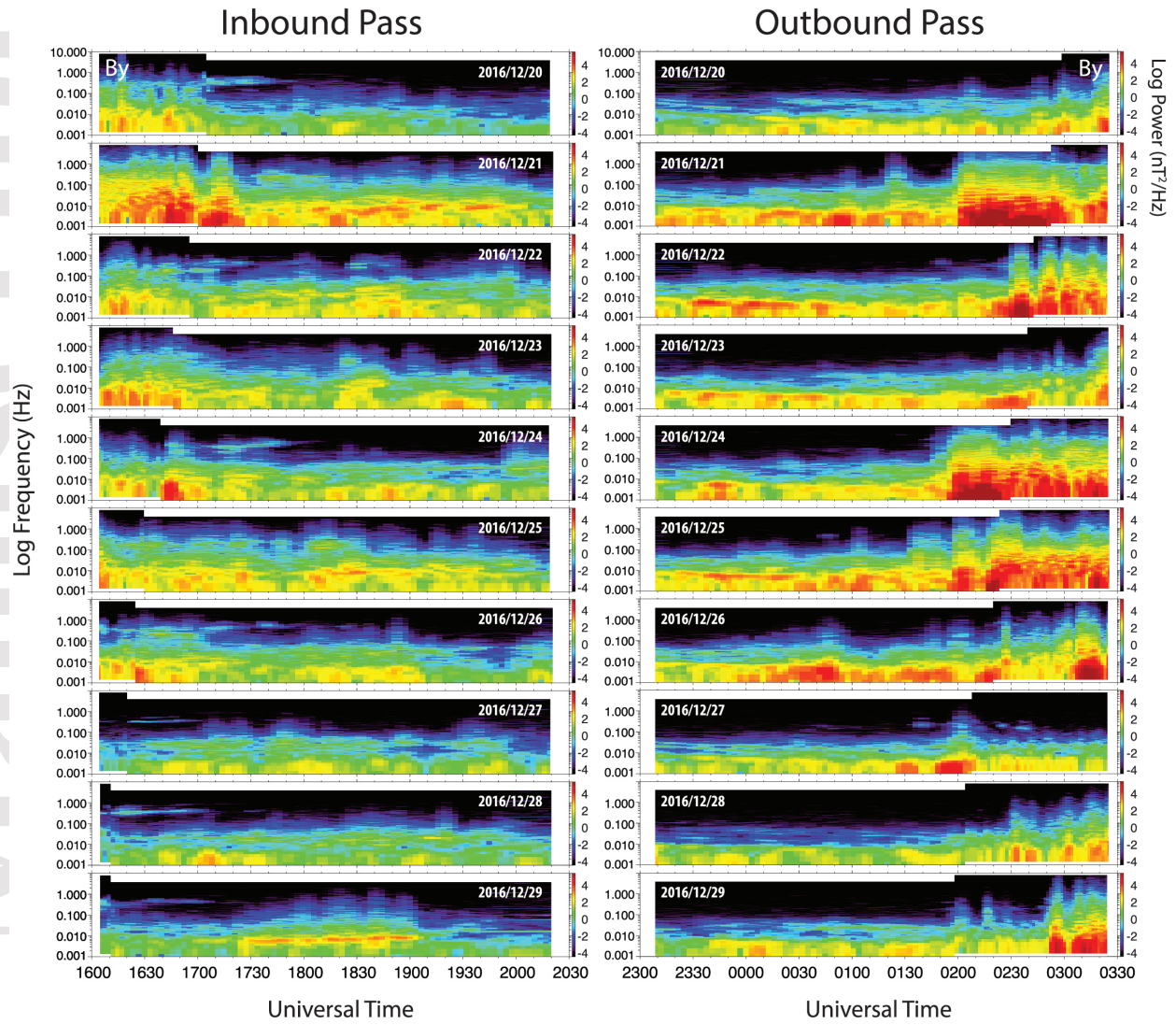
Figure 12. (a) The poloidal component of the toroidal wave event on 6 November 2015 from the four MMS spacecraft. (b-c) The observed phase shifts as a function of longitudinally separations for the two wave packets. The red lines are least square fits. (d-e) The spectrograms from the Wigner-Ville Distribution (WVD) for the toroidal and poloidal waves, respectively.

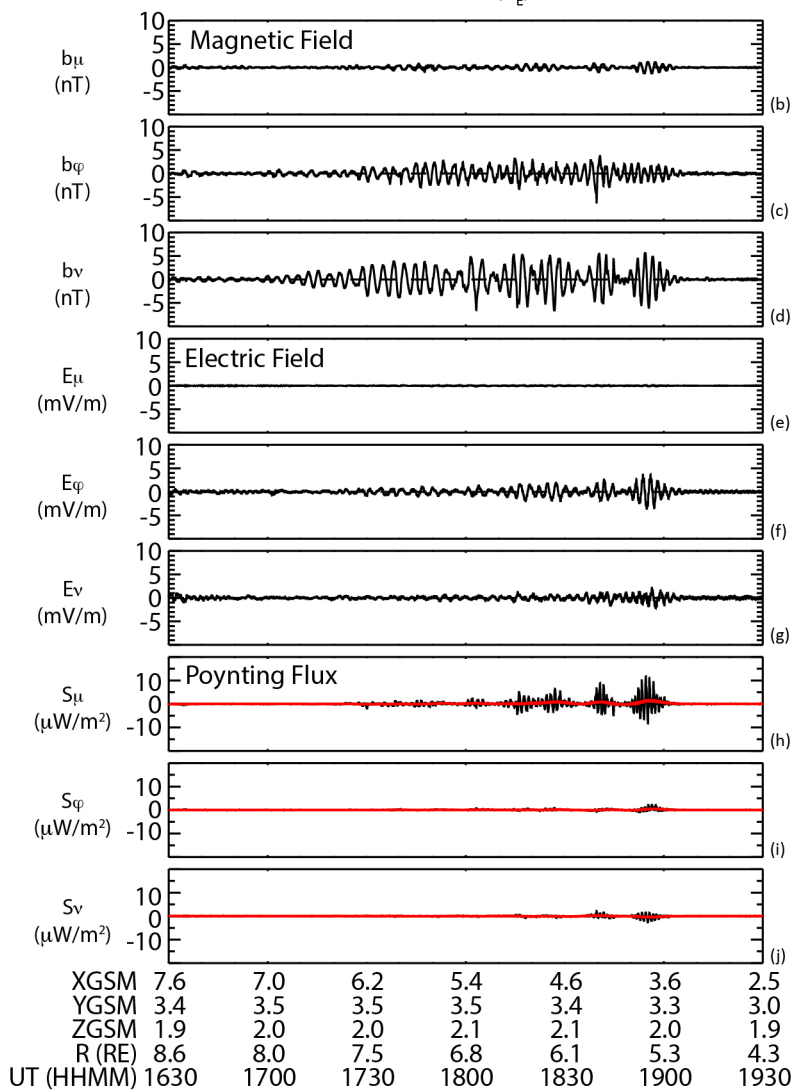
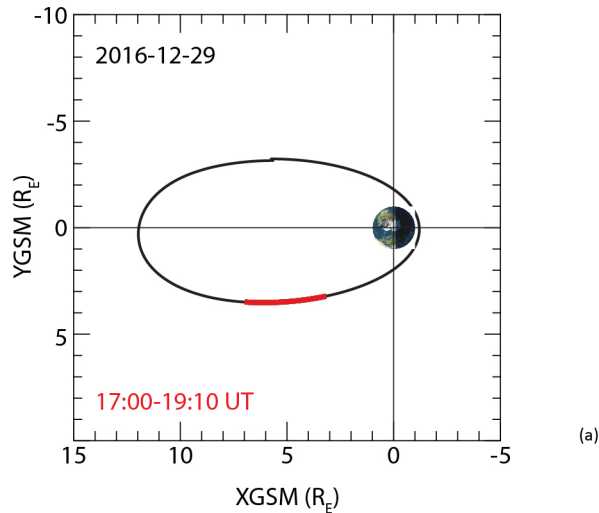
Supporting Material S1: The first page shows the MMS-1 spacecraft orbits in the GSM XY plane for the time period from 0000 UT 20 December 2016 to 0330 UT 30 December 2016.

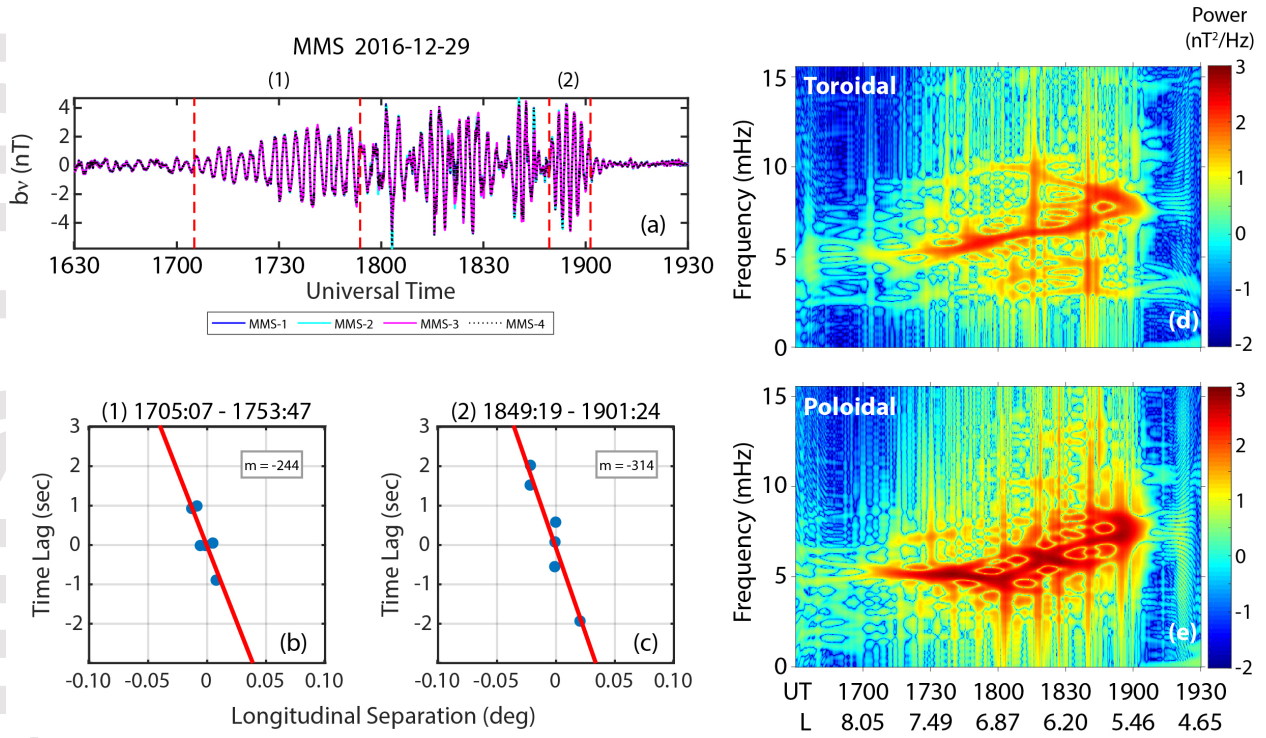
The spacecraft orbit period was approximately 1 day in this mission phase. The rest of the pages show the dynamic power spectra of the magnetic field components ( $b_x$ ,  $b_y$ ,  $b_z$ ) and the field strength ( $b_t$ ) for inbound and outbound passes. The colored orbit segments in the orbit plot correspond to the inbound (red) and outbound (magenta) time intervals displayed in these pages. The horizontal labels are the spacecraft position ( $X_{GSM}$ ,  $Y_{GSM}$ ,  $Z_{GSM}$ ) in  $R_E$ , the radial distance in  $R_E$ , and Universal Time (UT), respectively.

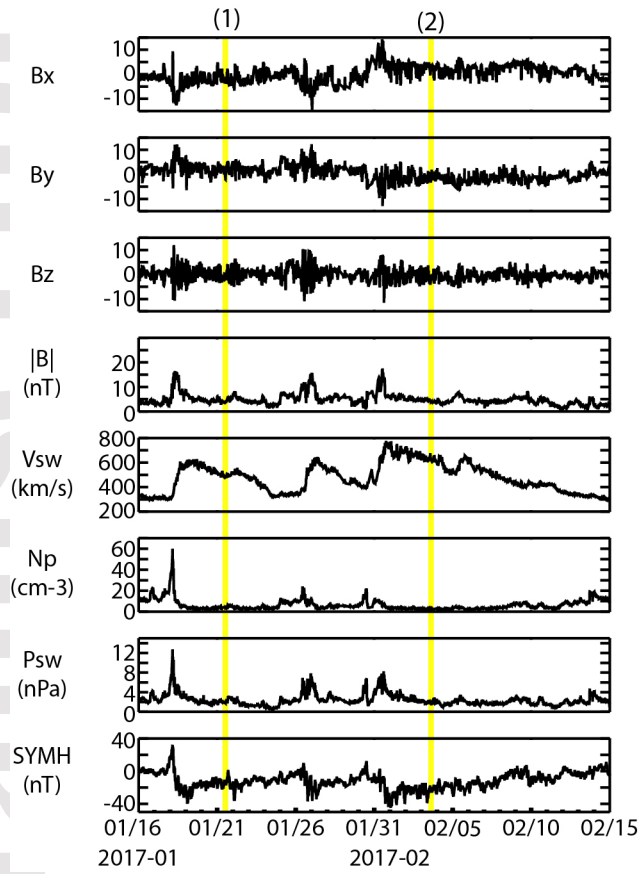
Supporting Material S2. The first page shows the MMS-1 spacecraft orbits in the GSM XY plane for the time period from 0000 UT 17 January 2017 to 2400 UT 4 February 2017. The spacecraft orbit period was approximately 1 day in this mission phase. The rest of the pages show the dynamic power spectra of the magnetic field components ( $b_x$ ,  $b_y$ ,  $b_z$ ) and the field strength ( $b_t$ ) for inbound and outbound passes. The colored orbit segments in the orbit plot correspond to the inbound (red) and outbound (magenta) time intervals displayed in these pages. The horizontal labels are the spacecraft position ( $X_{GSM}$ ,  $Y_{GSM}$ ,  $Z_{GSM}$ ) in  $R_E$ , the radial distance in  $R_E$ , Universal Time (UT), respectively.



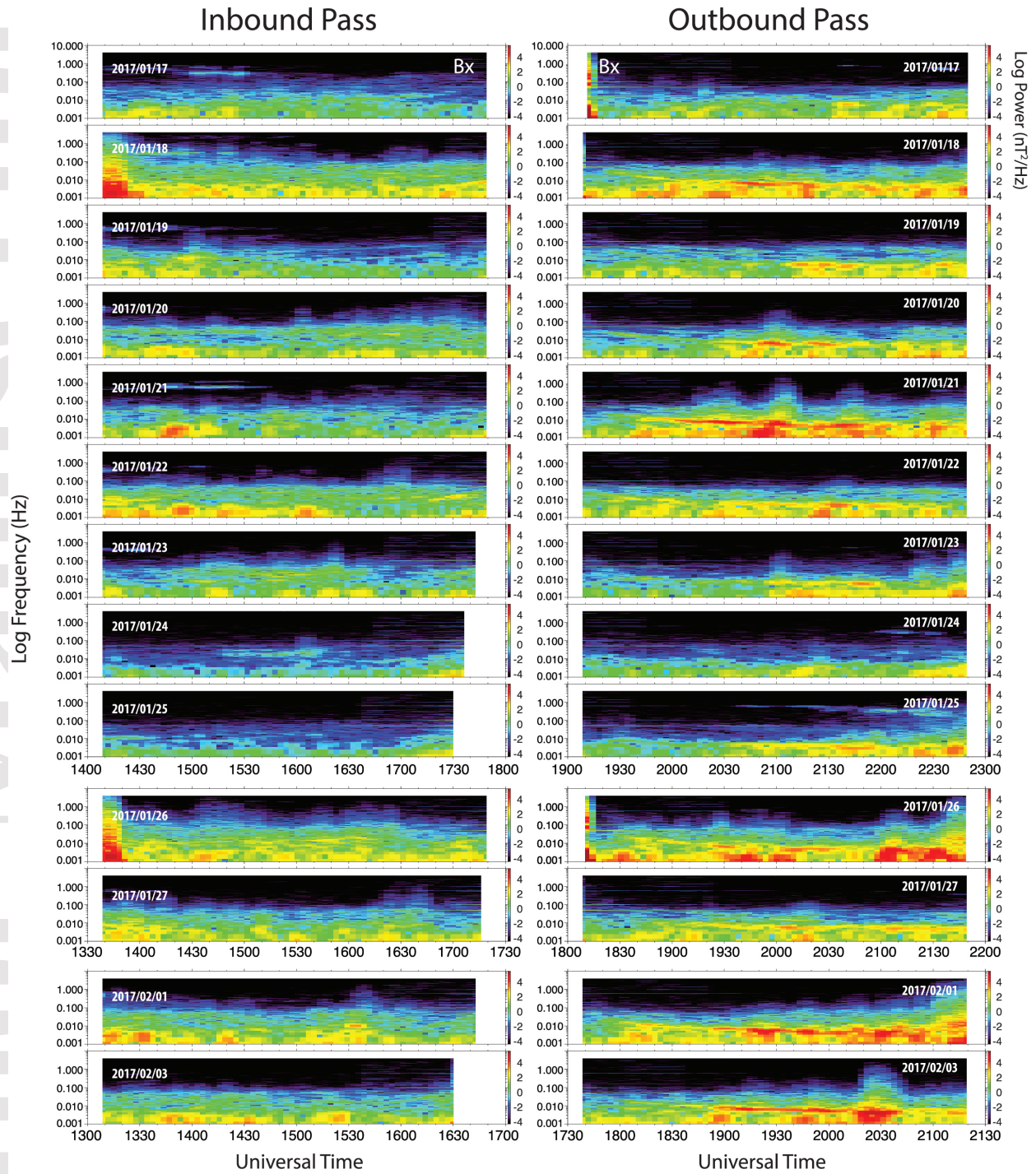


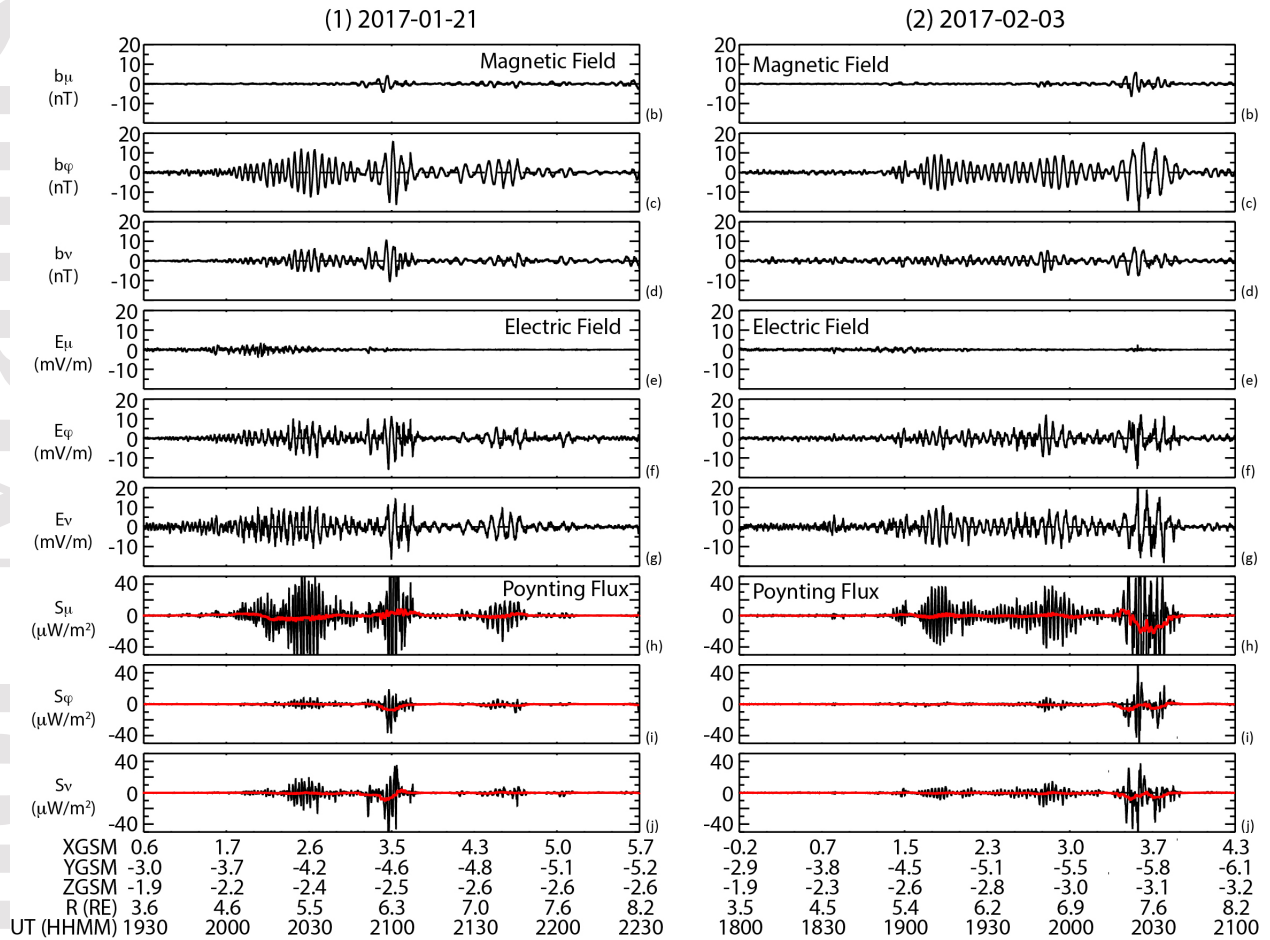
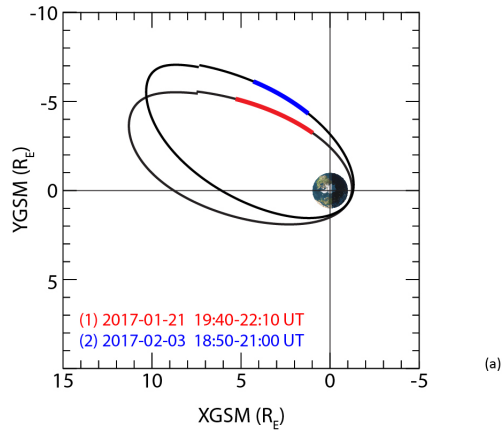


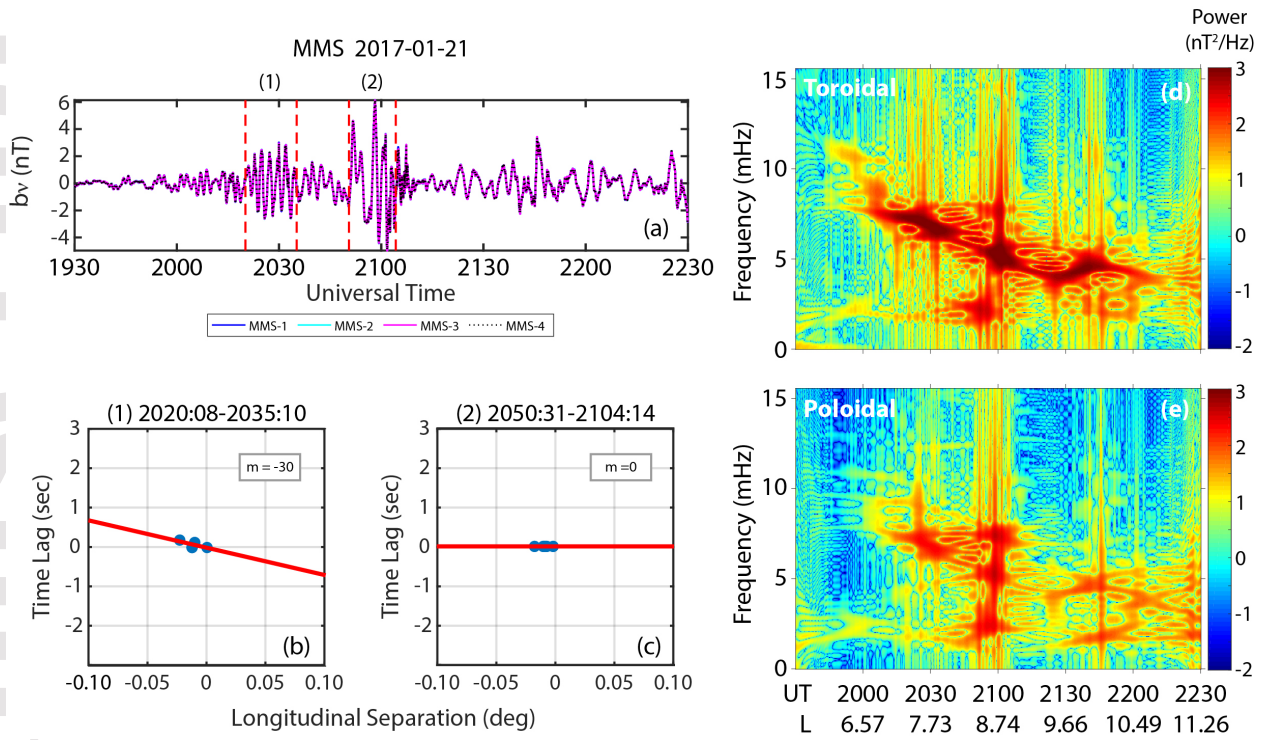


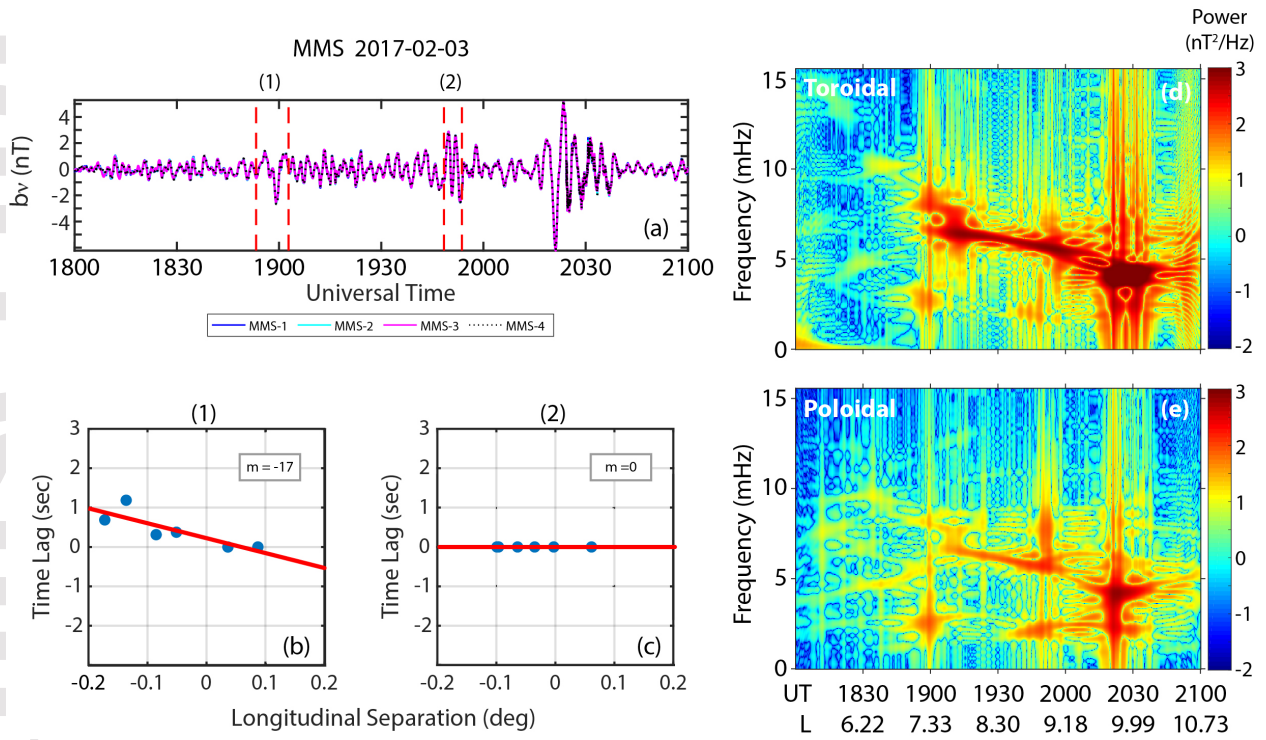


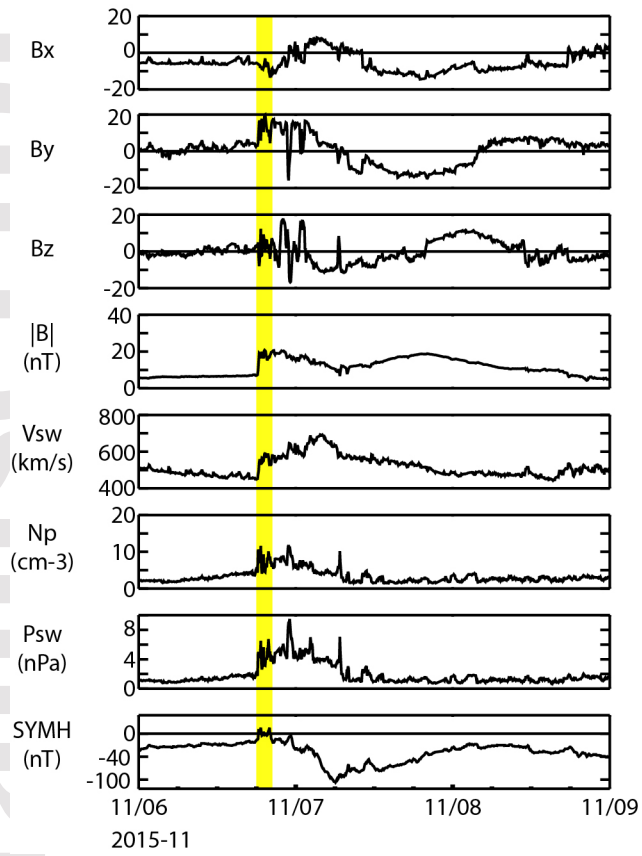


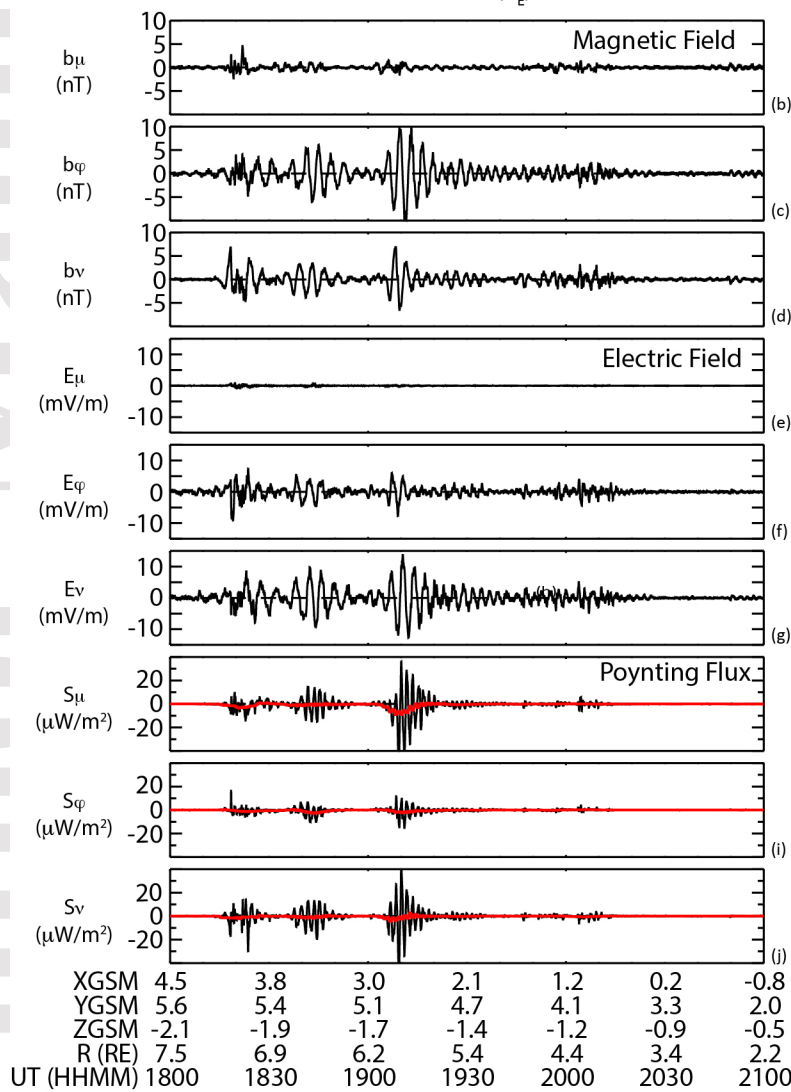
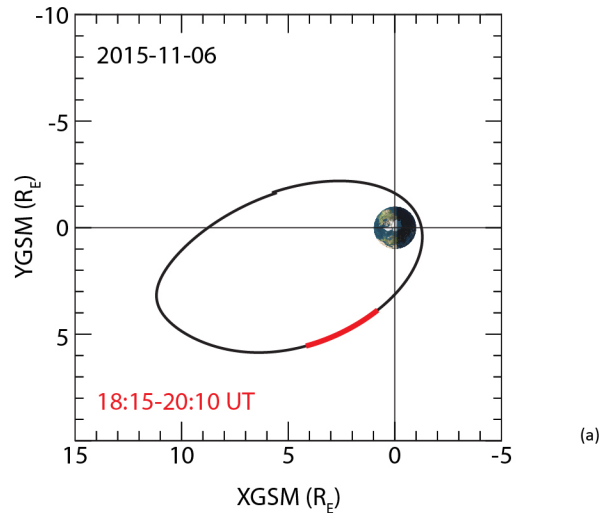


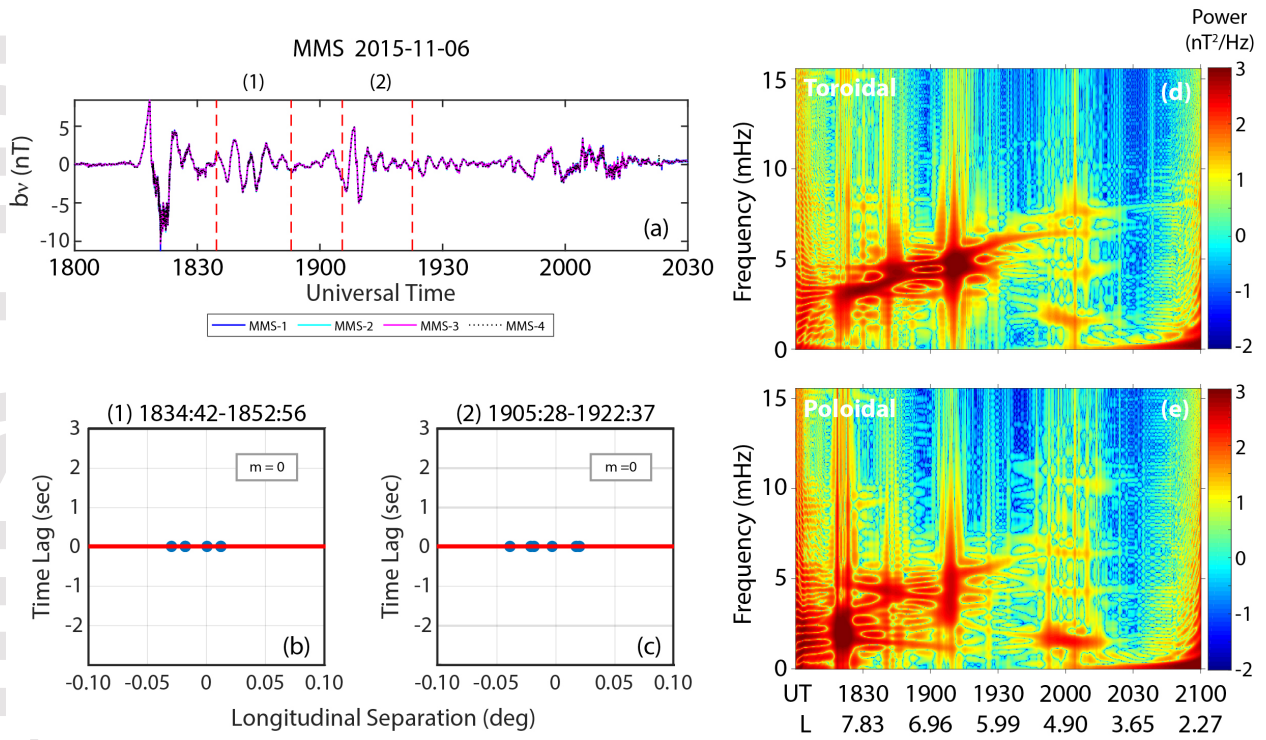












**MMS Observations of Field Line Resonances Under Disturbed Solar Wind Conditions**

Le<sup>1</sup>, P. J. Chi<sup>2</sup>, R. J. Strangeway<sup>2</sup>, C. T. Russell<sup>2</sup>, J. A. Slavin<sup>3</sup>, B. Anderson<sup>4</sup>, R. Nakamura<sup>5</sup>, F. Plaschke<sup>5</sup>, R. Torbert<sup>6</sup>, and F. Wilder<sup>7</sup>

<sup>1</sup> Heliophysics Science Division, NASA Goddard Space Flight Center, Greenbelt, Maryland

<sup>2</sup> Department of Earth and Space Sciences, University of California, Los Angeles, California

<sup>3</sup> Department of Climate and Space Sciences and Engineering, University of Michigan, Ann Arbor, Michigan

<sup>4</sup> Johns Hopkins University Applied Physics Laboratory, Laurel, Maryland

<sup>5</sup> Space Research Institute, Austrian Academy of Sciences, Graz, Austria

<sup>6</sup> University of New Hampshire, Durham, New Hampshire

<sup>7</sup> Laboratory for Atmospheric and Space Physics, University of Colorado, Boulder, Colorado

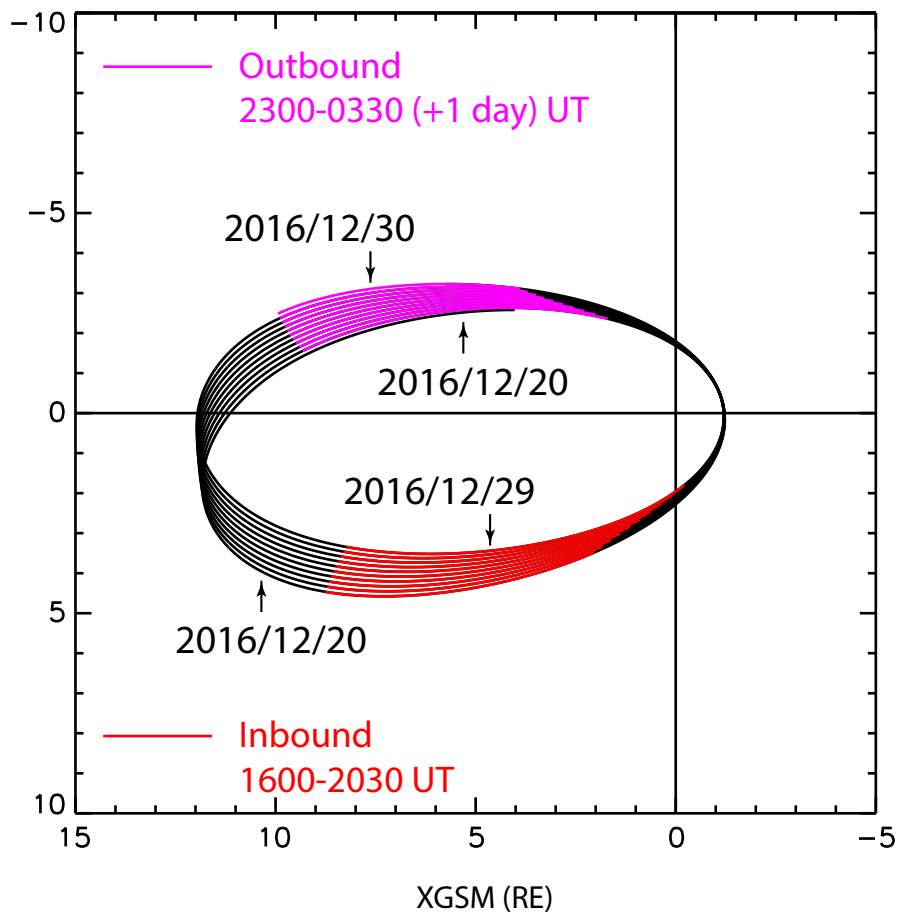
**Contents of this file**

Figure S1

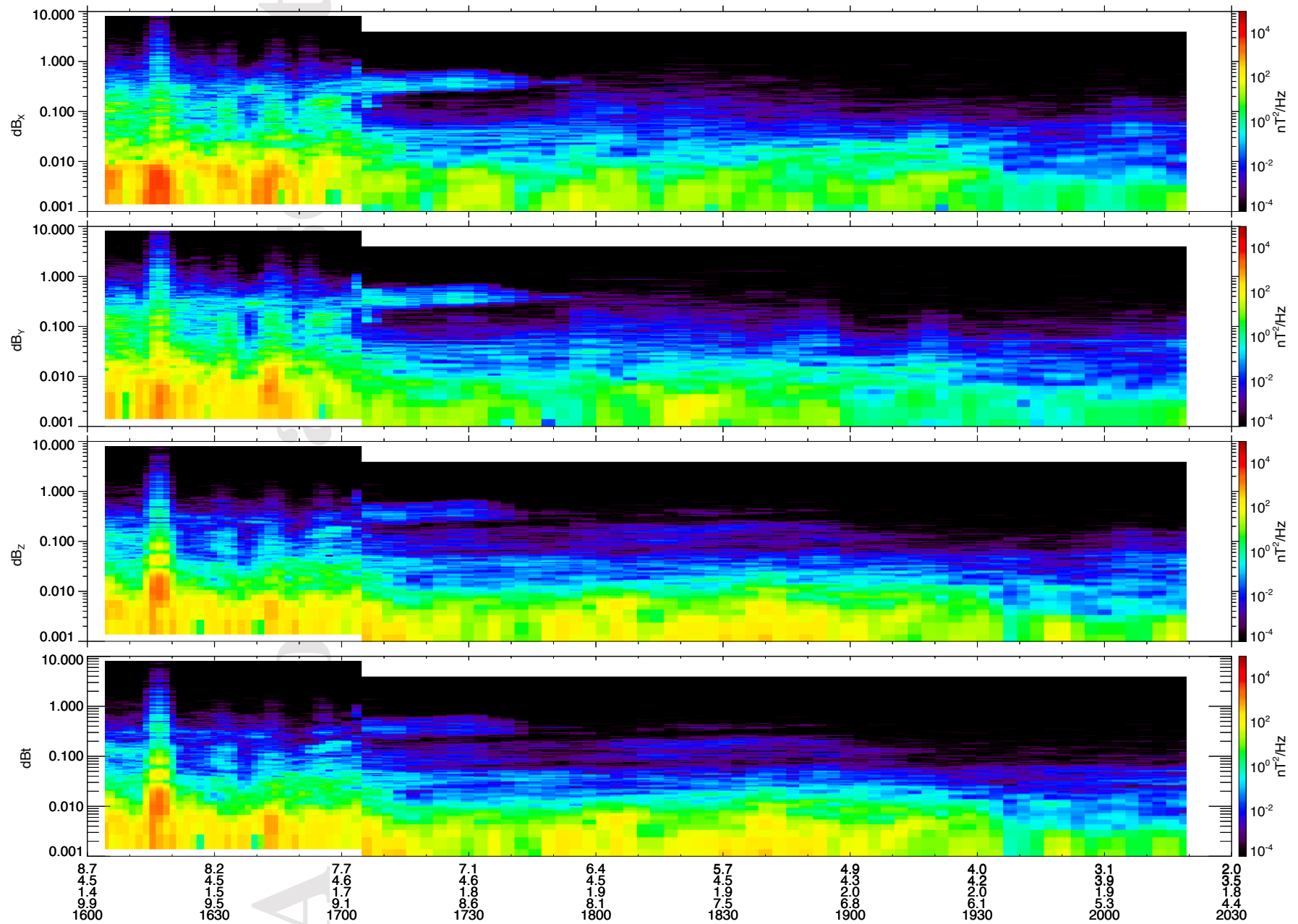
**Introduction**

**Figure S1** provides supporting information to Figures 2. The first page shows the MMS-1 spacecraft orbits in the GSM XY plane for the time period from 0000 UT 20 December 2016 to 0330 UT 30 December 2016. The spacecraft orbit period was approximately 1 day in this mission phase. The rest of the pages show the dynamic power spectra of the magnetic field components ( $b_x$ ,  $b_y$ ,  $b_z$ ) and the field strength ( $b_t$ ) for inbound and outbound passes. The colored orbit segments in the orbit plot correspond to the inbound (red) and outbound (magenta) time intervals displayed in these pages. The horizontal labels are the spacecraft position (XGSM, YGSM, ZGSM) in RE, the radial distance in RE, and Universal Time (UT), respectively.

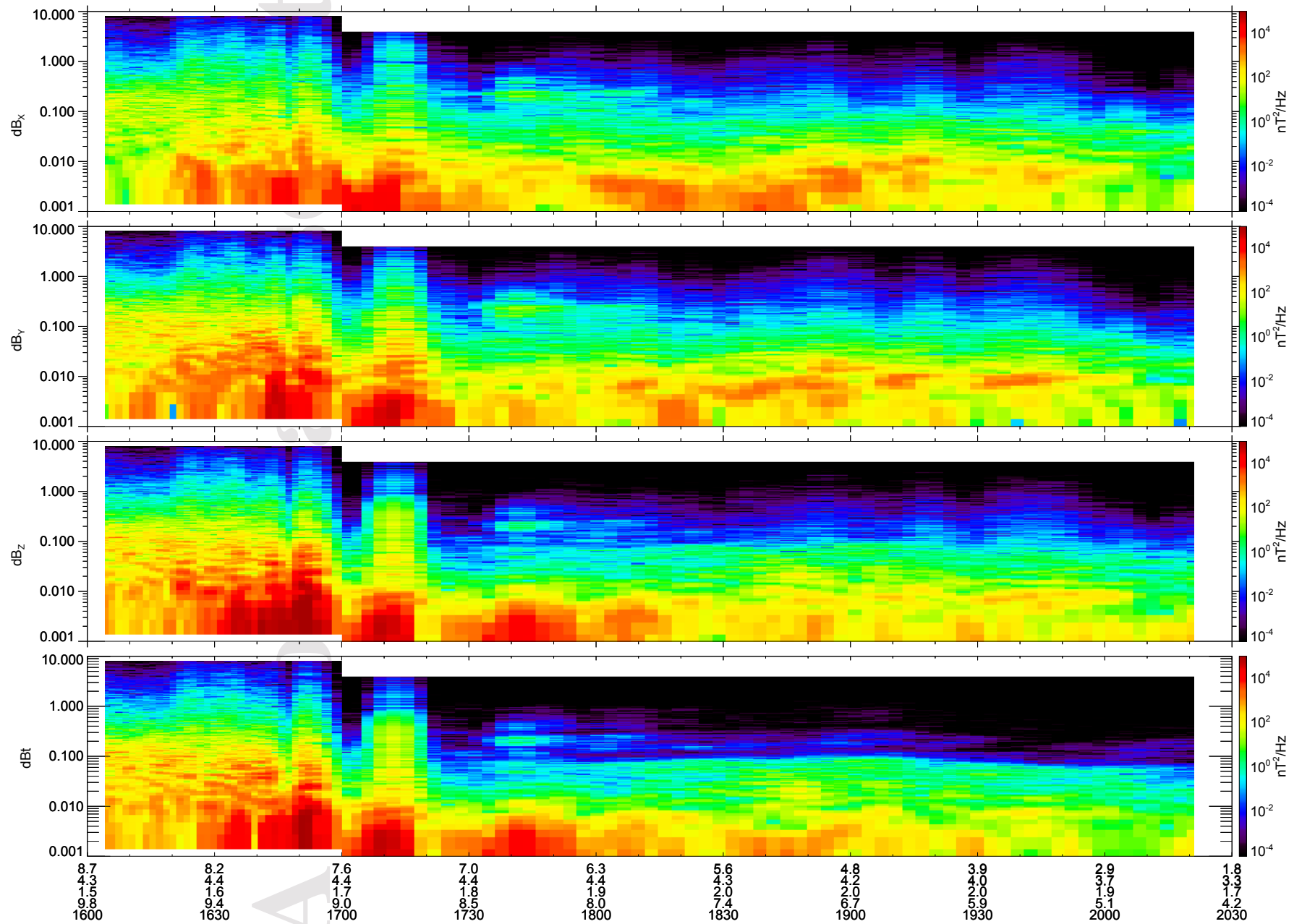




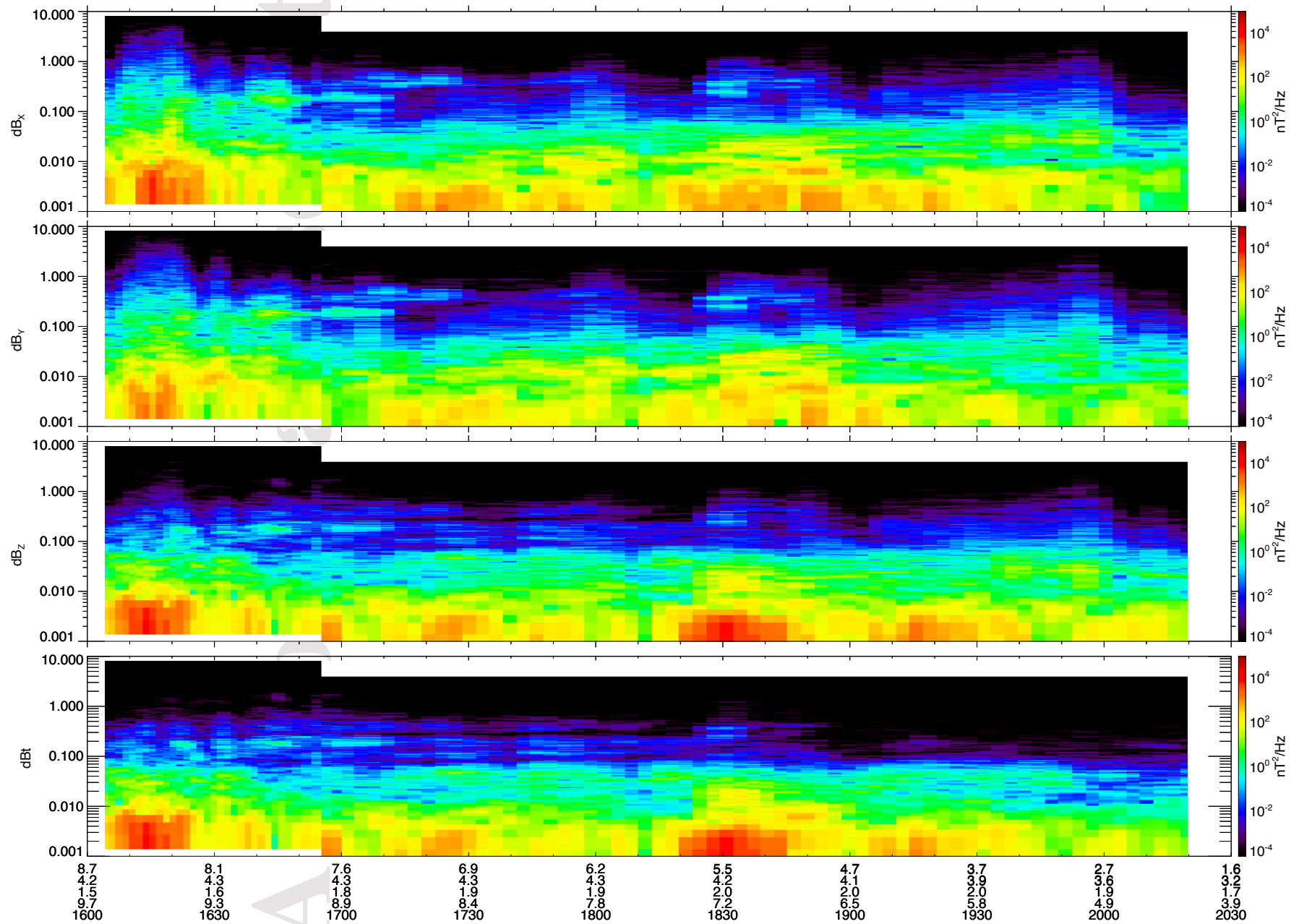
MMS1 Inbound Dynamic Power Spectrum - 2016-12-20



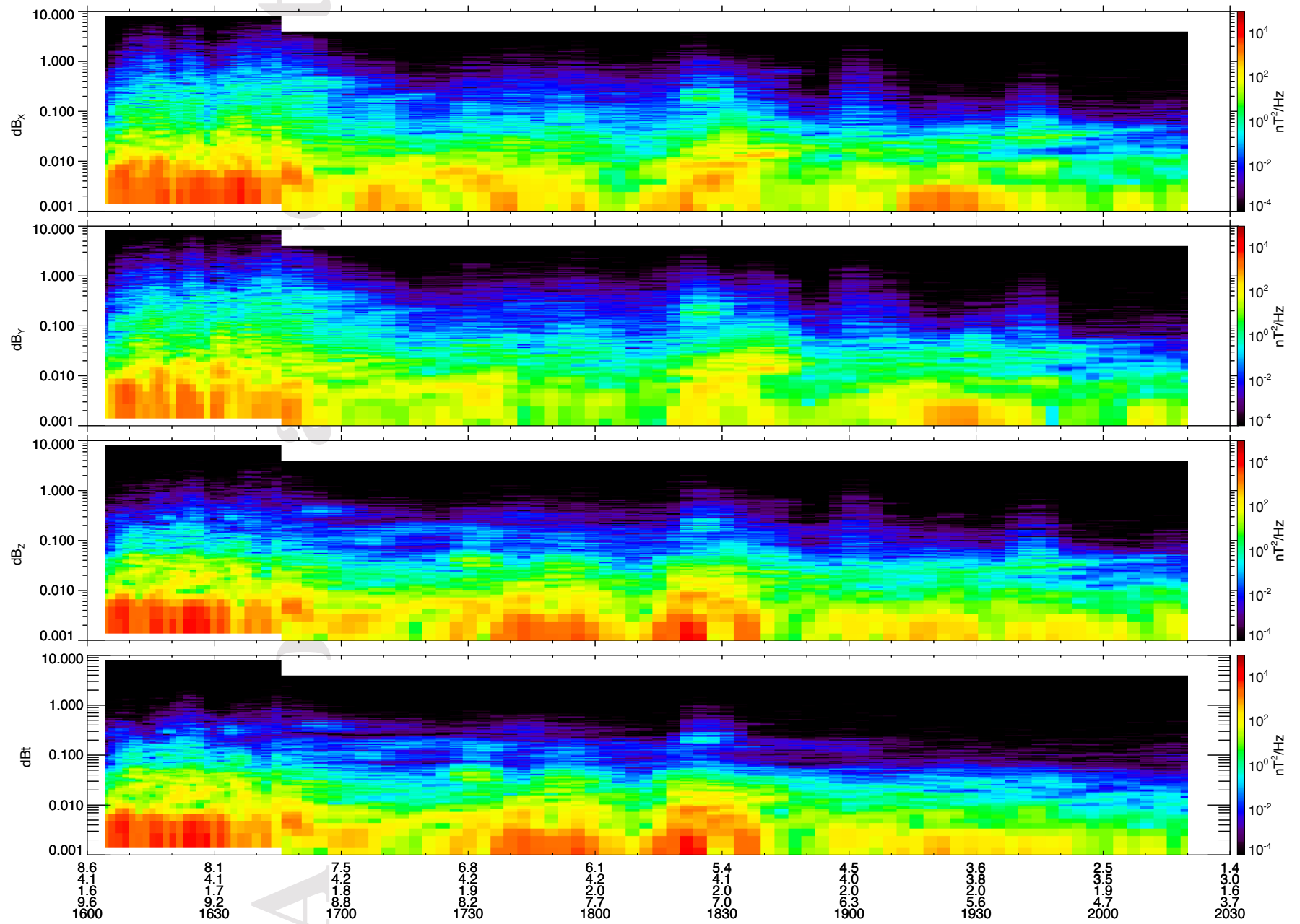
MMS1 Inbound Dynamic Power Spectrum 2016-12-21



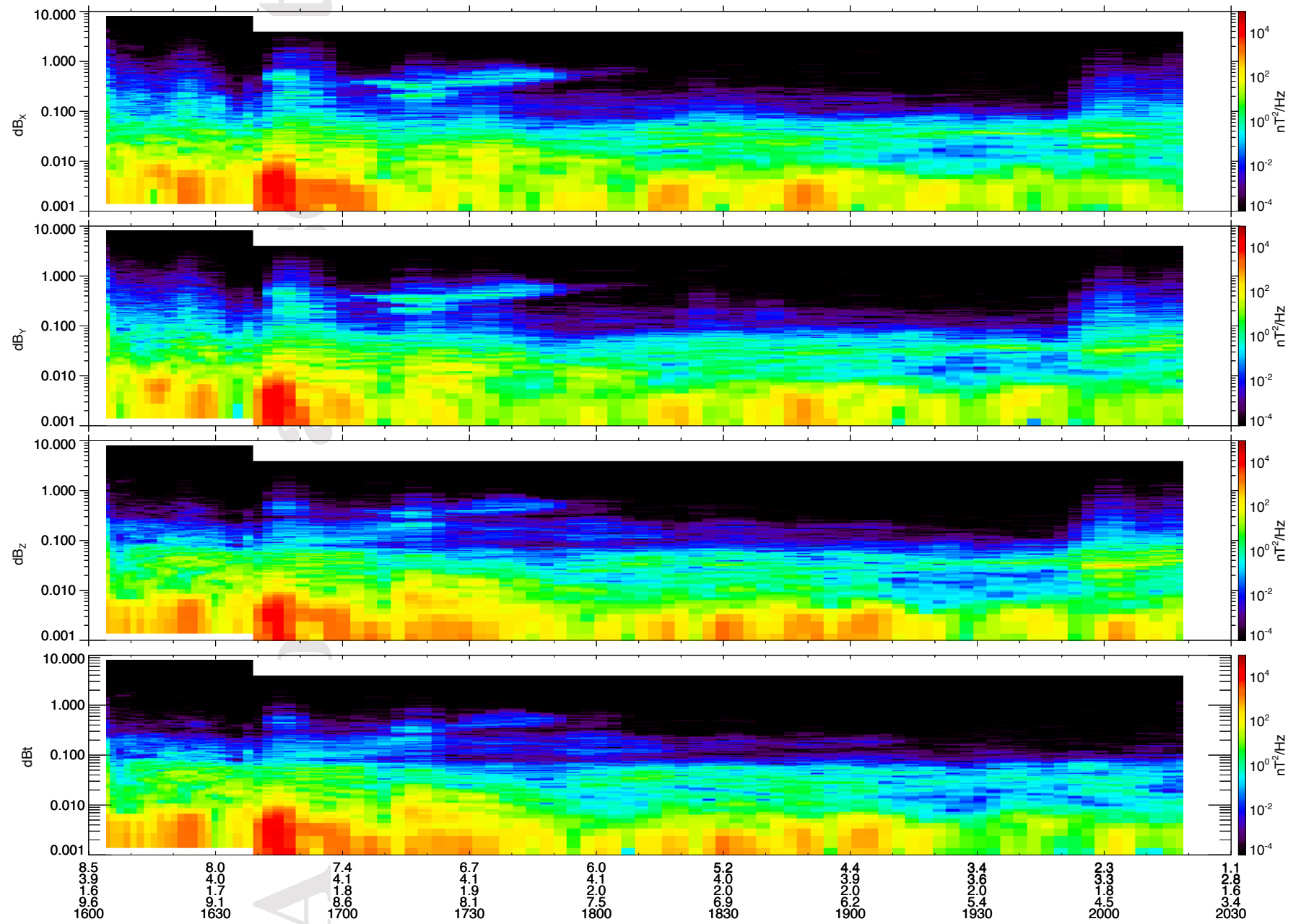
MMS1 Inbound Dynamic Power Spectrum 2016-12-22



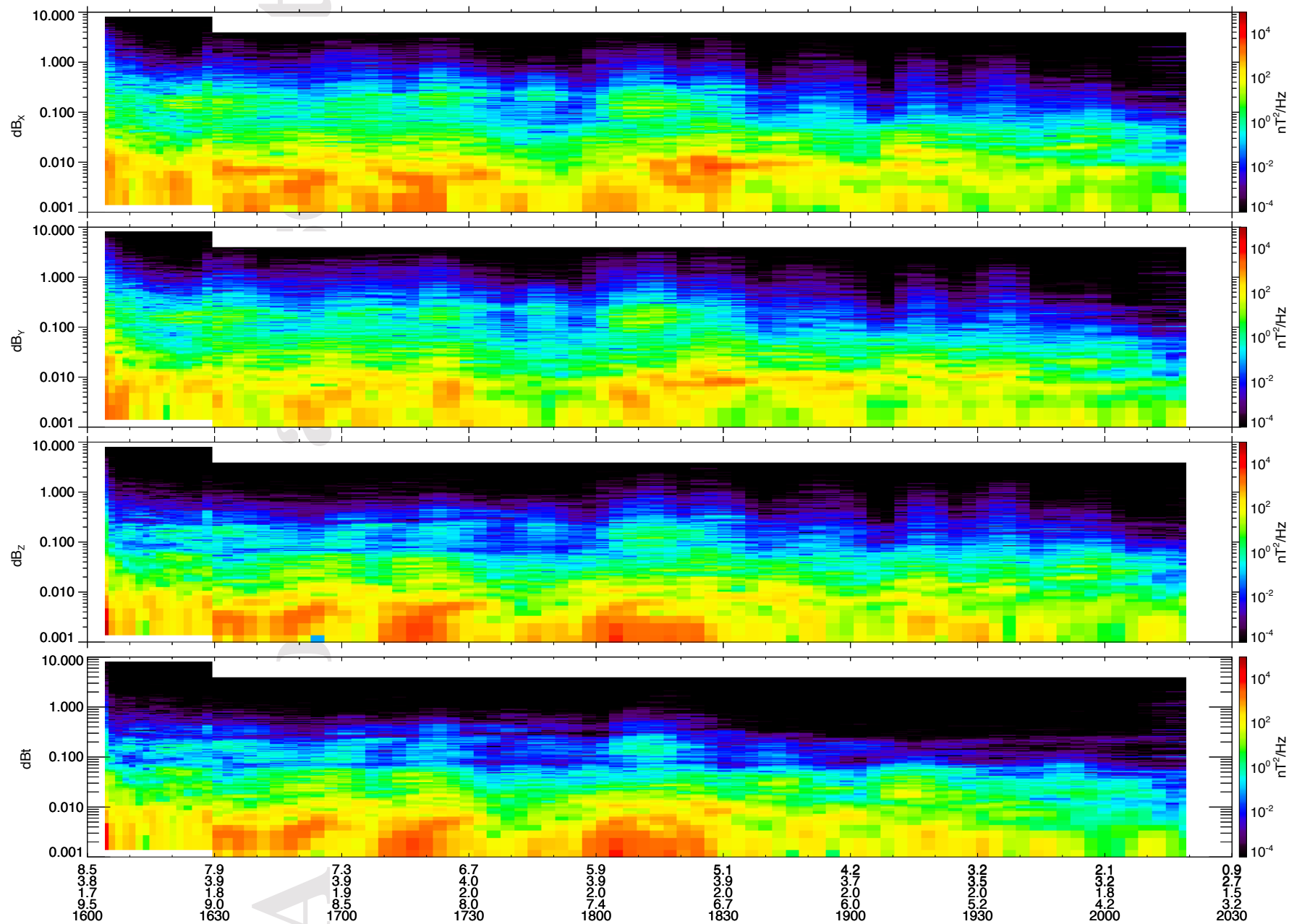
MMS1 Inbound Dynamic Power Spectrum 2016-12-23



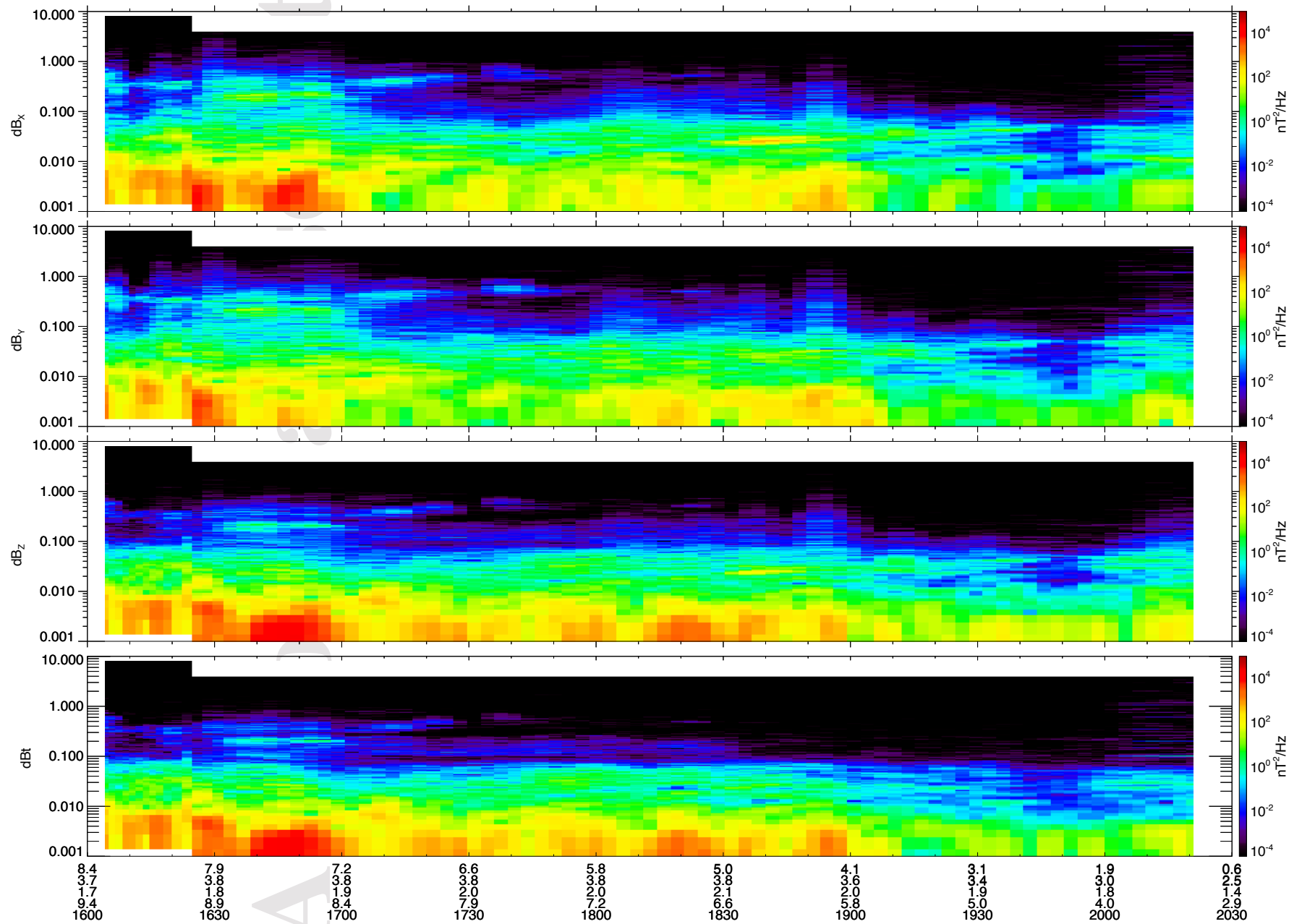
MMS1 Inbound Dynamic Power Spectrum 2016-12-24



MMS1 Inbound Dynamic Power Spectrum 2016-12-25

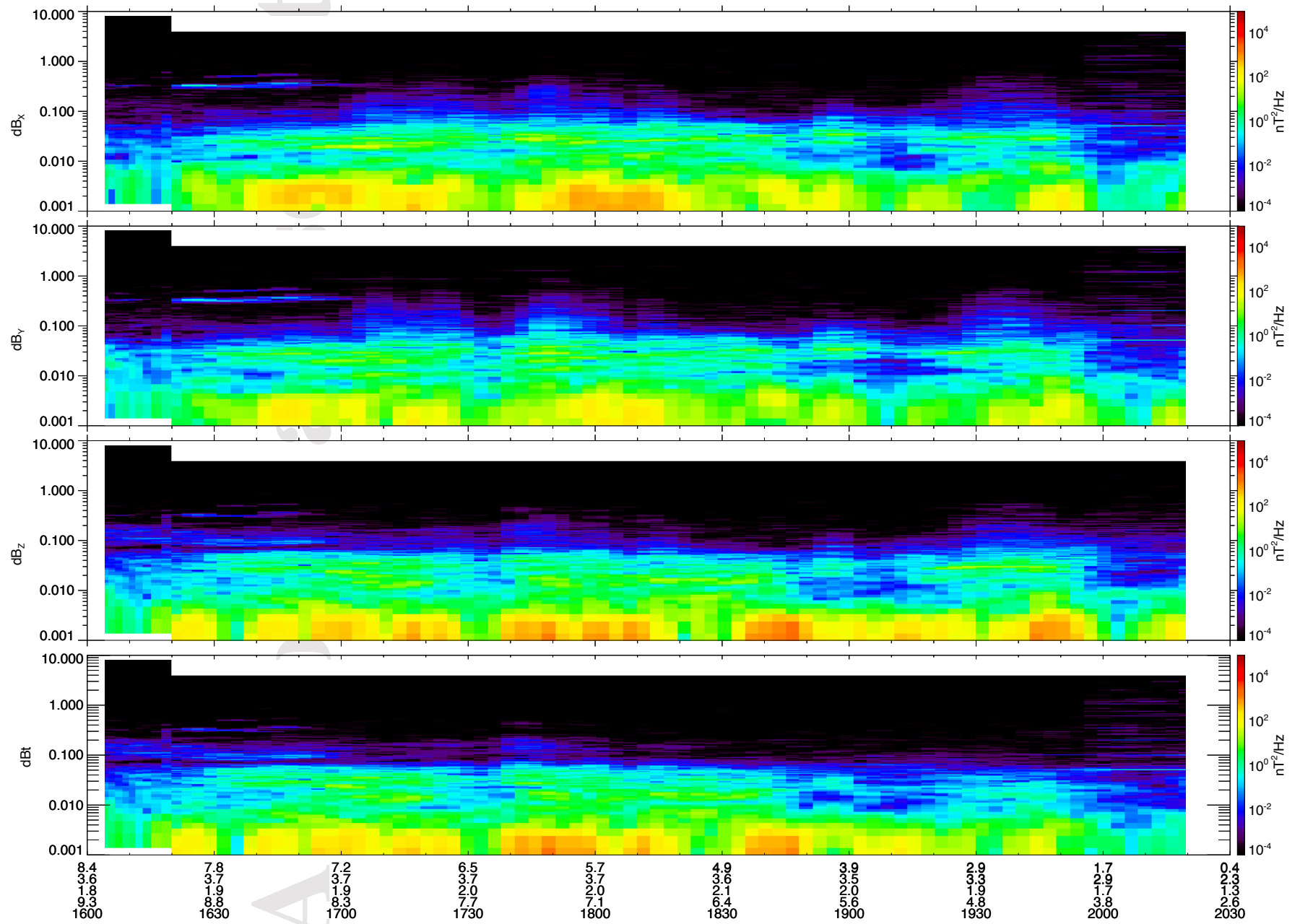


MMS1 Inbound Dynamic Power Spectrum 2016-12-26

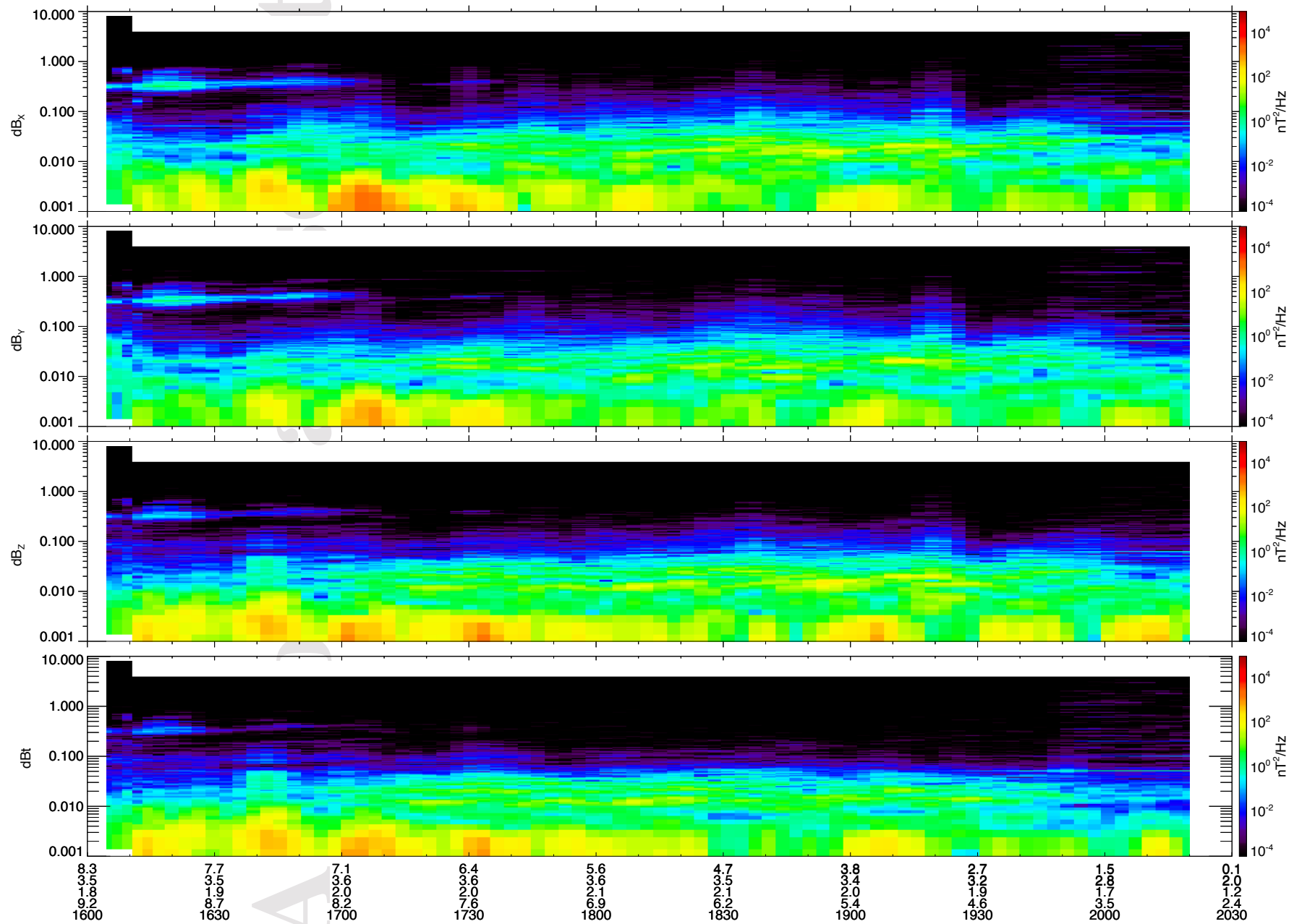




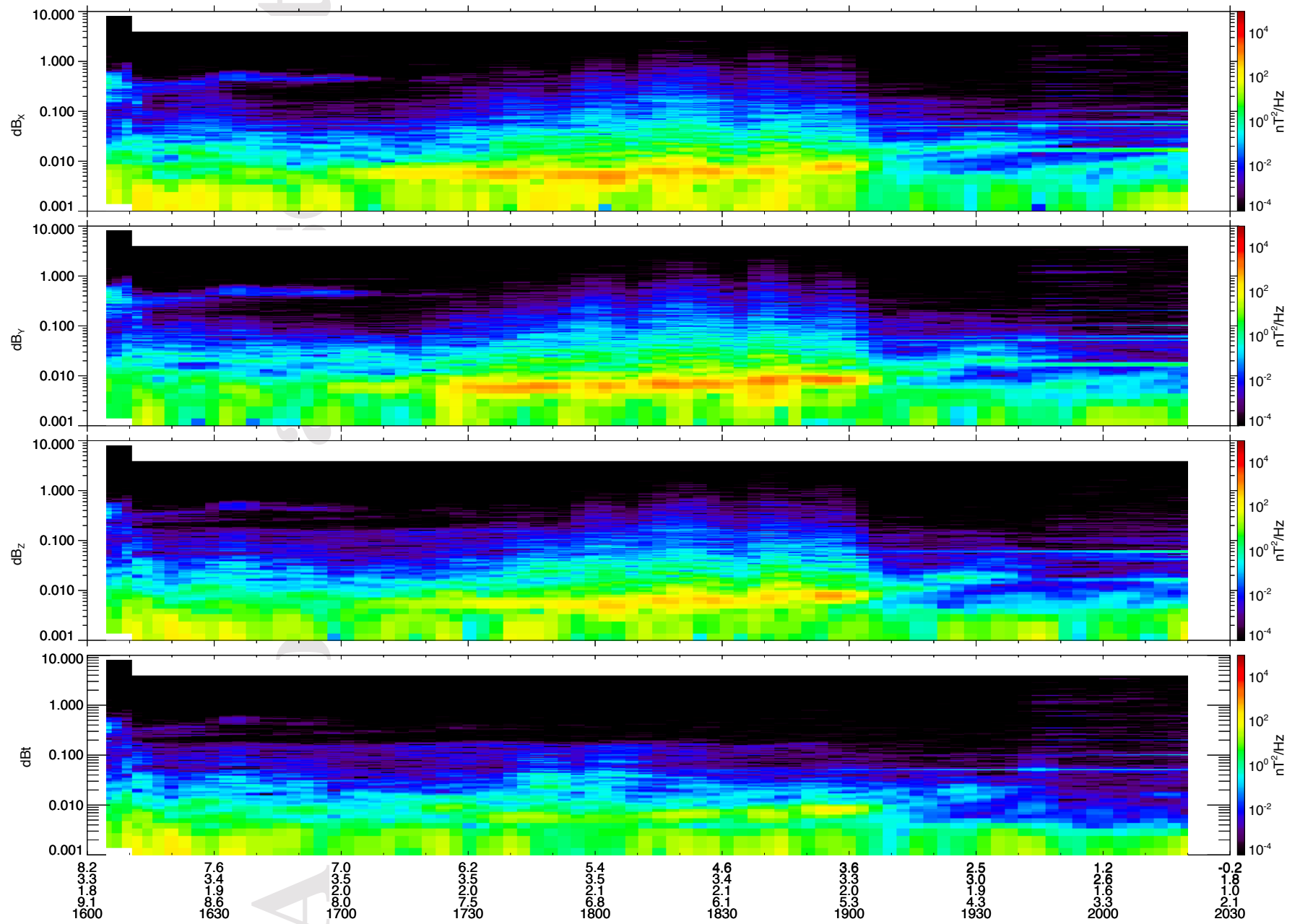
MMS1 Inbound Dynamic Power Spectrum 2016-12-27



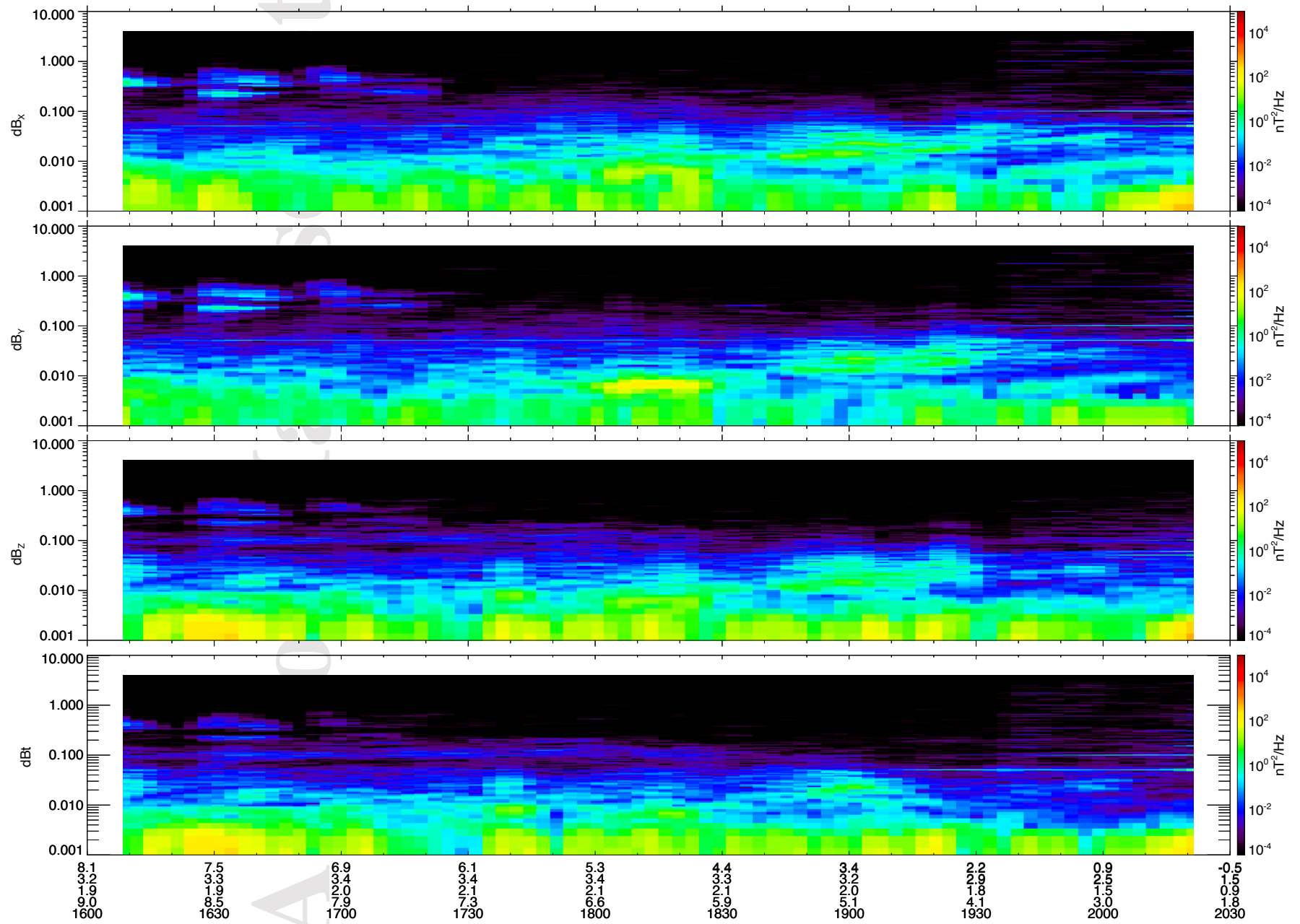
MMS1 Inbound Dynamic Power Spectrum 2016-12-28



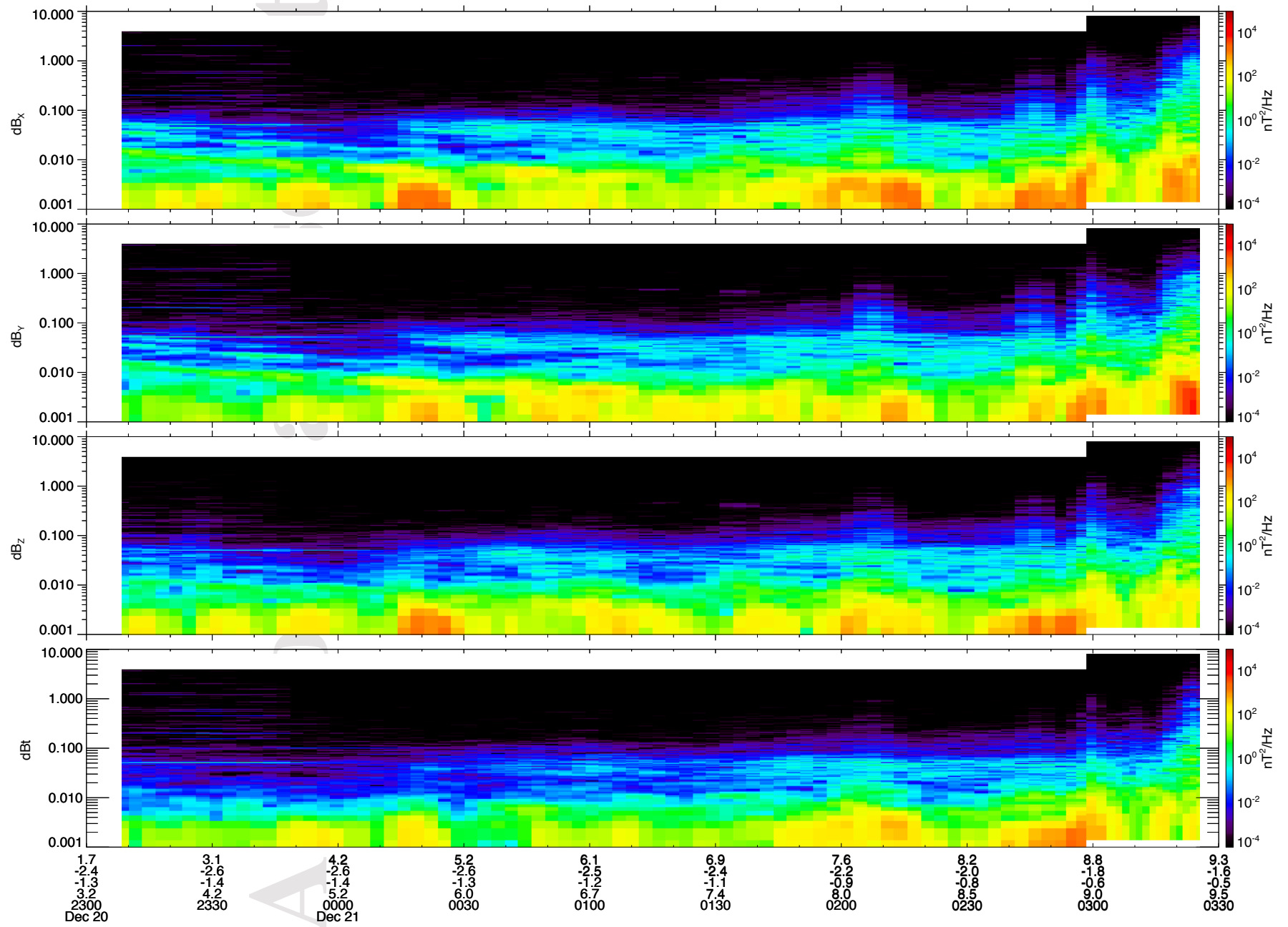
MMS1 Inbound Dynamic Power Spectrum 2016-12-29



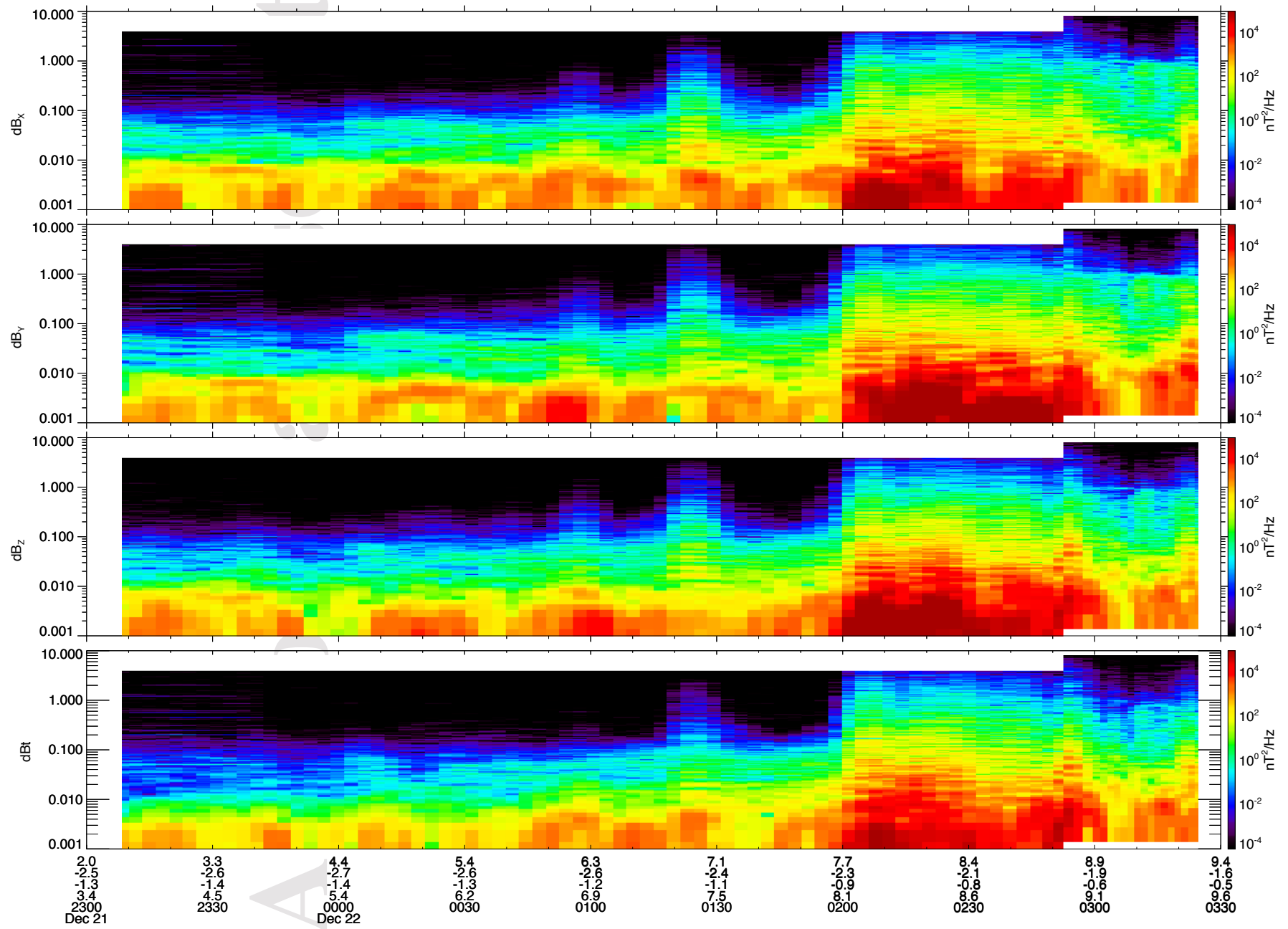
MMS1 Inbound Dynamic Power Spectrum 2016-12-30



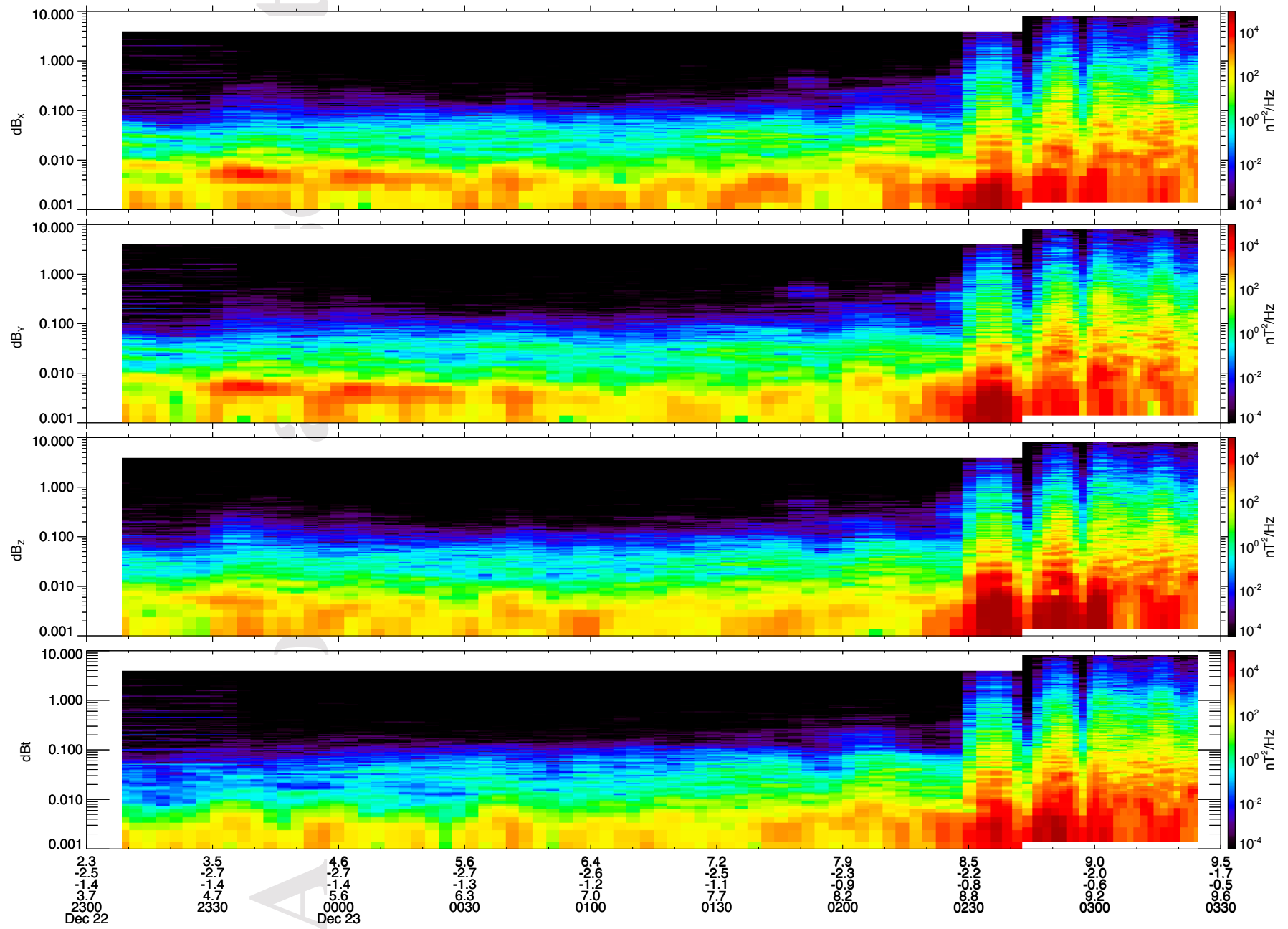
MMS1 Outbound Dynamic Power Spectrum 2016-12-20



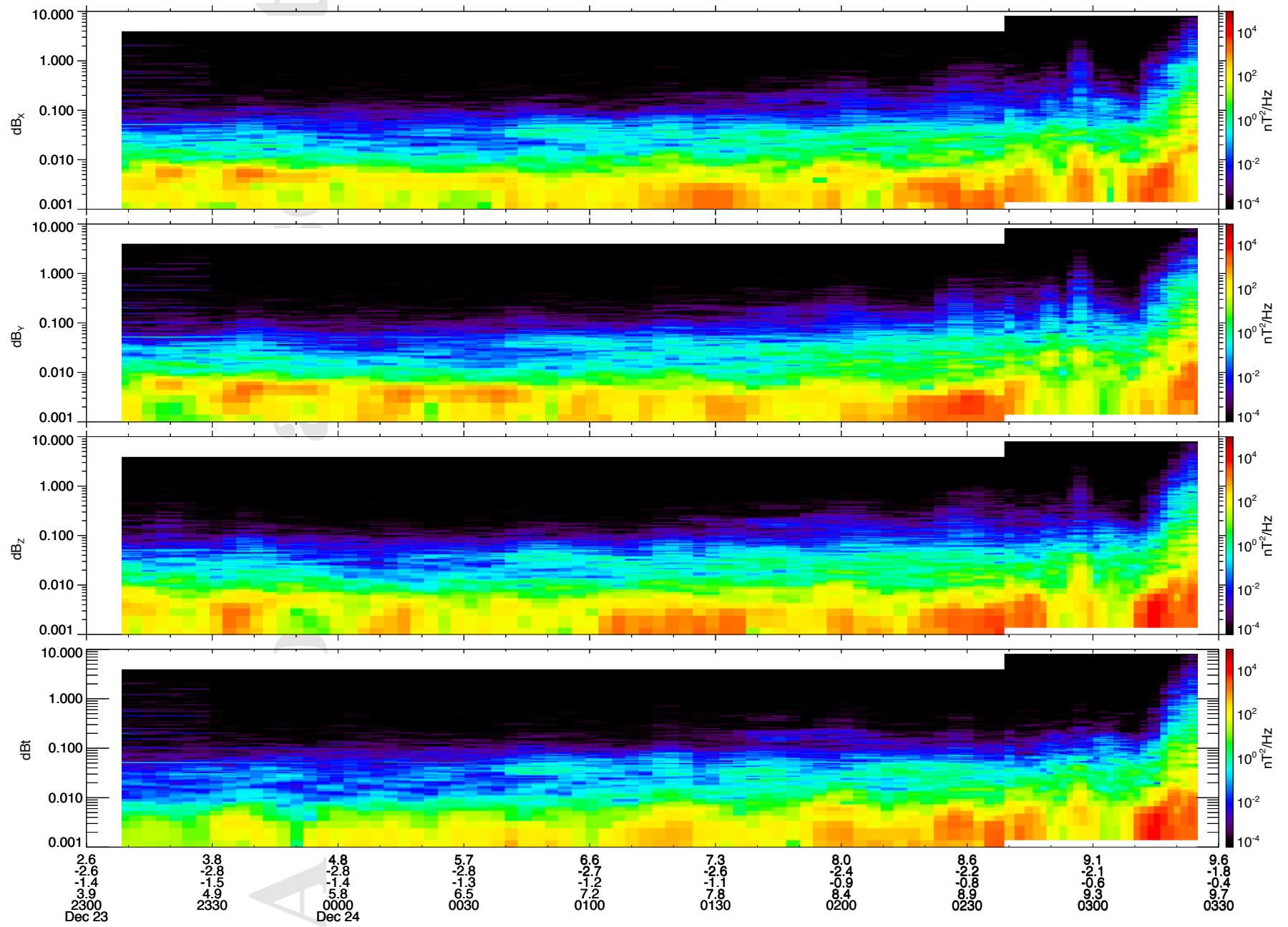
MMS1 Outbound Dynamic Power Spectrum 2016-12-21



MMS1 Outbound Dynamic Power Spectrum 2016-12-22

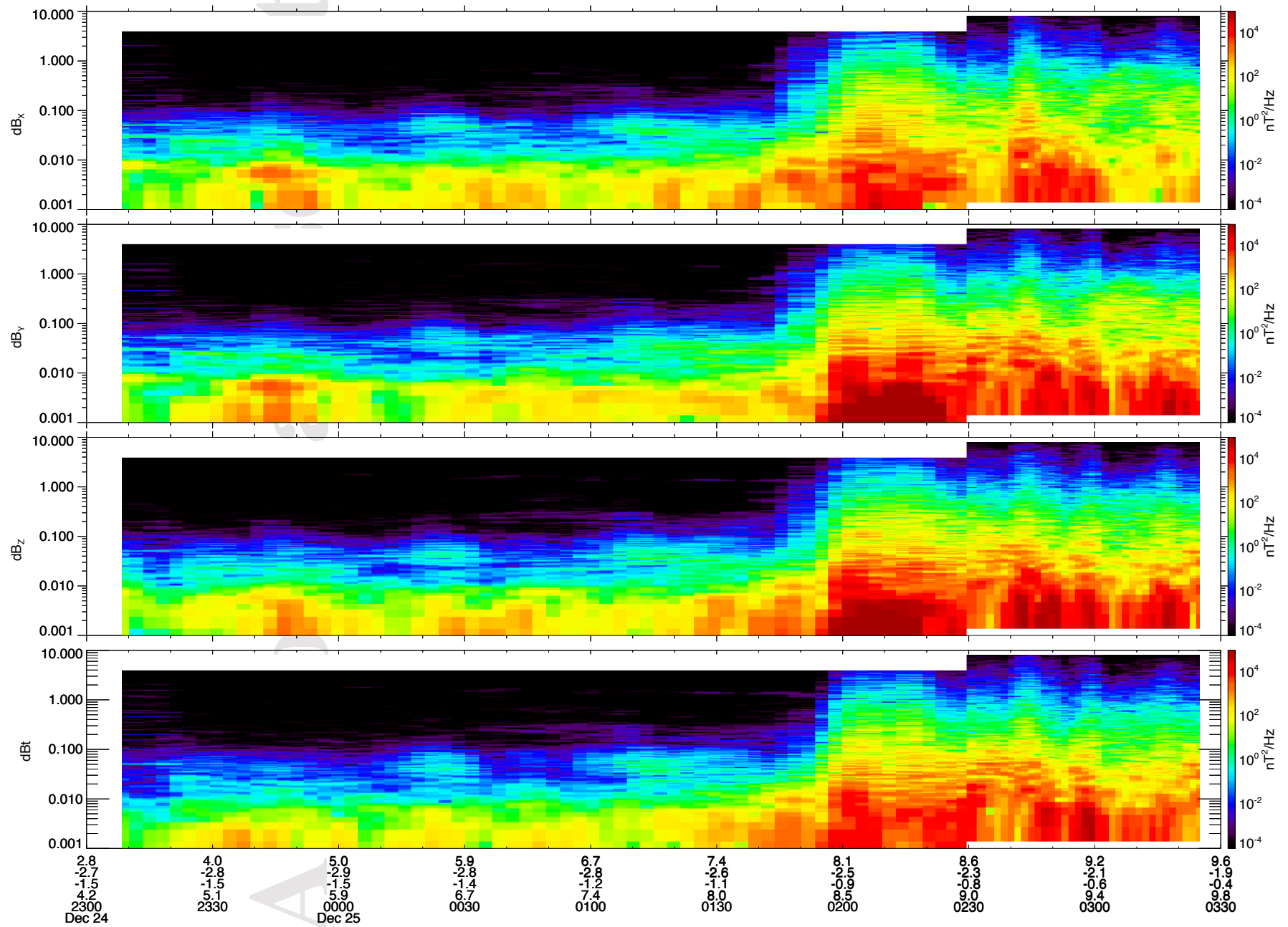


MMS1 Outbound Dynamic Power Spectrum 2016-12-23

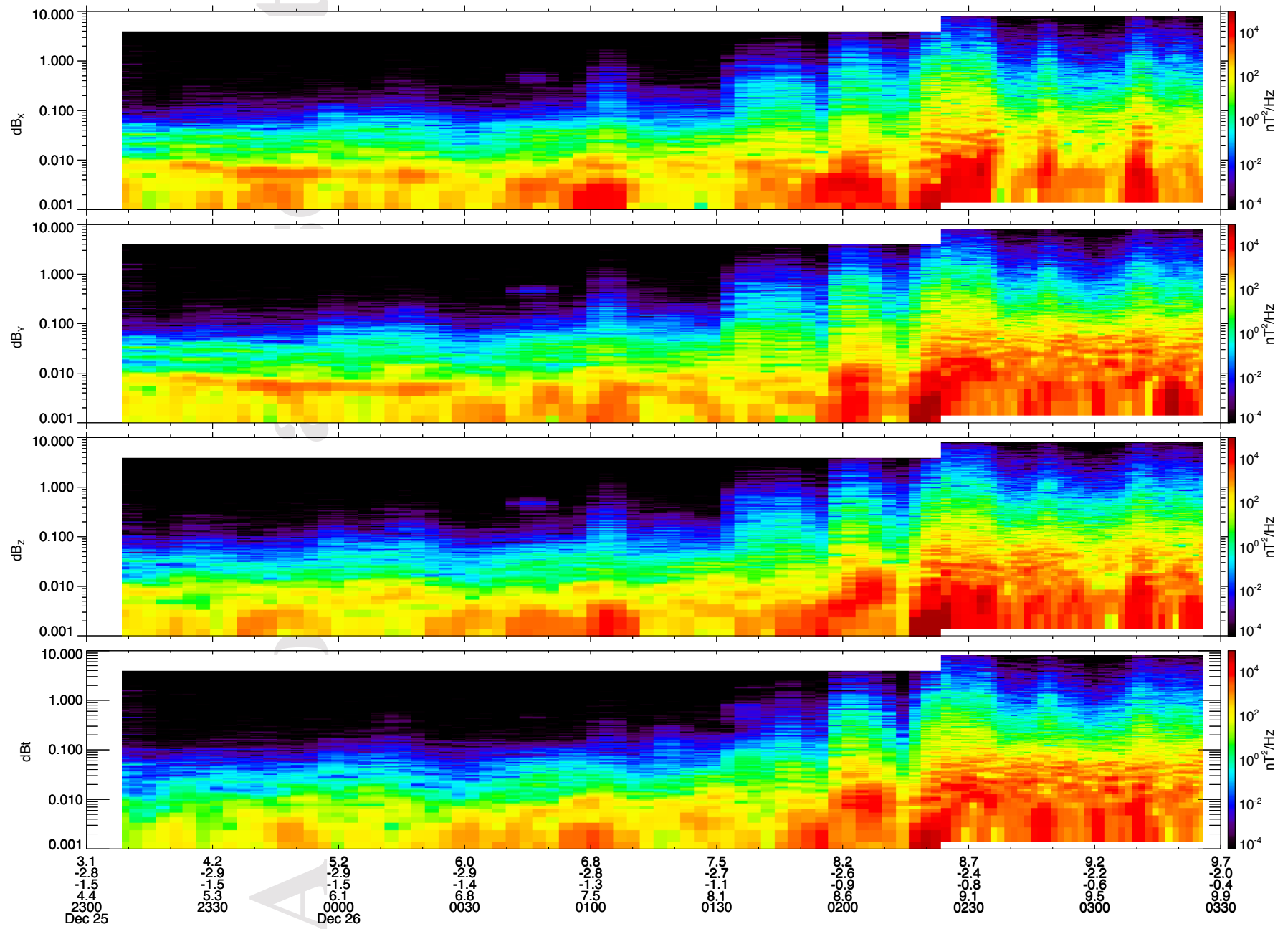




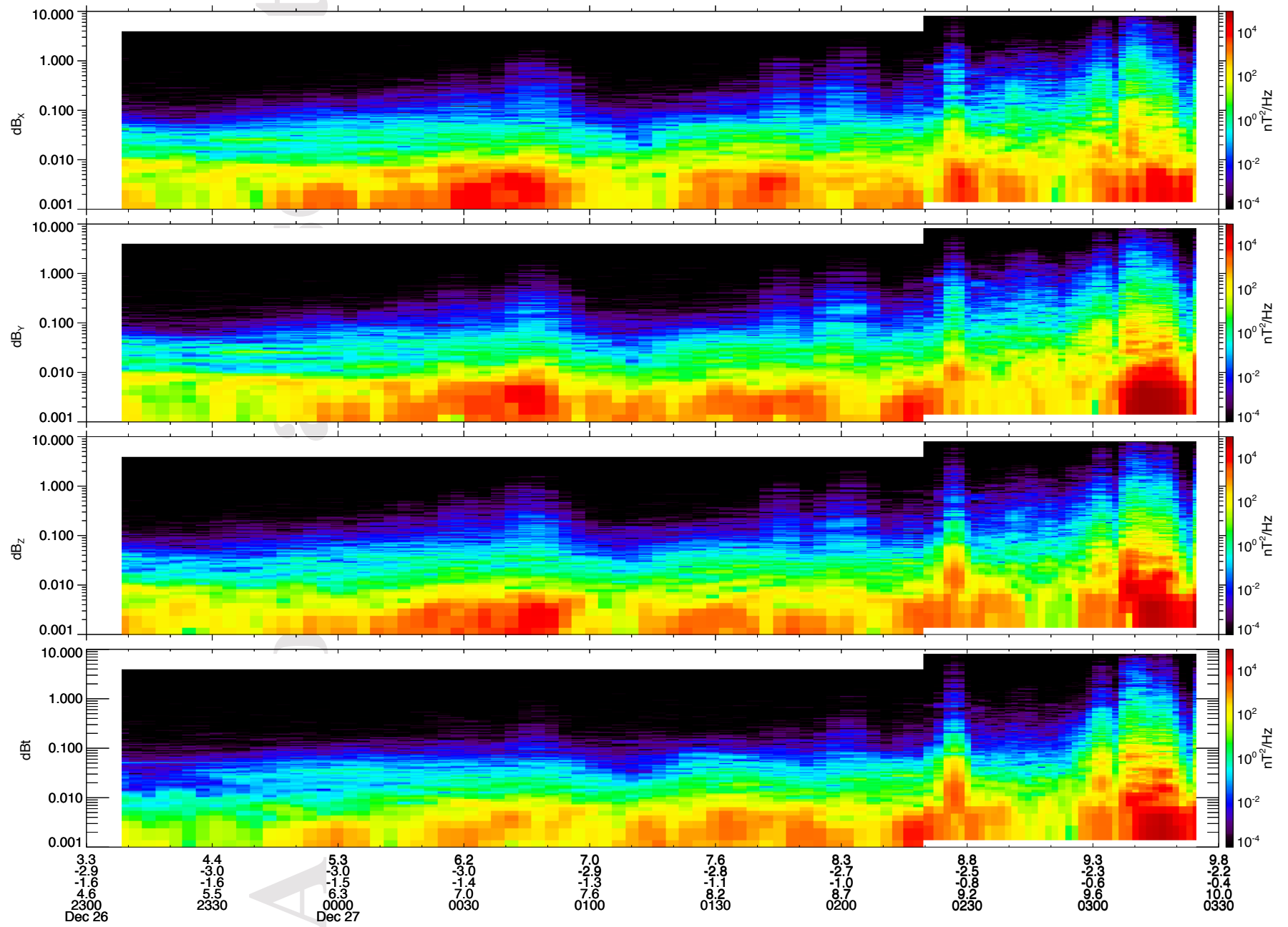
MMS1 Outbound Dynamic Power Spectrum 2016-12-24



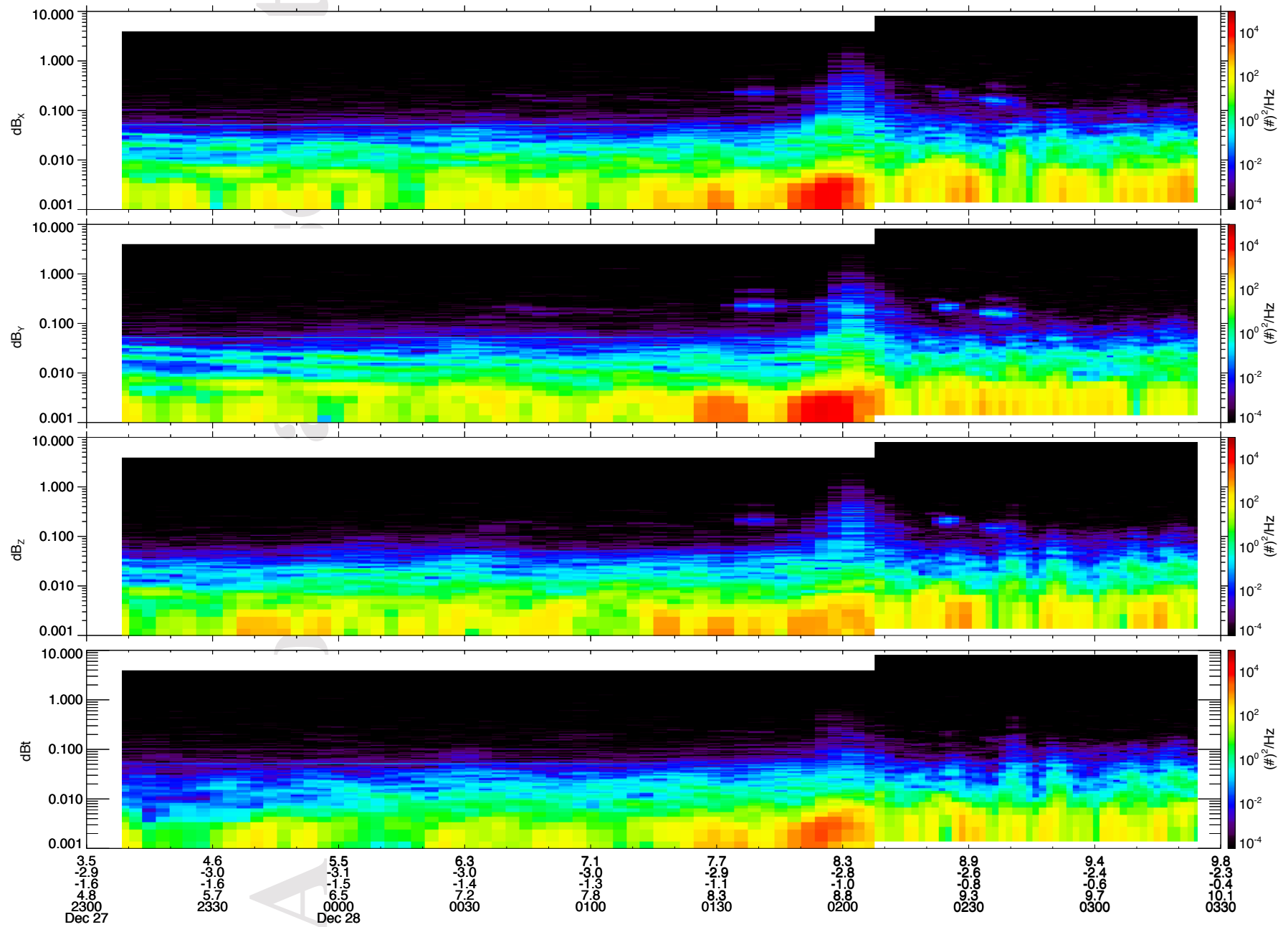
MMS1 Outbound Dynamic Power Spectrum 2016-12-25



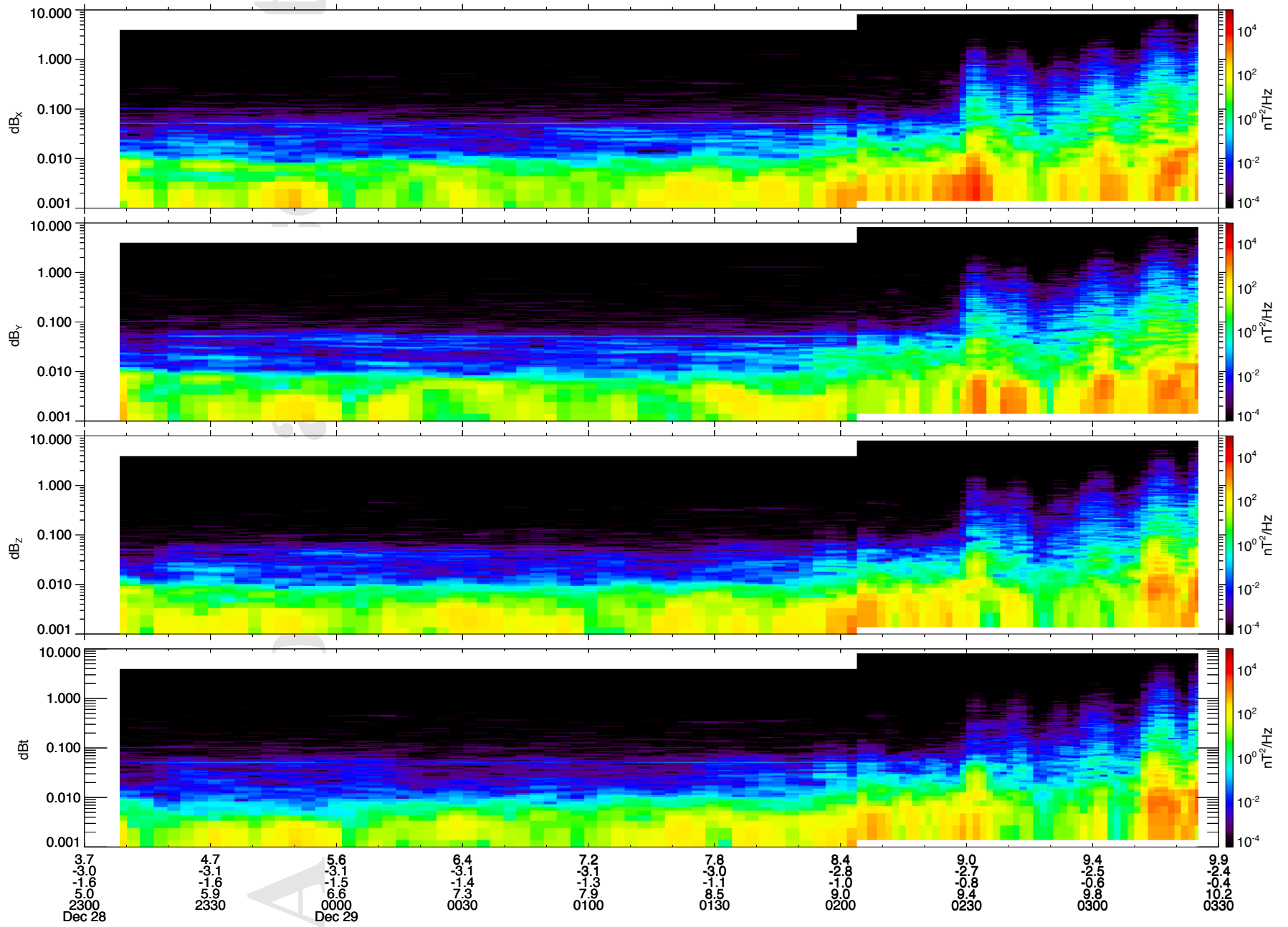
MMS1 Outbound Dynamic Power Spectrum 2016-12-26



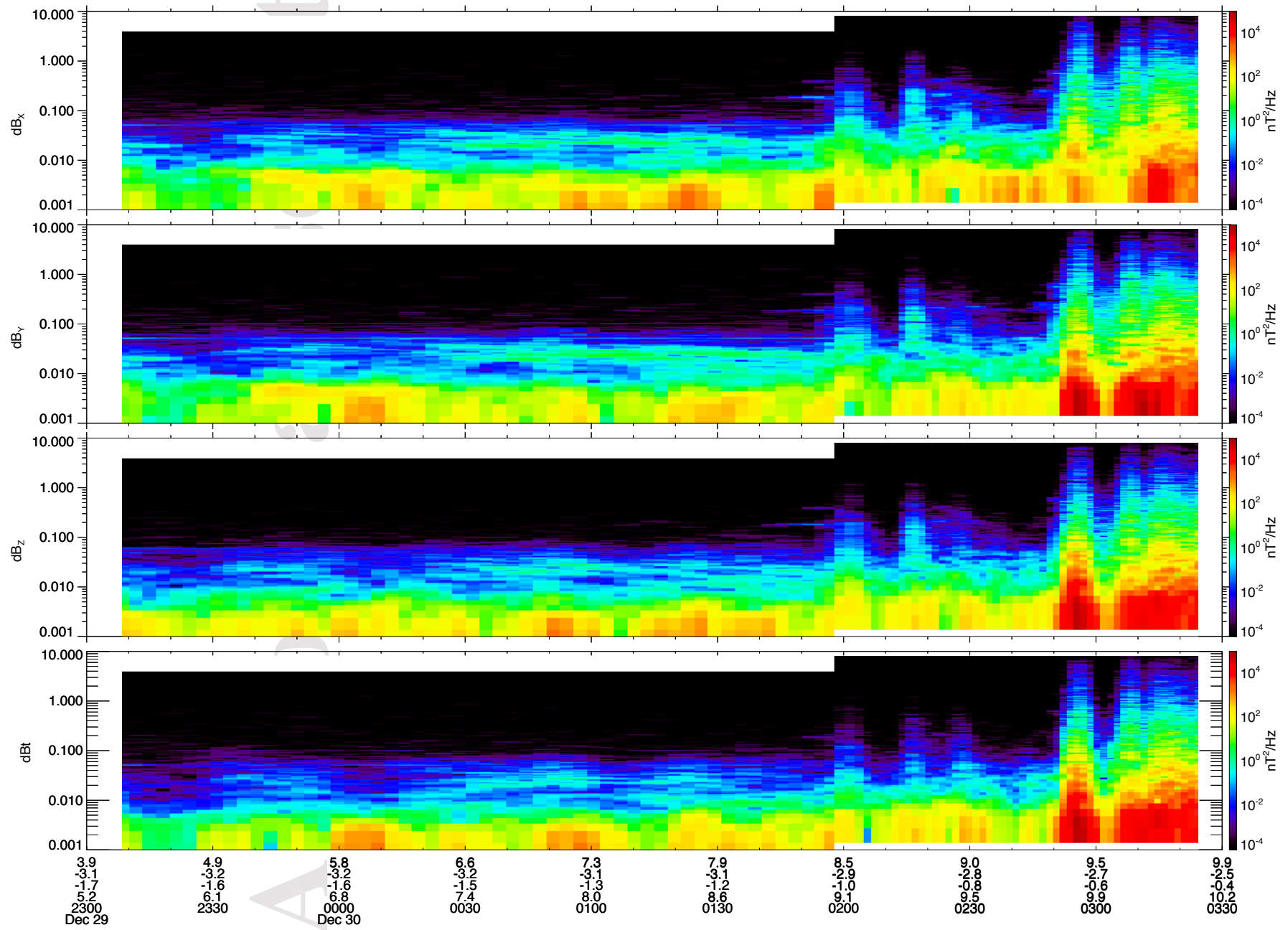
MMS1 Outbound Dynamic Power Spectrum 2016-12-27



MMS1 Outbound Dynamic Power Spectrum 2016-12-28



MMS1 Outbound Dynamic Power Spectrum 2016-12-29



**MMS Observations of Field Line Resonances Under Disturbed Solar Wind Conditions**

Le<sup>1</sup>, P. J. Chi<sup>2</sup>, R. J. Strangeway<sup>2</sup>, C. T. Russell<sup>2</sup>, J. A. Slavin<sup>3</sup>, B. Anderson<sup>4</sup>, R. Nakamura<sup>5</sup>, F. Plaschke<sup>5</sup>, R. Torbert<sup>6</sup>, and F. Wilder<sup>7</sup>

<sup>1</sup> Heliophysics Science Division, NASA Goddard Space Flight Center, Greenbelt, Maryland

<sup>2</sup> Department of Earth and Space Sciences, University of California, Los Angeles, California

<sup>3</sup> Department of Climate and Space Sciences and Engineering, University of Michigan, Ann Arbor, Michigan

<sup>4</sup> Johns Hopkins University Applied Physics Laboratory, Laurel, Maryland

<sup>5</sup> Space Research Institute, Austrian Academy of Sciences, Graz, Austria

<sup>6</sup> University of New Hampshire, Durham, New Hampshire

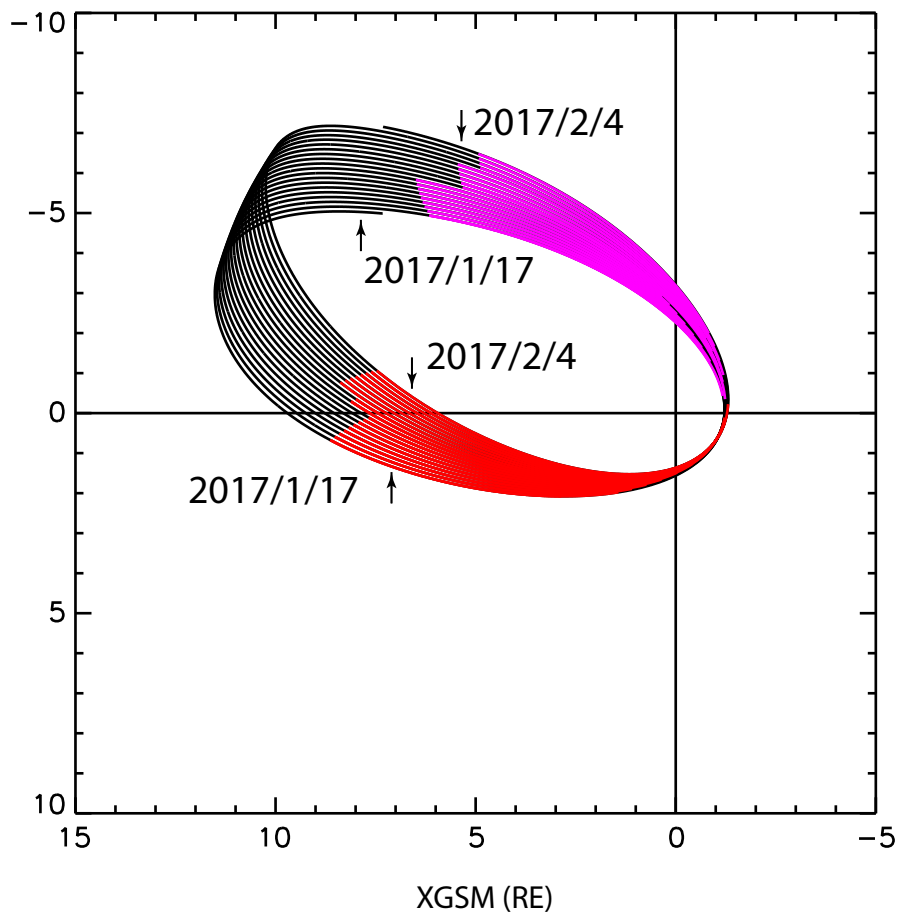
<sup>7</sup> Laboratory for Atmospheric and Space Physics, University of Colorado, Boulder, Colorado

**Contents of this file**

Figure S2

**Introduction**

**Figure S2** provides supporting information to Figures 6. The first page shows the MMS-1 spacecraft orbits in the GSM XY plane for the time period from 0000 UT 17 January 2017 to 2400 UT 4 February 2017. The spacecraft orbit period was approximately 1 day in this mission phase. The rest of the pages show the dynamic power spectra of the magnetic field components ( $b_x$ ,  $b_y$ ,  $b_z$ ) and the field strength ( $b_t$ ) for inbound and outbound passes. The colored orbit segments in the orbit plot correspond to the inbound (red) and outbound (magenta) time intervals displayed in these pages. The horizontal labels are the spacecraft position (XGSM, YGSM, ZGSM) in RE, the radial distance in RE, Universal Time (UT), respectively.

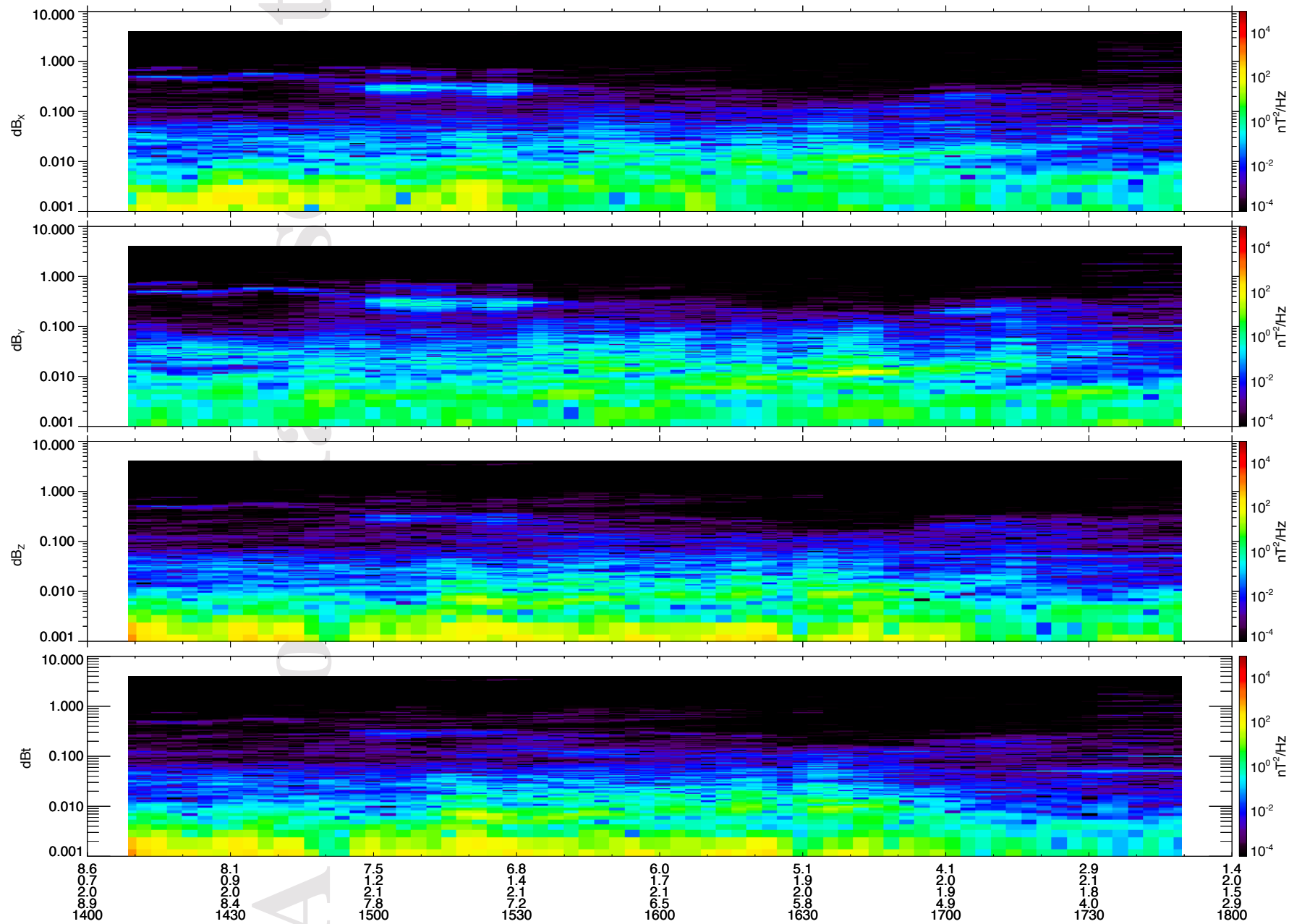


— Outbound  
1900-2300 UT 1/17-1/25  
1800-2200 UT 1/26-1/31  
1730-2130 UT 2/1-2/4

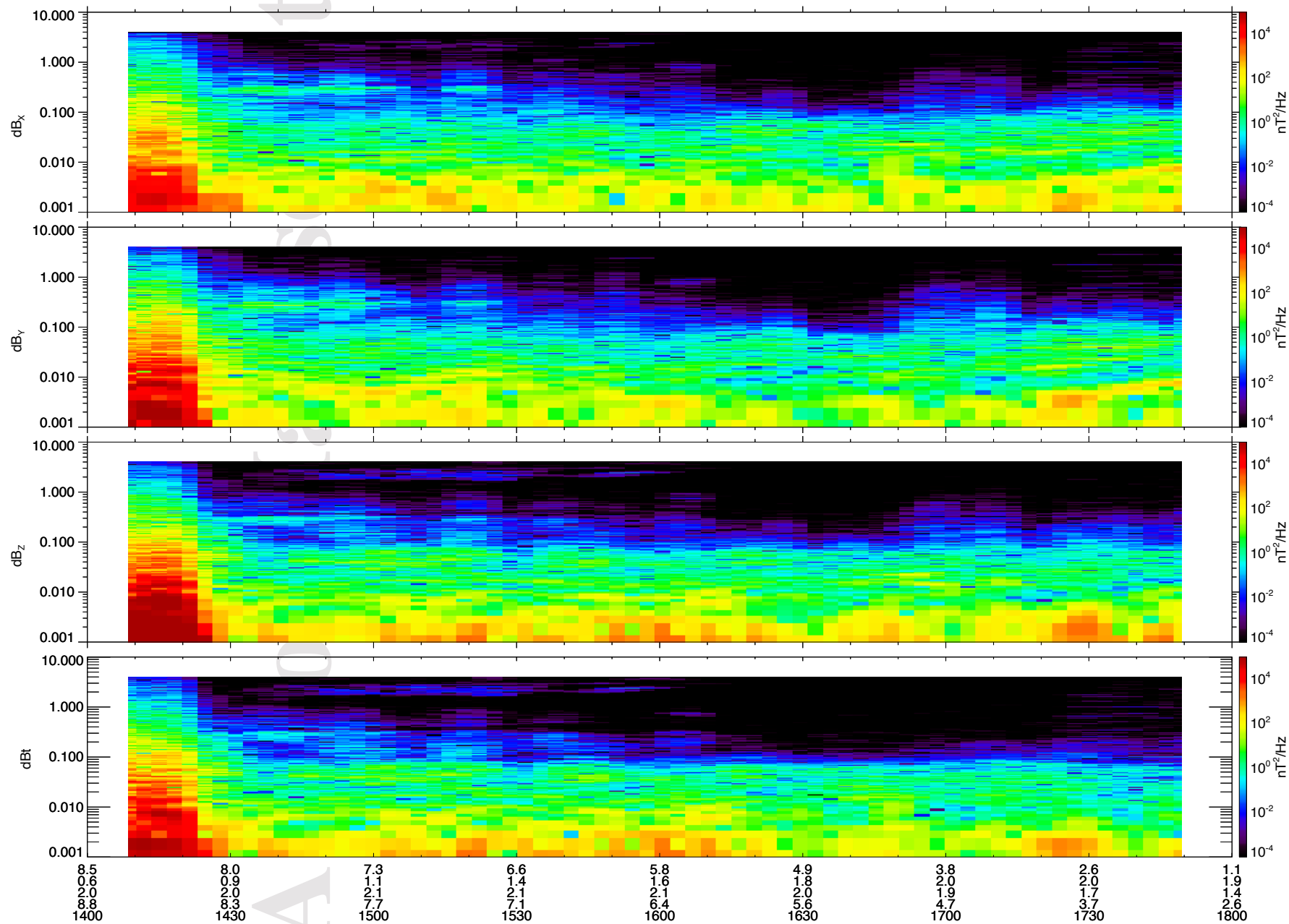
— Inbound  
1400-1800 UT 1/17-1/25  
1330-1730 UT 1/26 & 1/27  
1300-17:00 UT 1/28-2/4



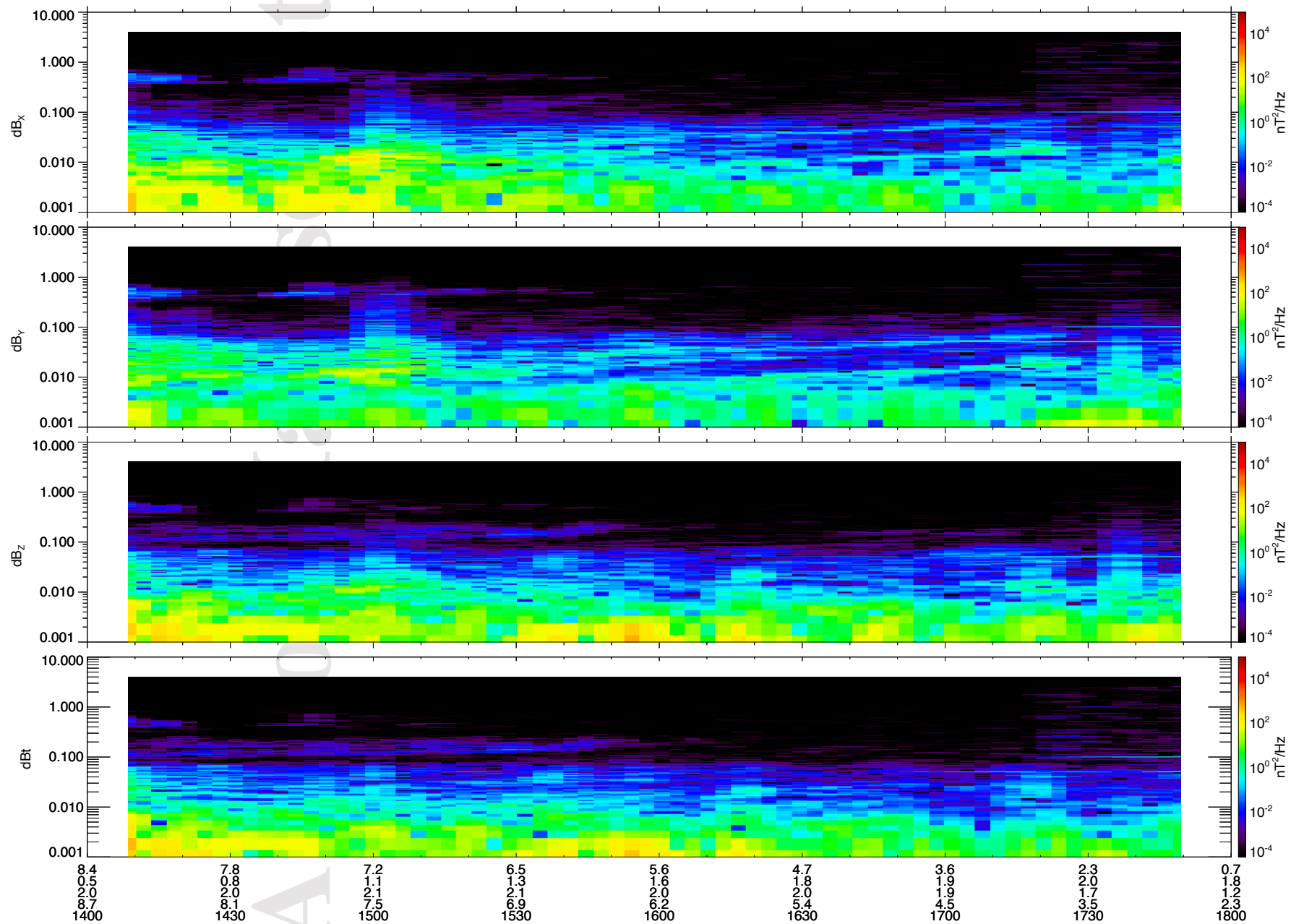
MMS1 Inbound Dynamic Power Spectrum - 2017-01-17



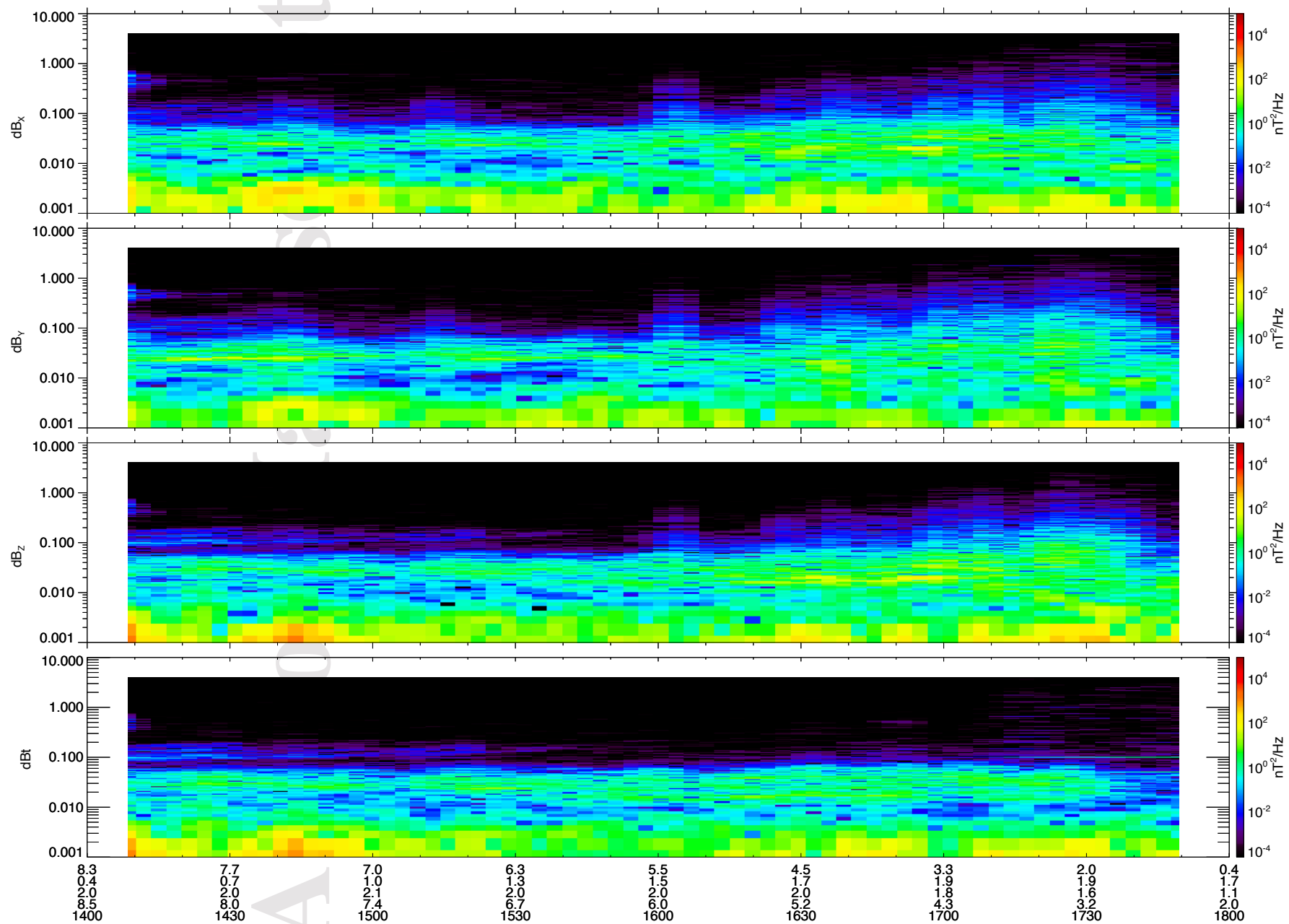
MMS1 Inbound Dynamic Power Spectrum - 2017-01-18



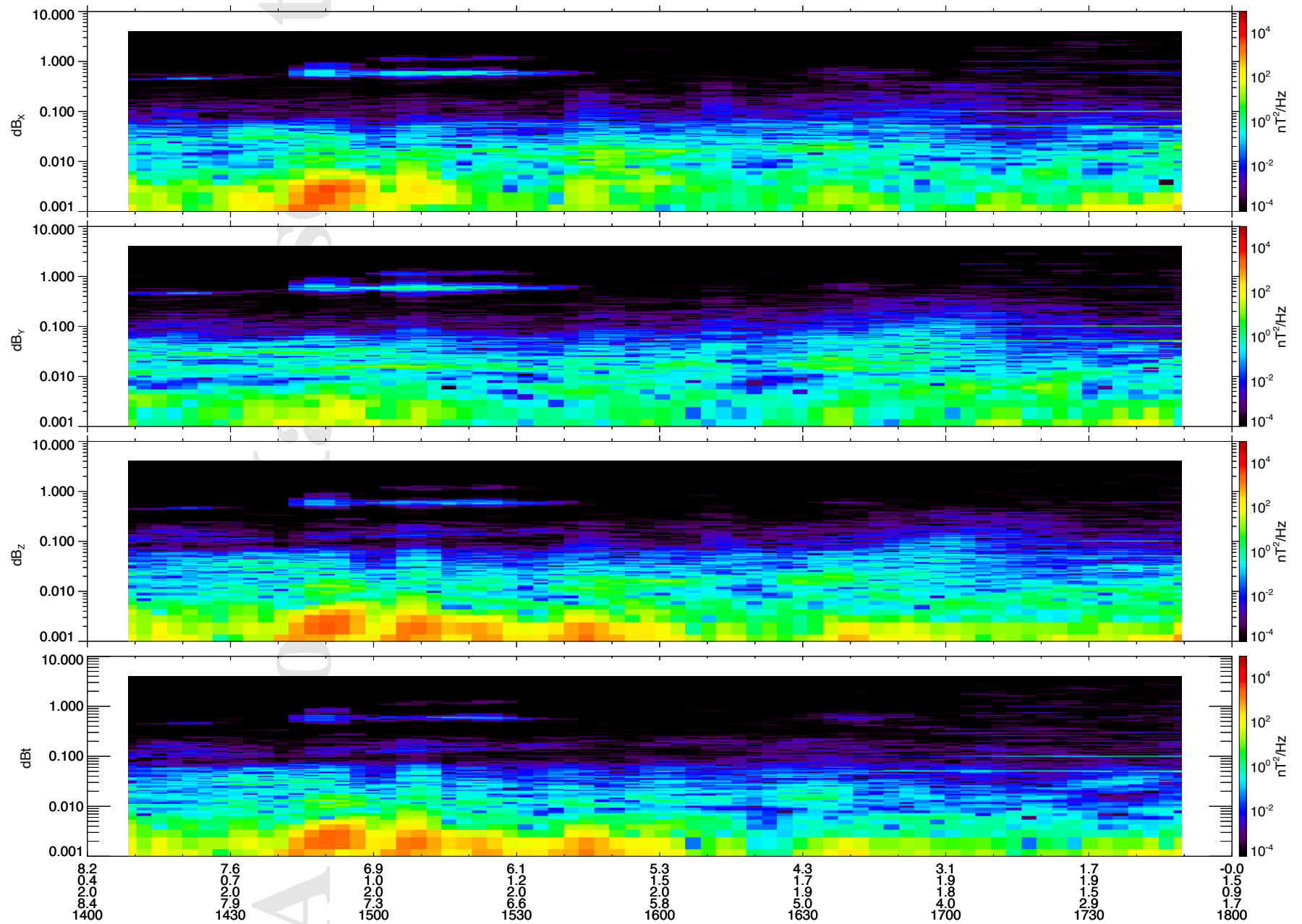
MMS1 Inbound Dynamic Power Spectrum - 2017-01-19



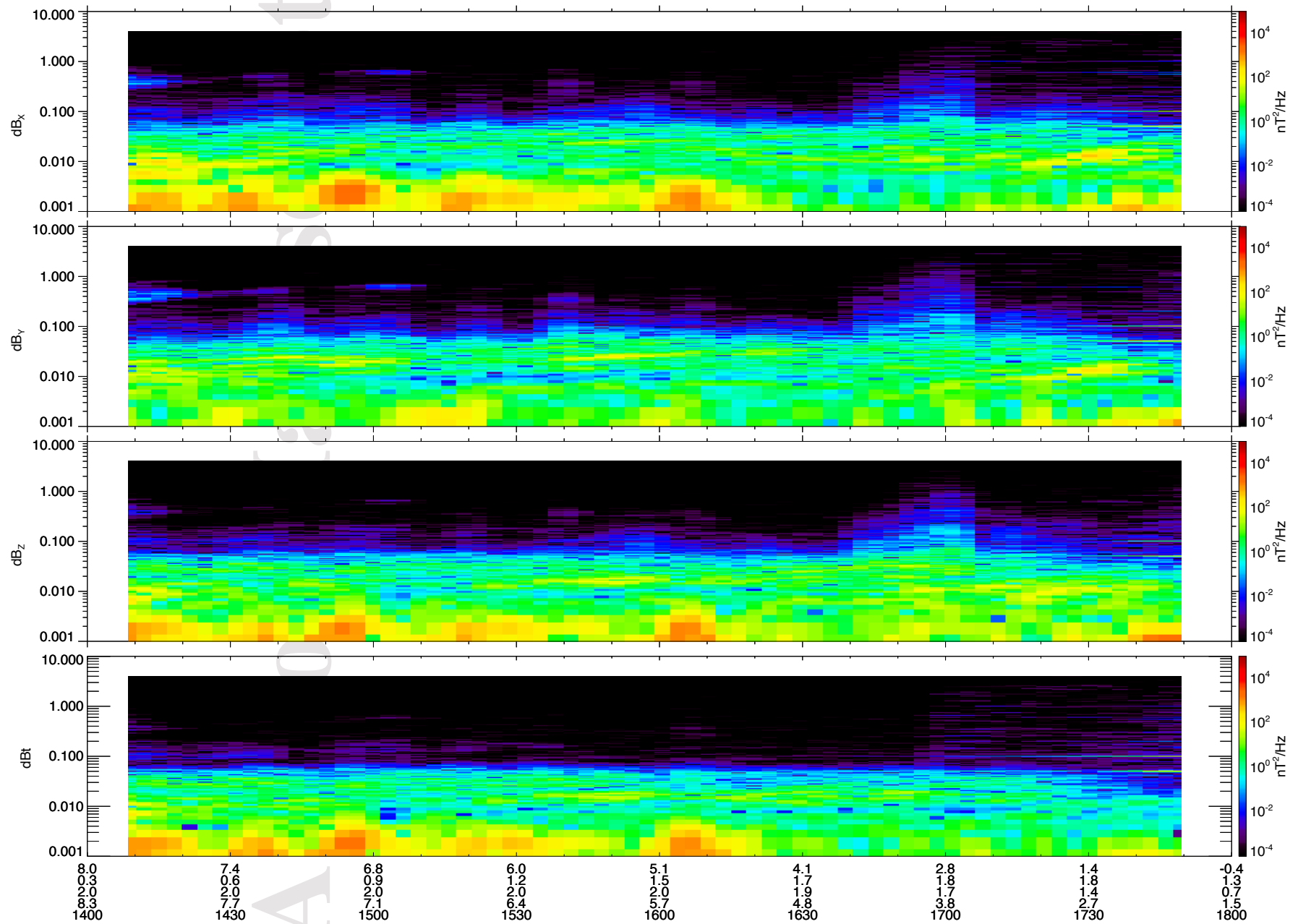
MMS1 Inbound Dynamic Power Spectrum - 2017-01-20



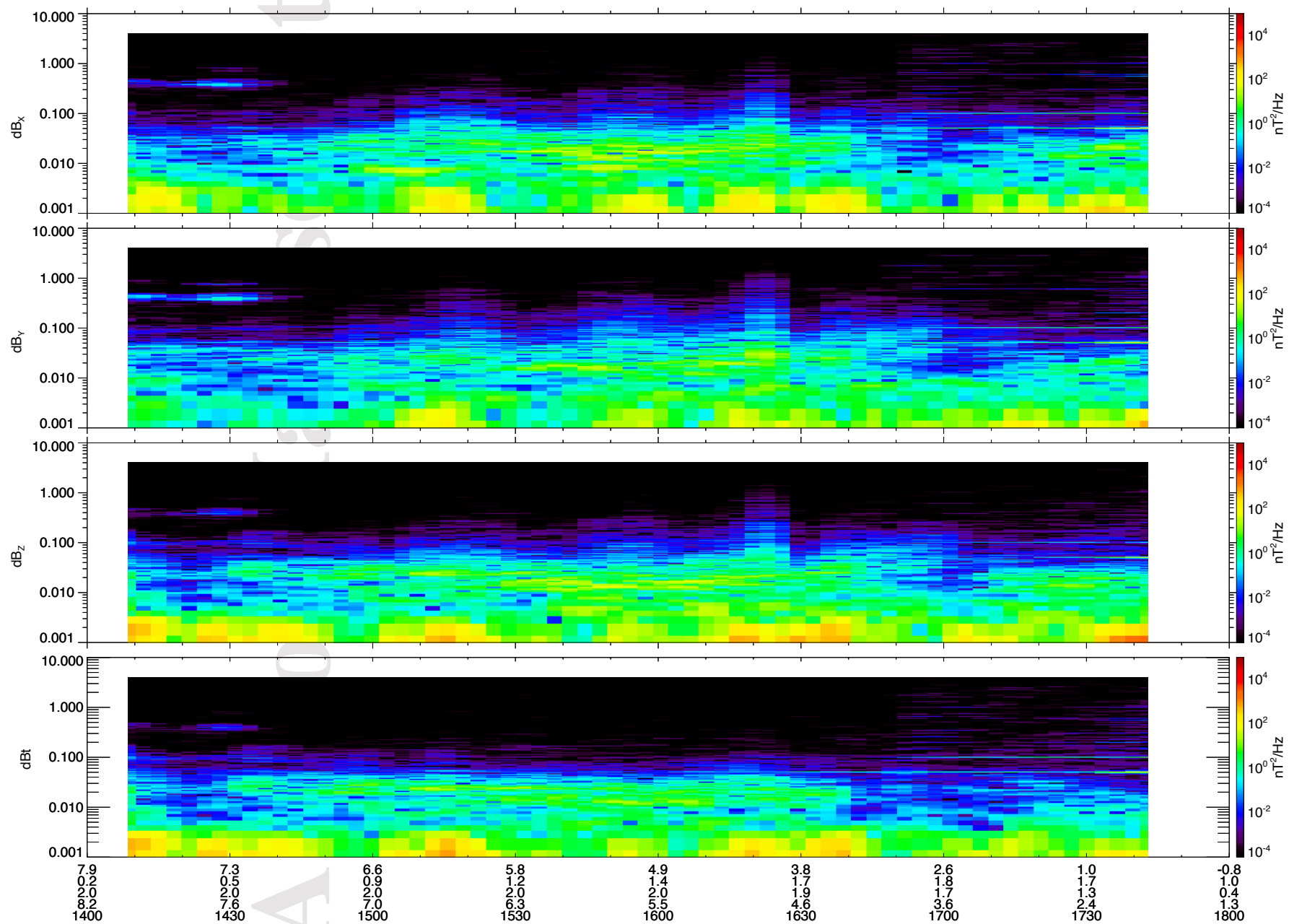
MMS1 Inbound Dynamic Power Spectrum - 2017-01-21



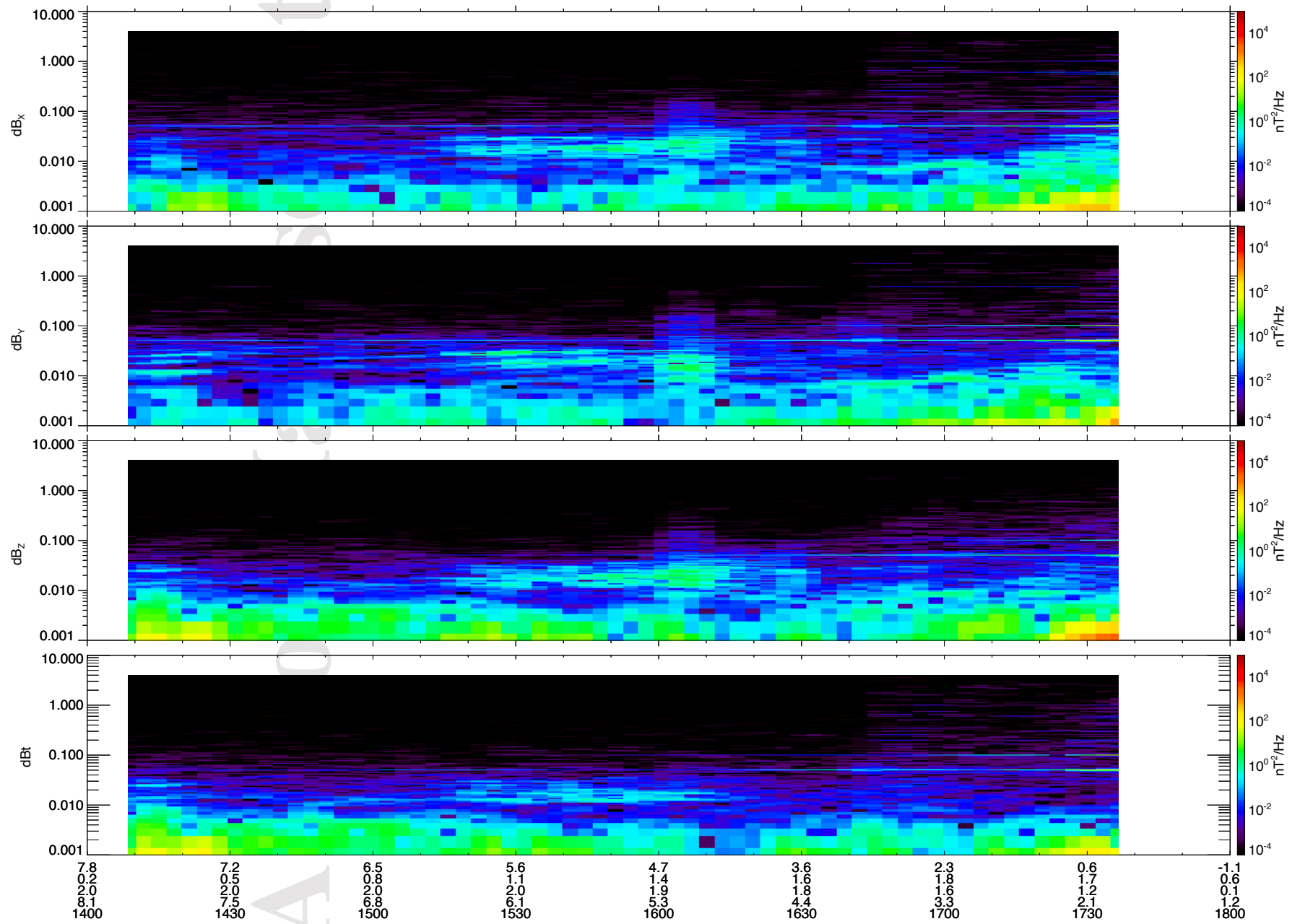
MMS1 Inbound Dynamic Power Spectrum - 2017-01-22



MMS1 Inbound Dynamic Power Spectrum - 2017-01-23

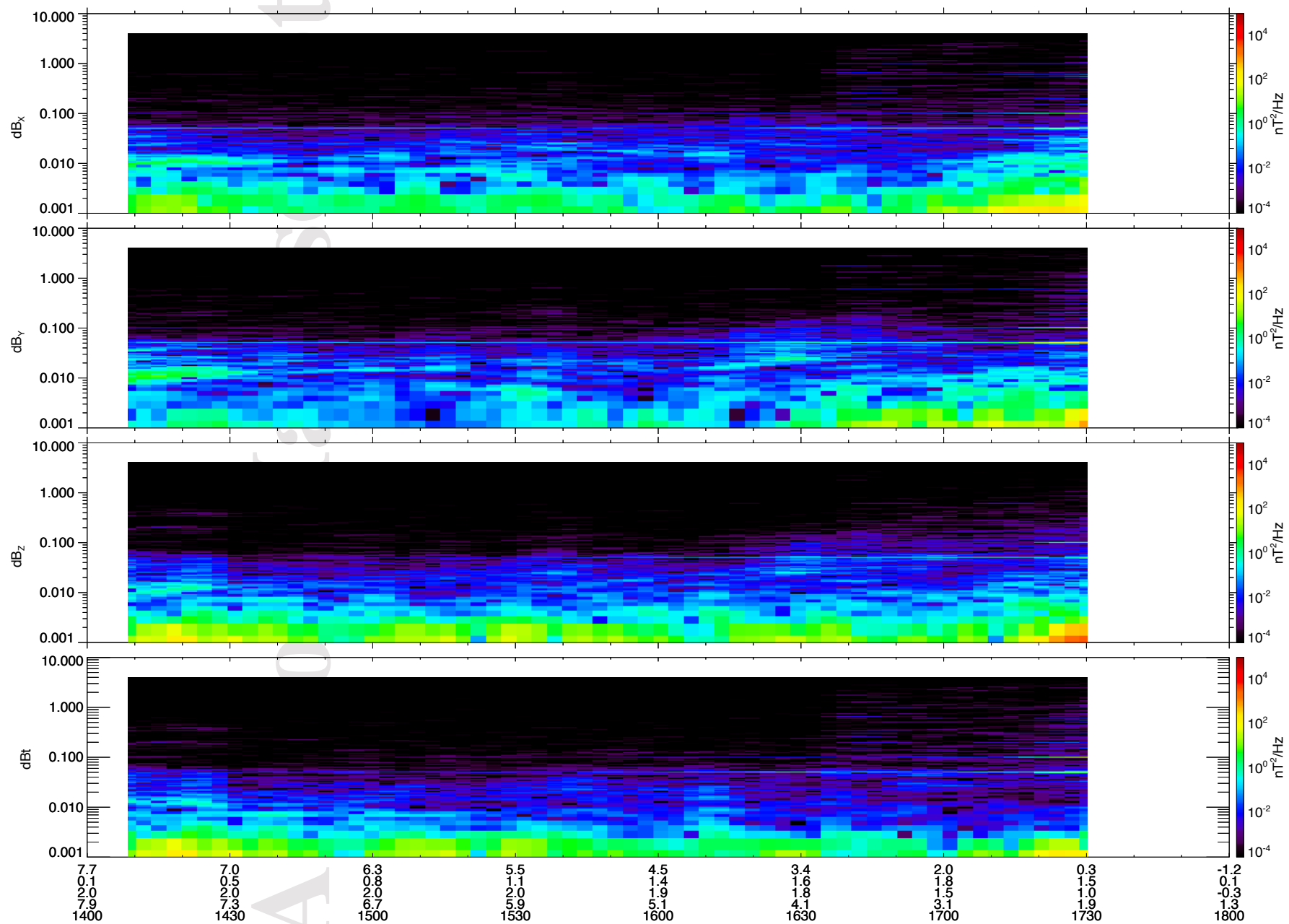


MMS1 Inbound Dynamic Power Spectrum - 2017-01-24

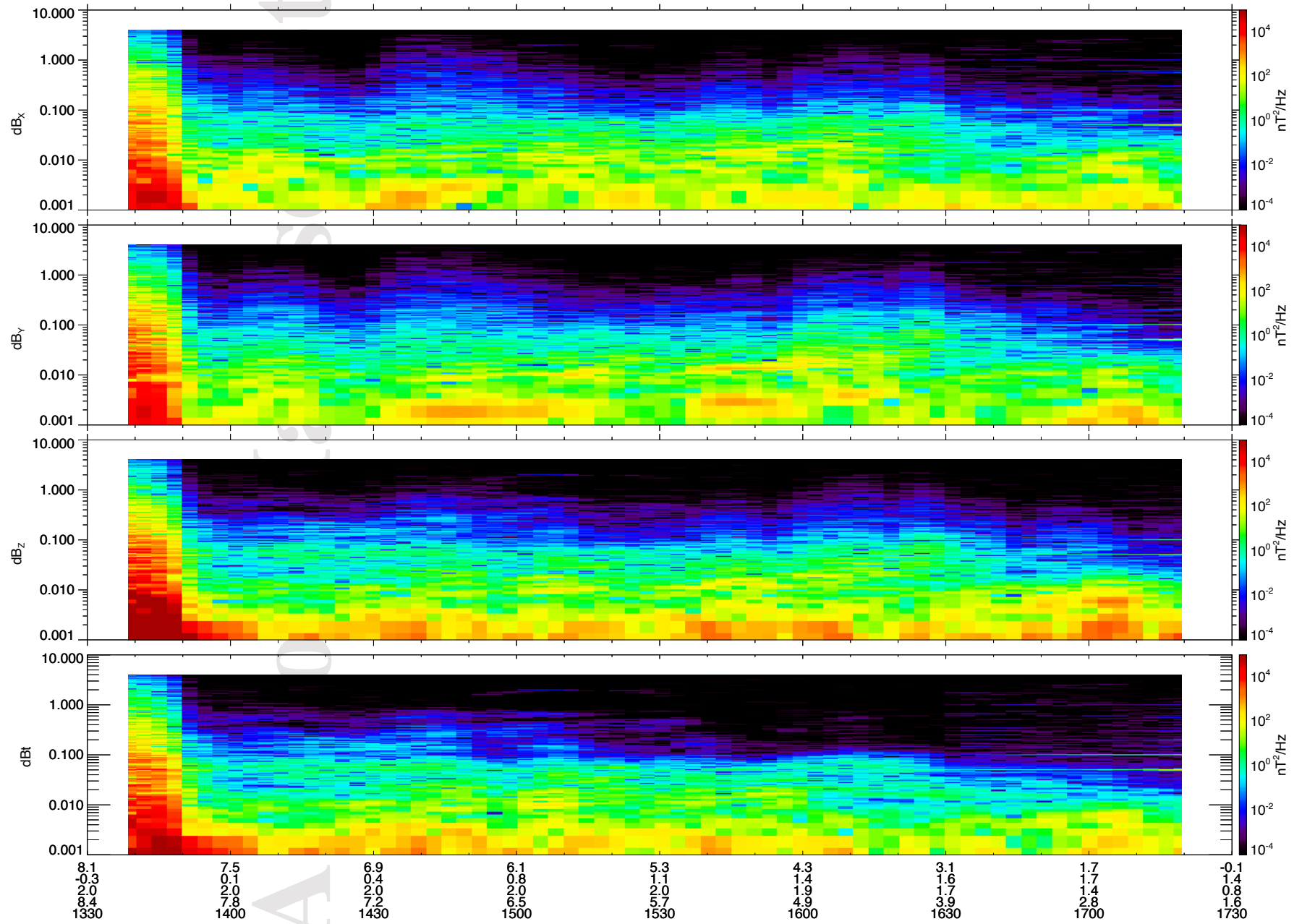




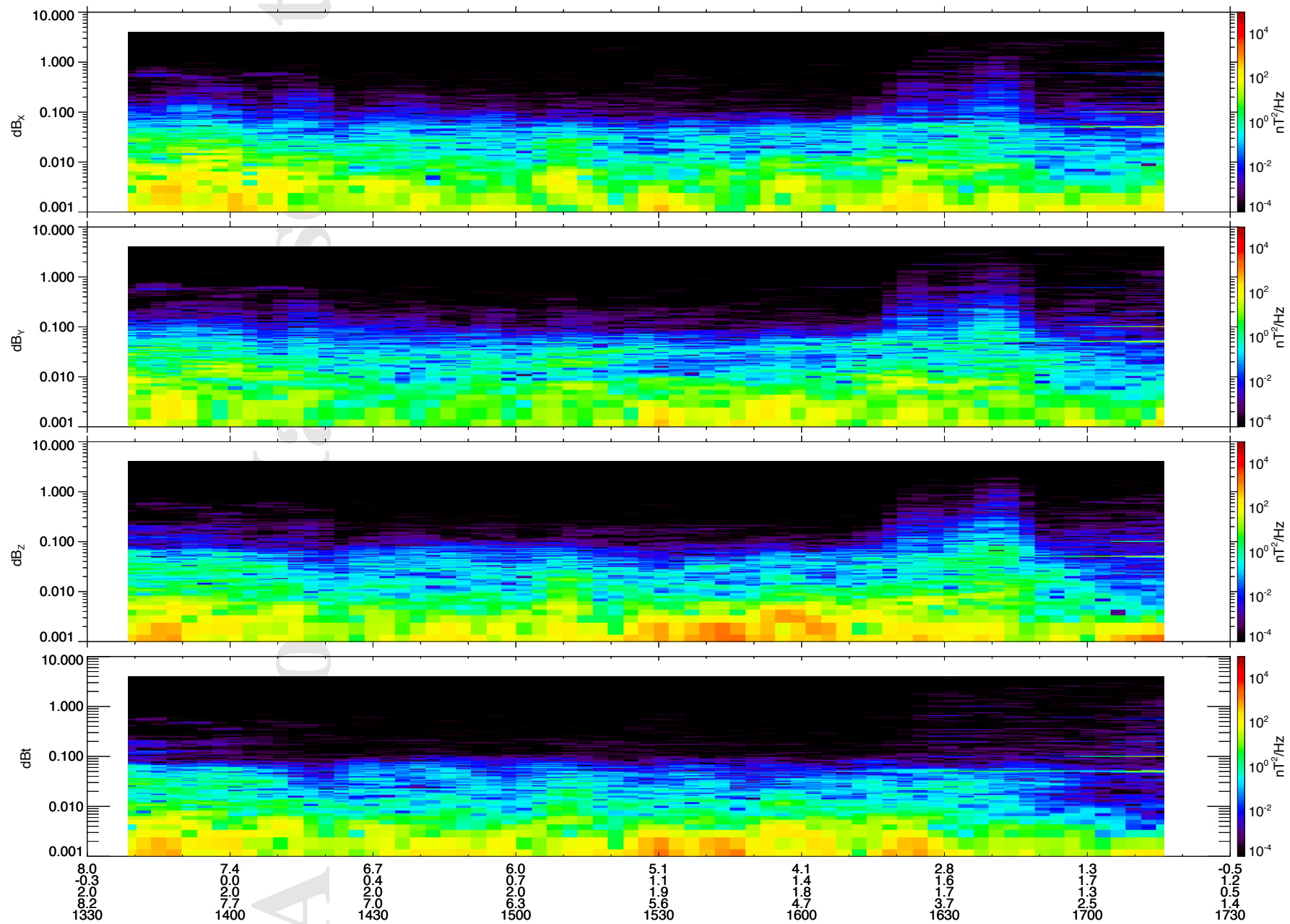
MMS1 Inbound Dynamic Power Spectrum - 2017-01-25



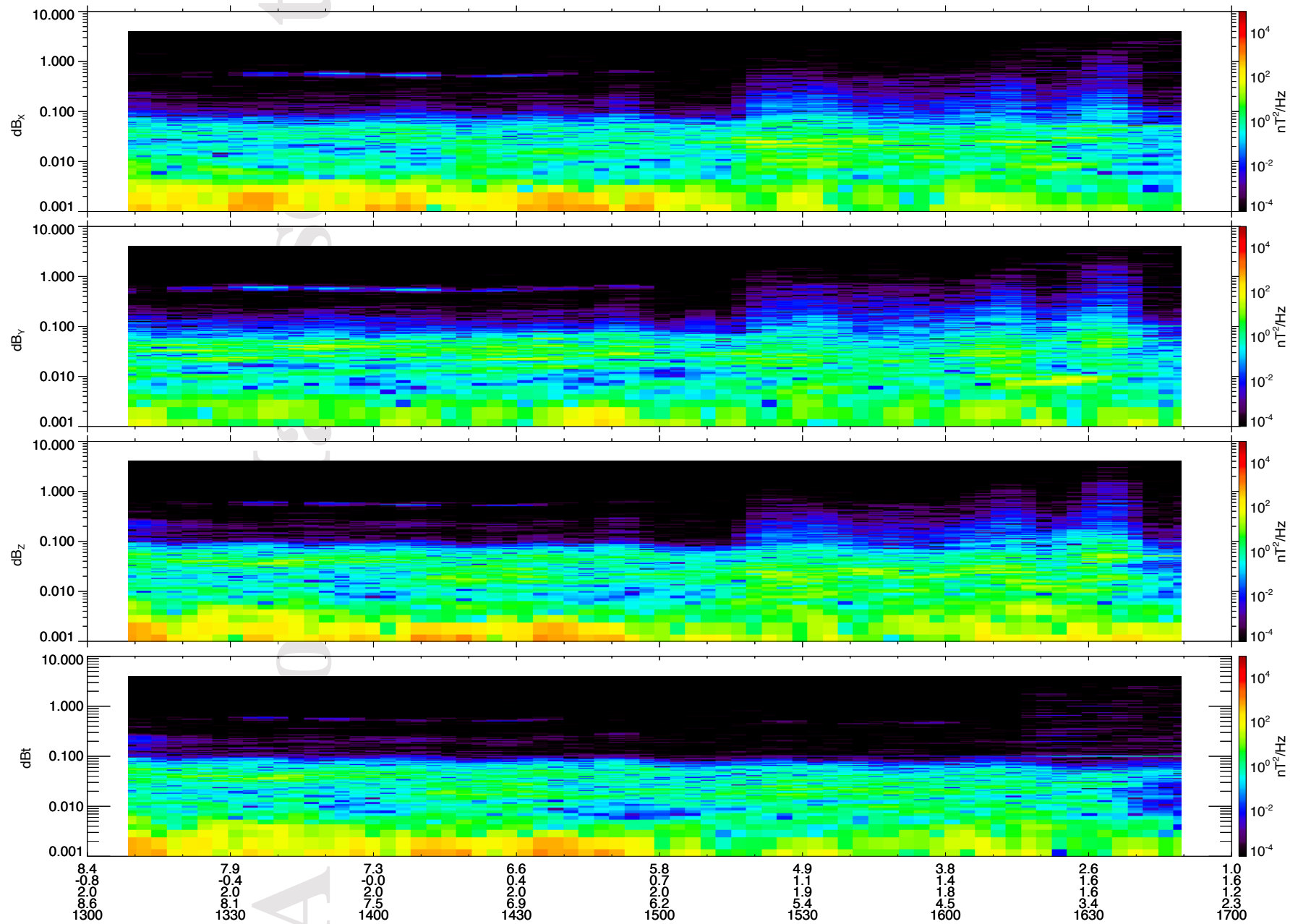
MMS1 Inbound Dynamic Power Spectrum - 2017-01-26



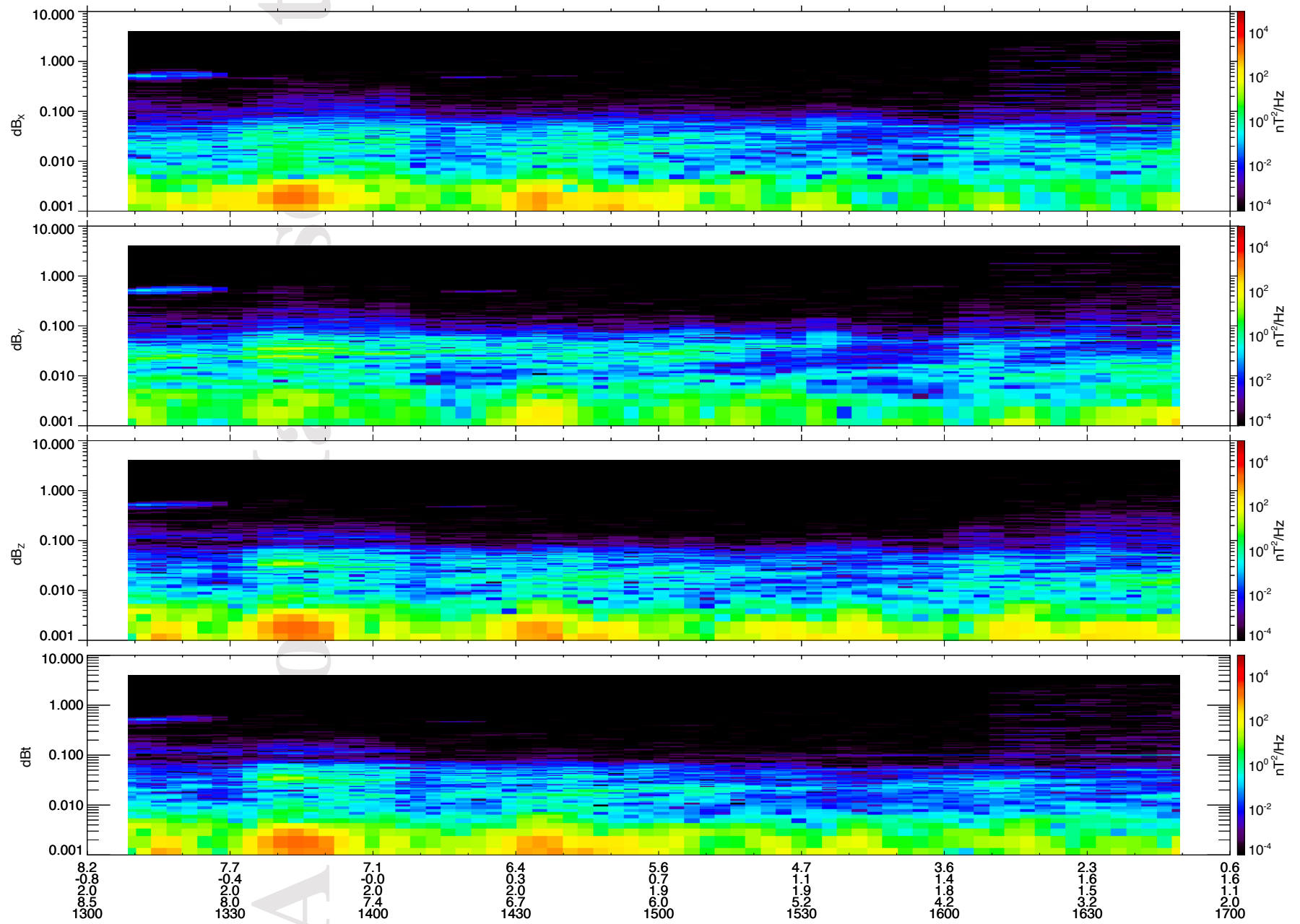
MMS1 Inbound Dynamic Power Spectrum - 2017-01-27



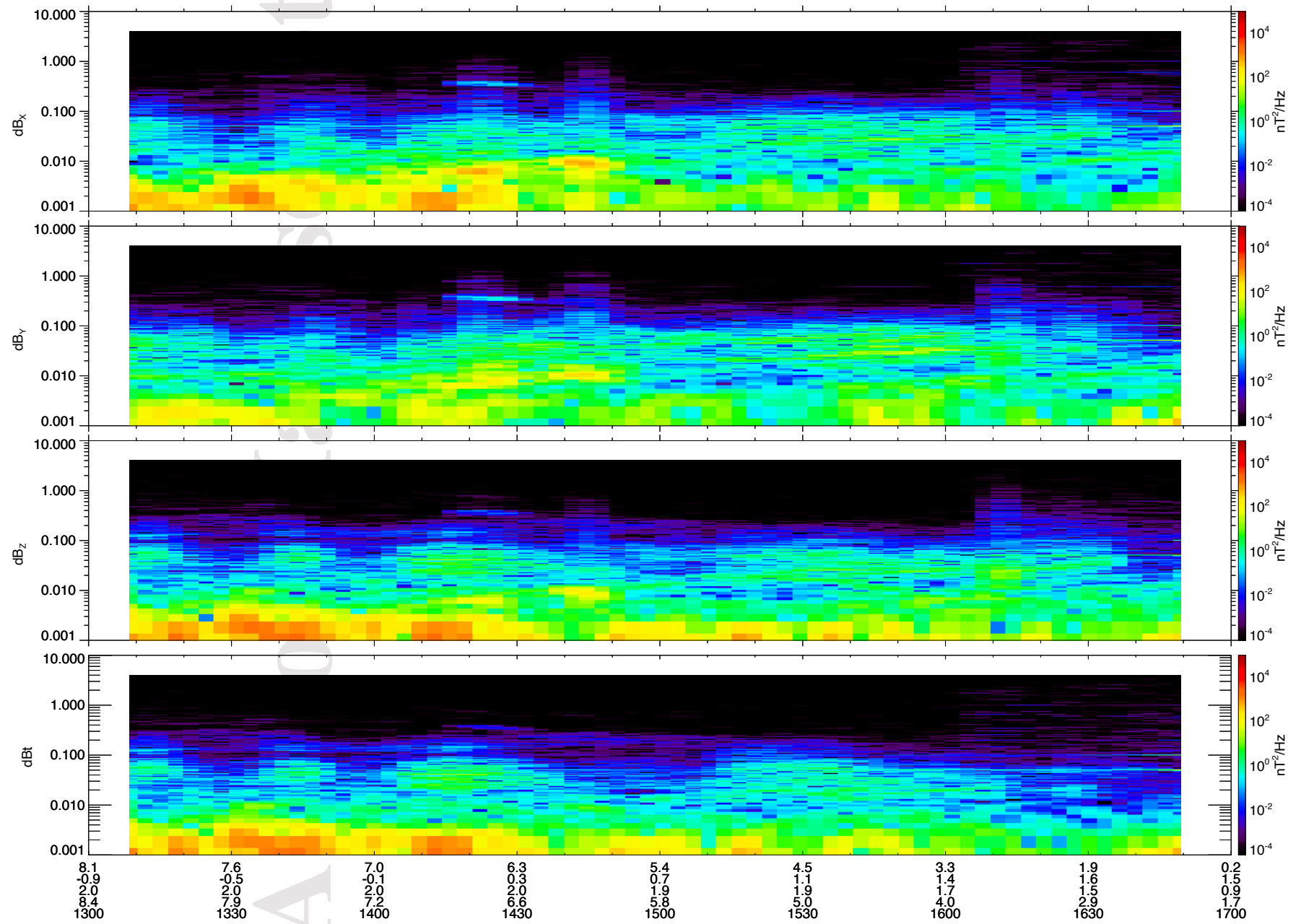
MMS1 Inbound Dynamic Power Spectrum - 2017-01-28



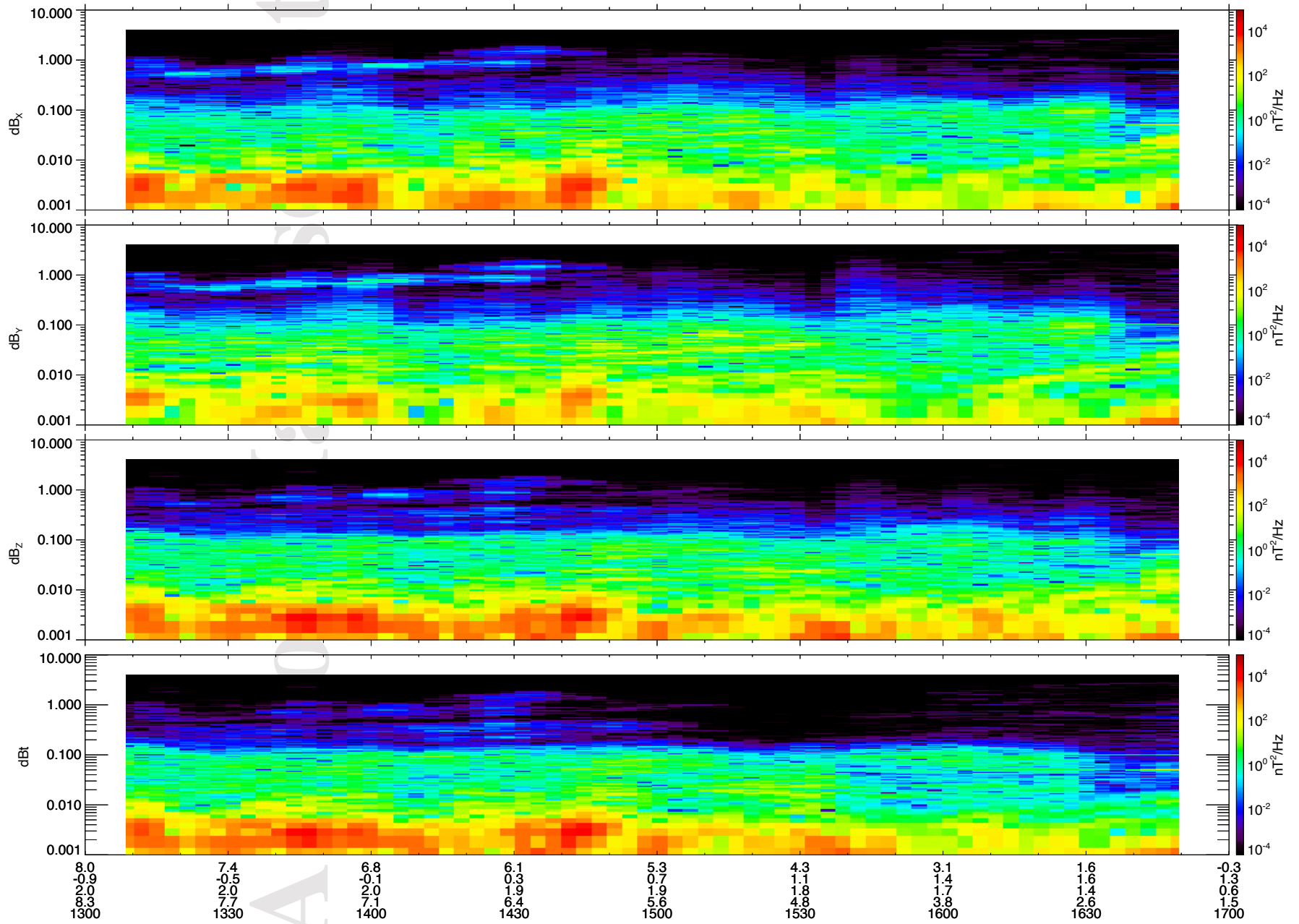
MMS1 Inbound Dynamic Power Spectrum - 2017-01-29



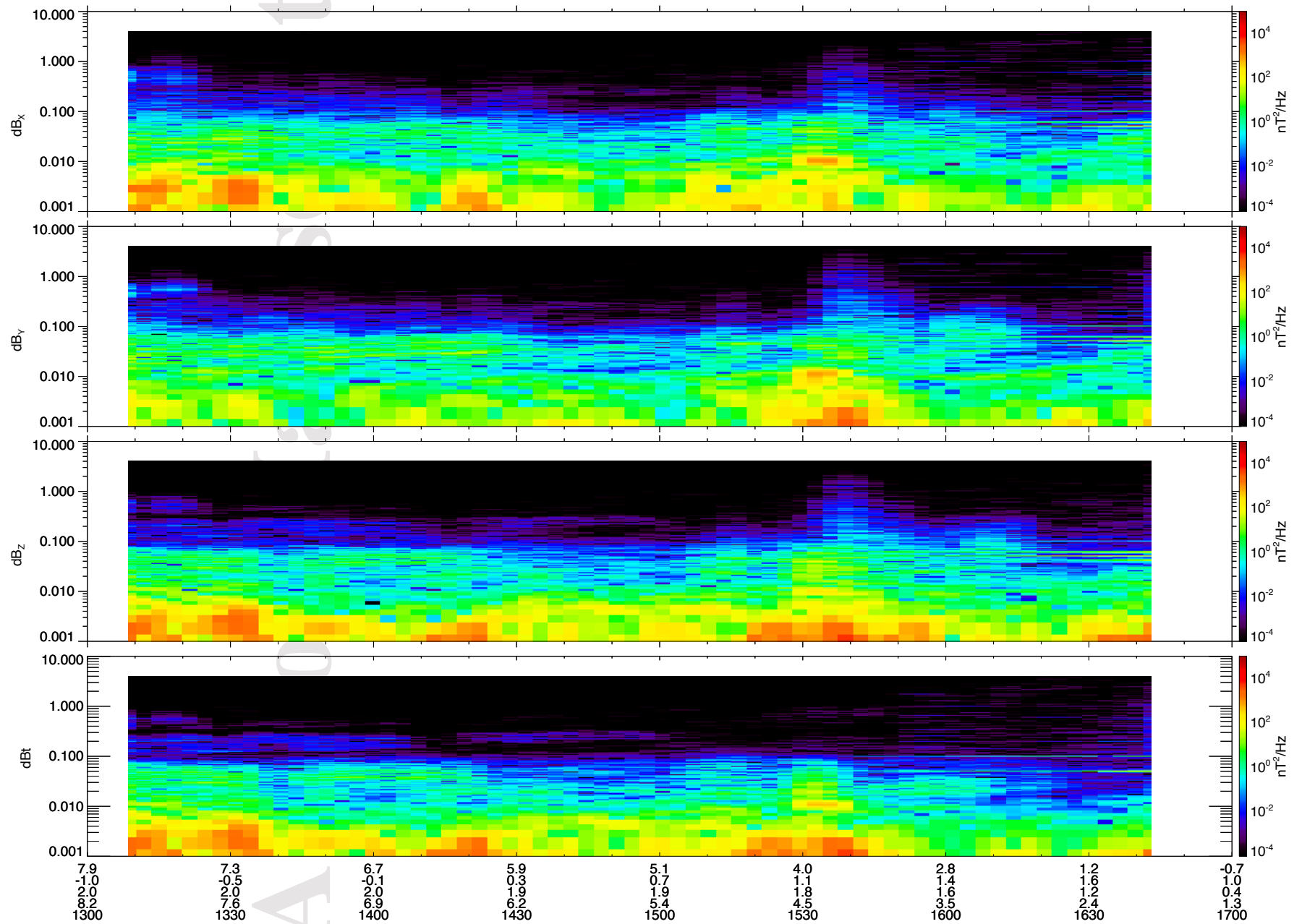
MMS1 Inbound Dynamic Power Spectrum - 2017-01-30



MMS1 Inbound Dynamic Power Spectrum - 2017-01-31

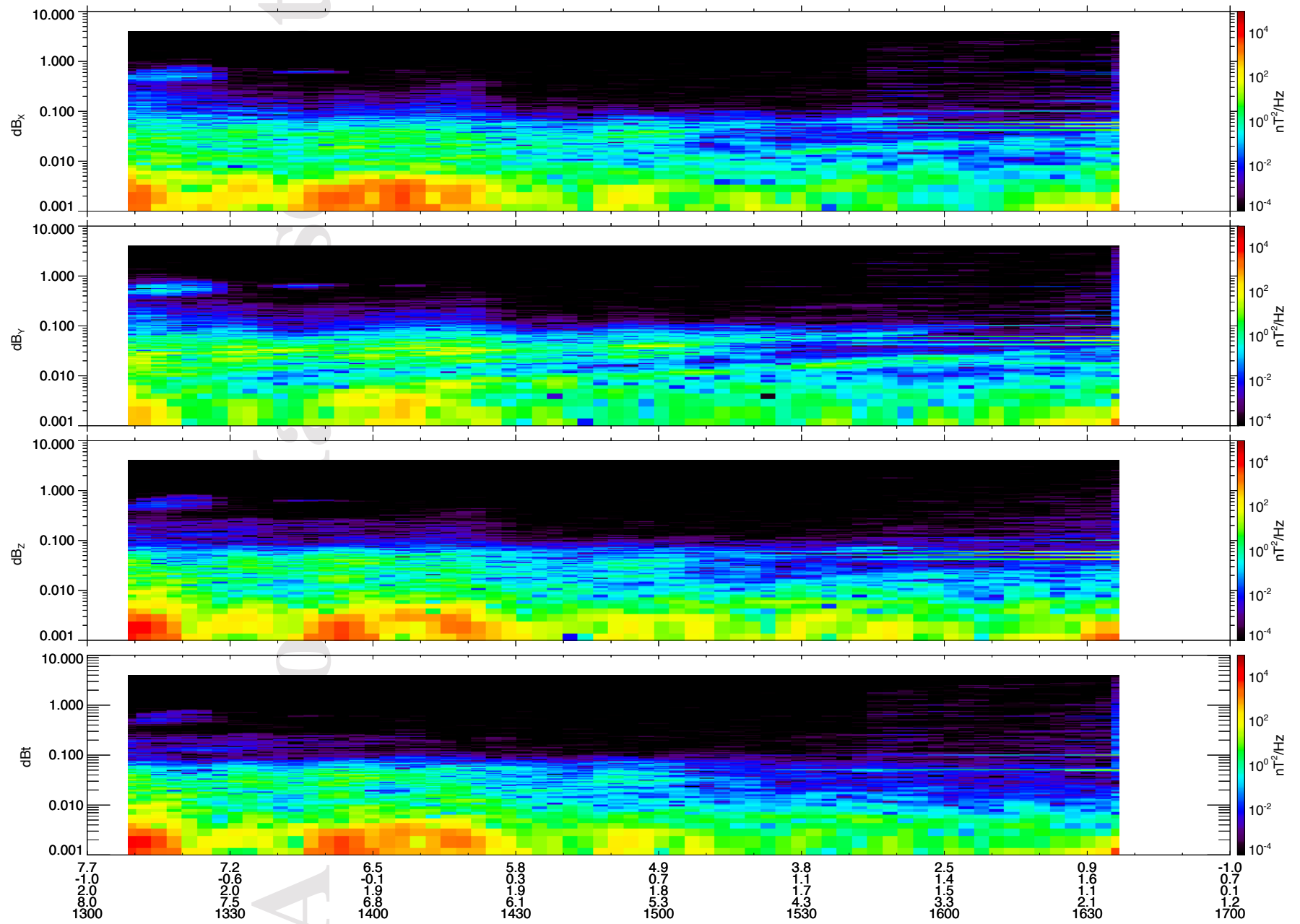


MMS1 Inbound Dynamic Power Spectrum - 2017-02-01

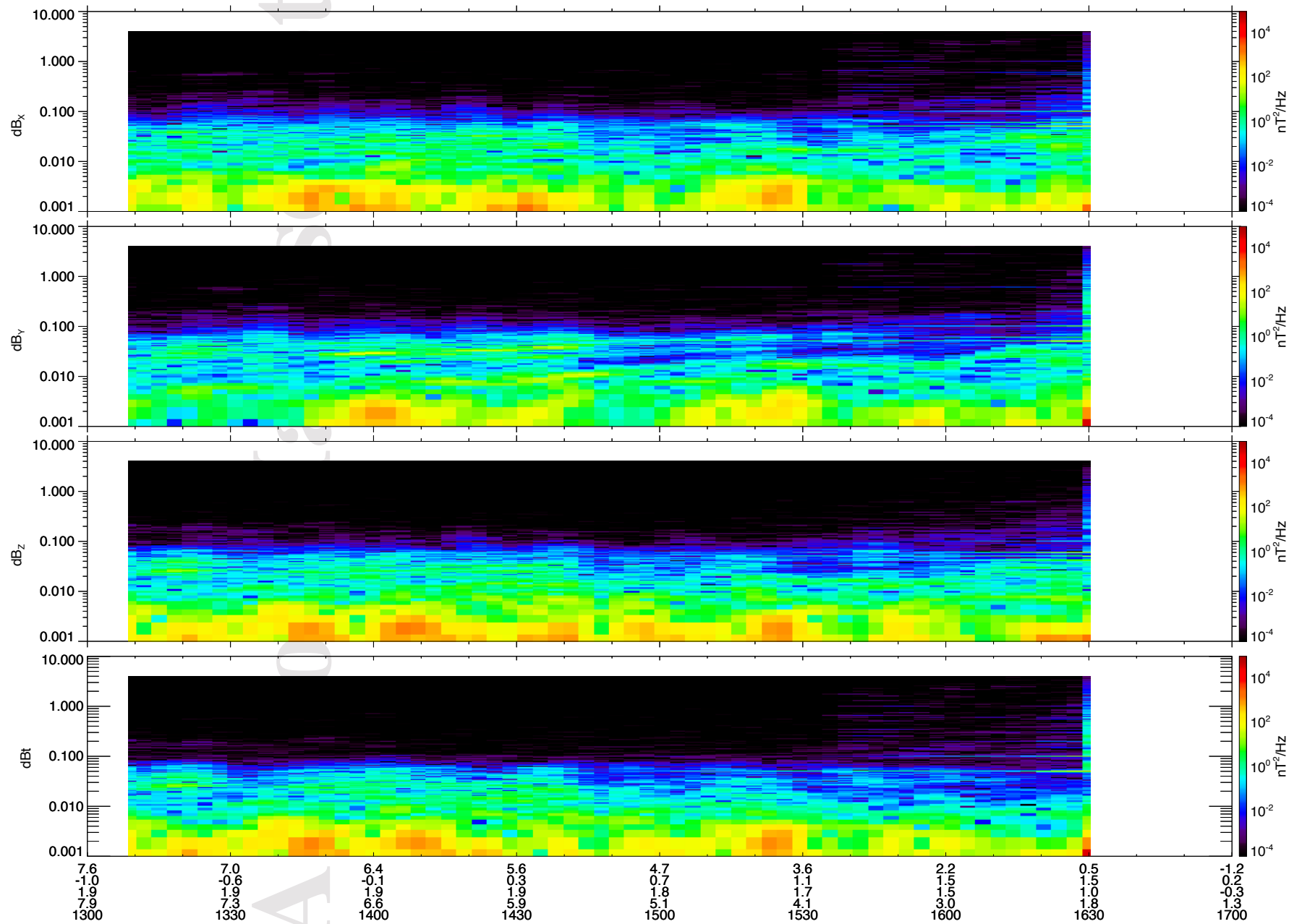




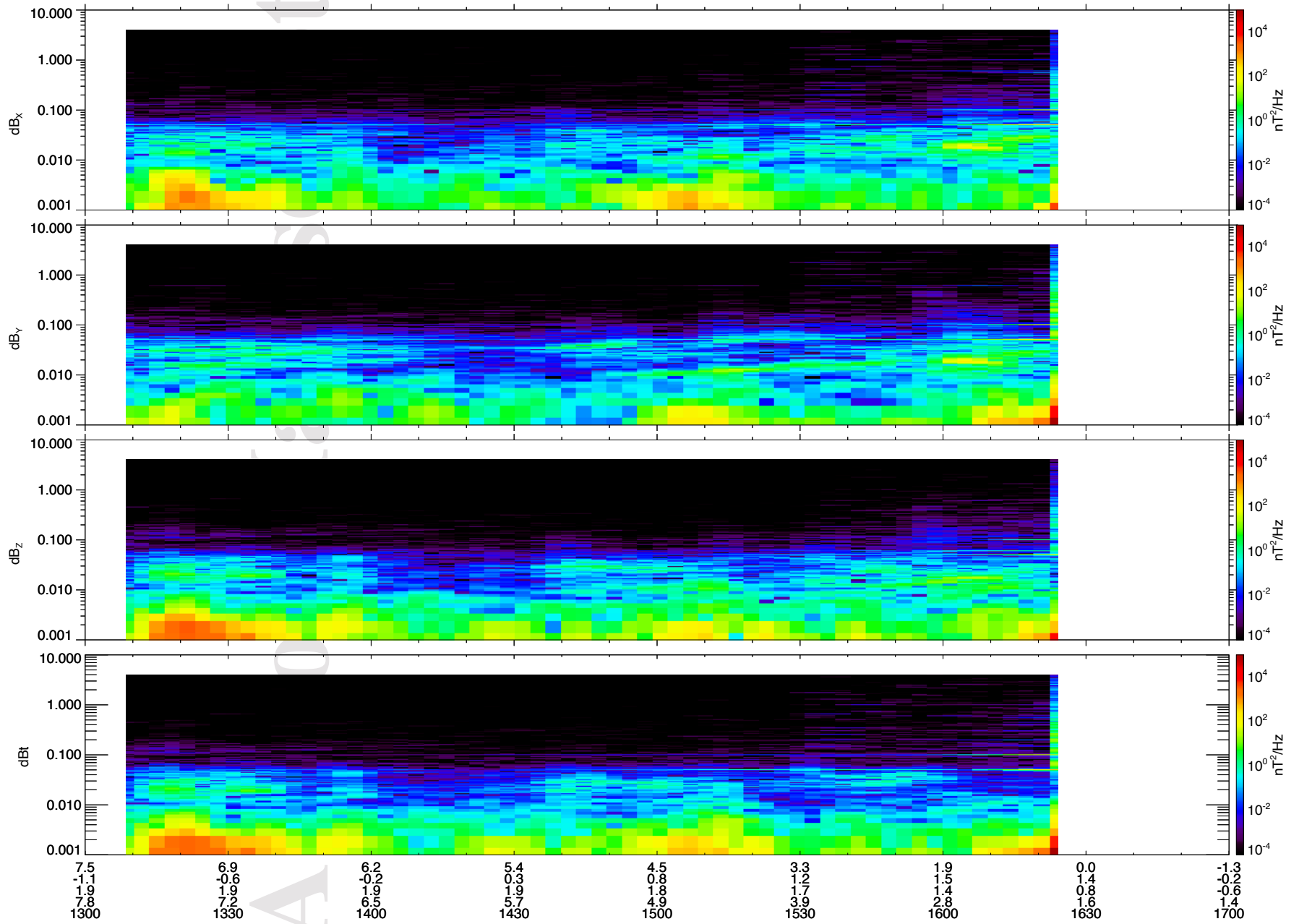
MMS1 Inbound Dynamic Power Spectrum - 2017-02-02



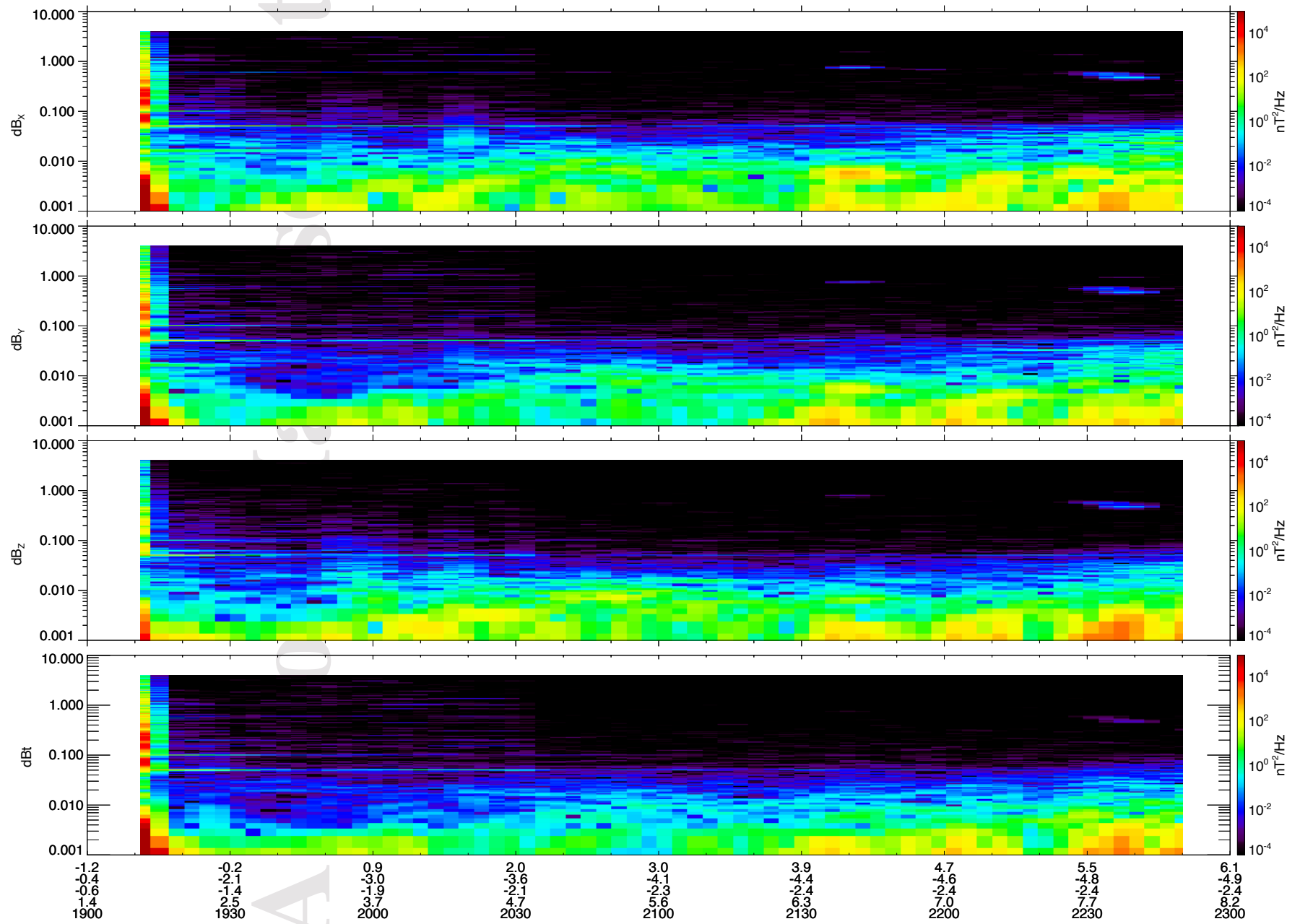
MMS1 Inbound Dynamic Power Spectrum - 2017-02-03



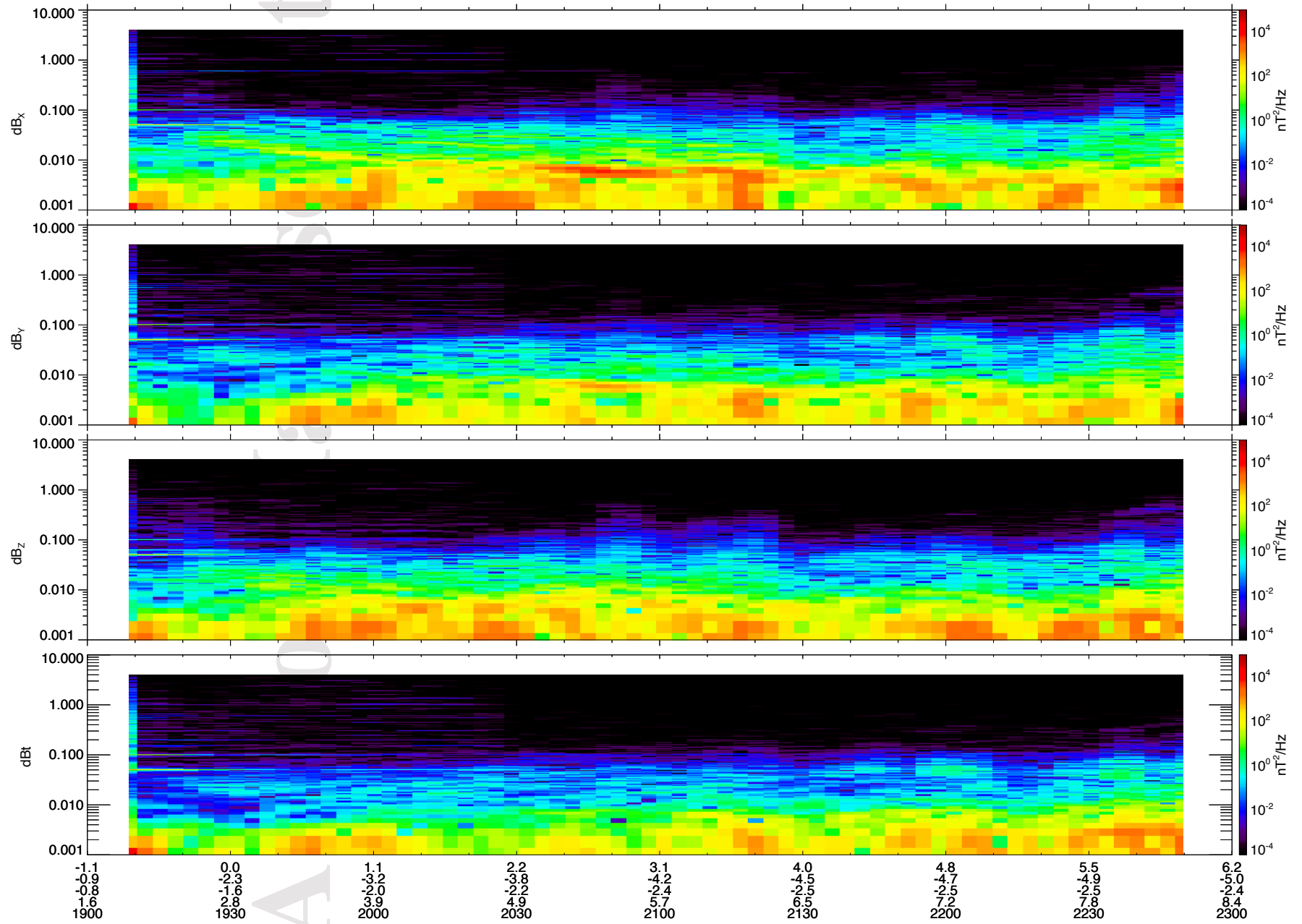
MMS1 Inbound Dynamic Power Spectrum - 2017-02-04



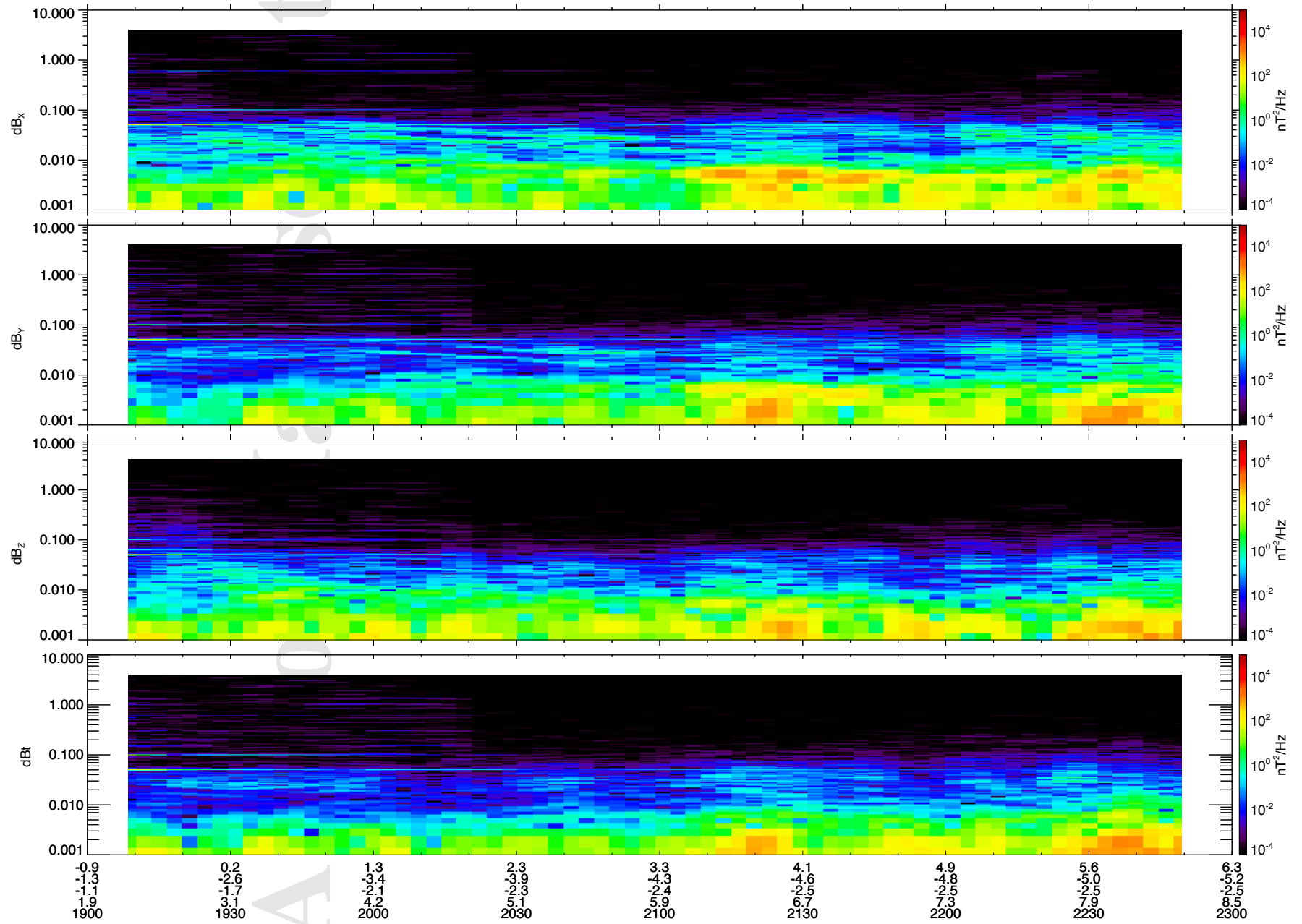
MMS1 Outbound Dynamic Power Spectrum 2017-01-17



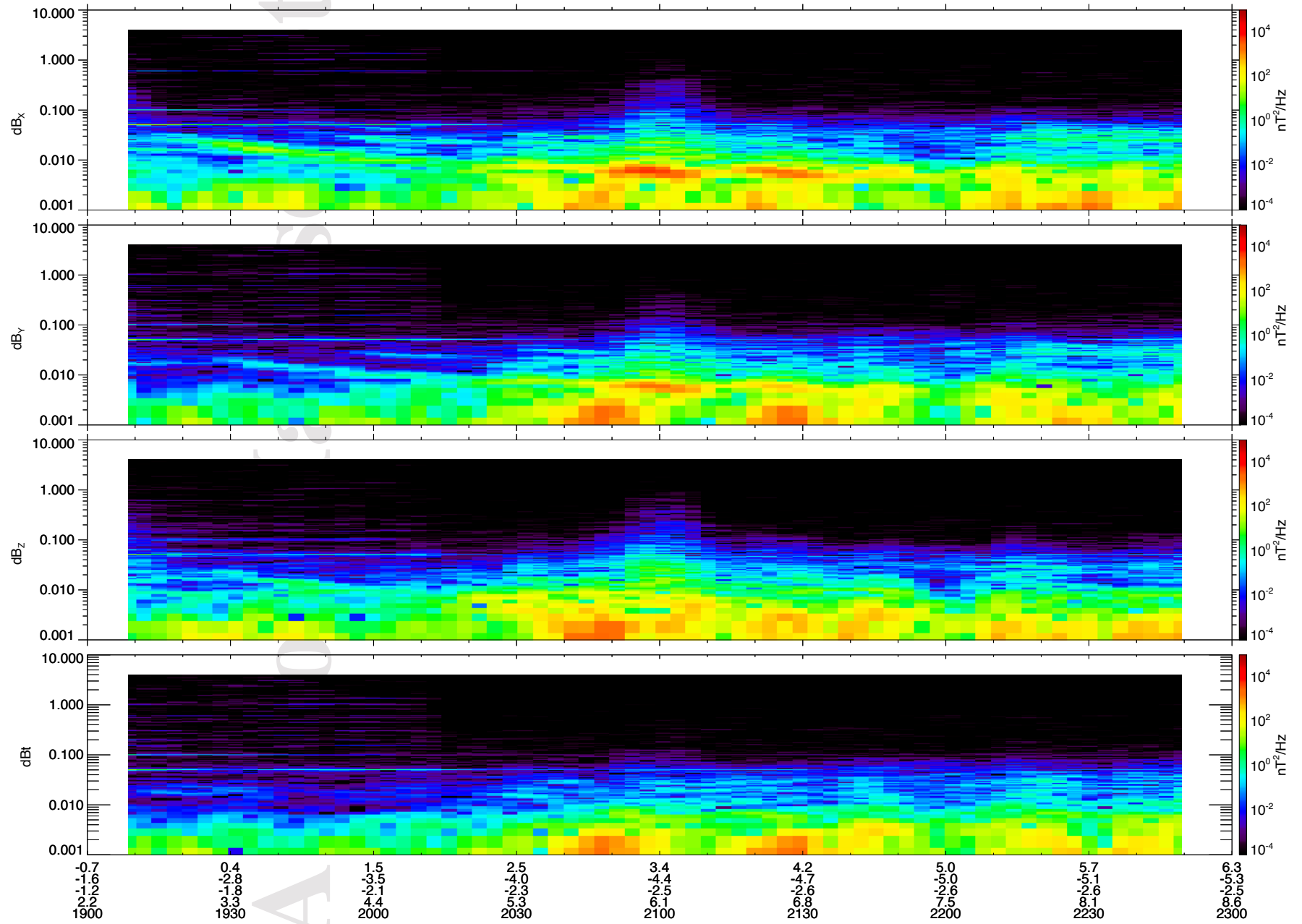
MMS1 Outbound Dynamic Power Spectrum 2017-01-18



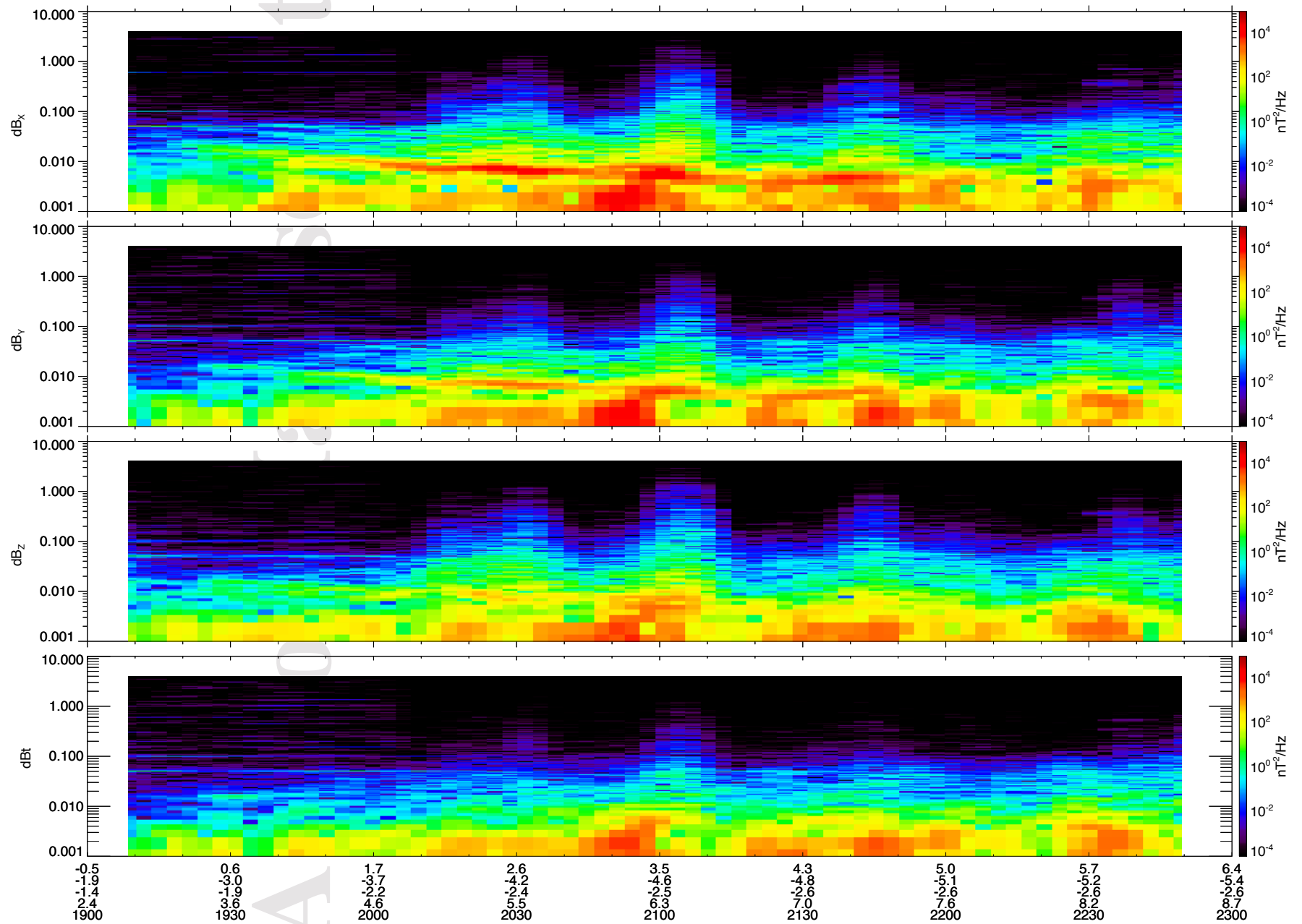
MMS1 Outbound Dynamic Power Spectrum 2017-01-19



MMS1 Outbound Dynamic Power Spectrum 2017-01-20

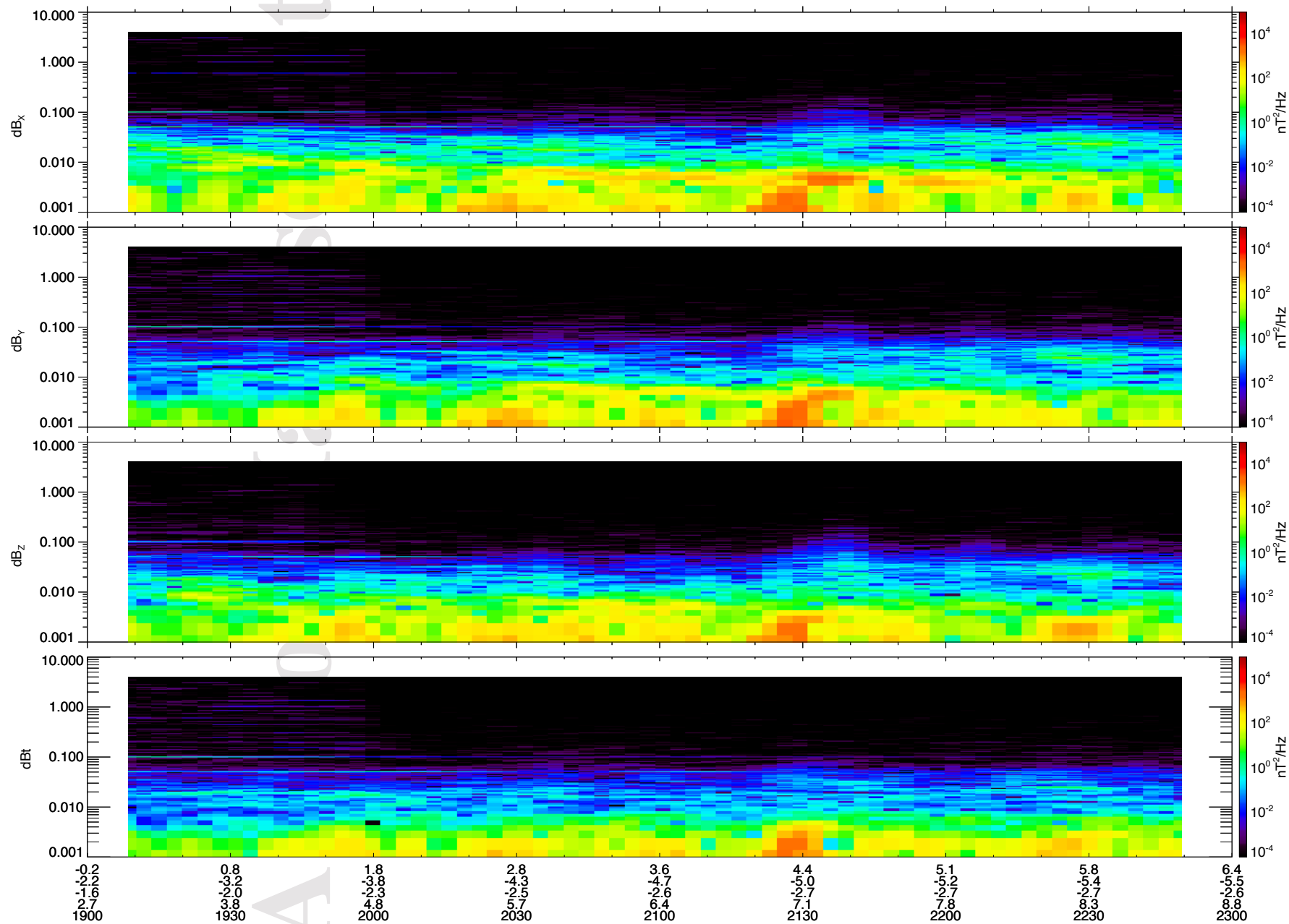


MMS1 Outbound Dynamic Power Spectrum 2017-01-21

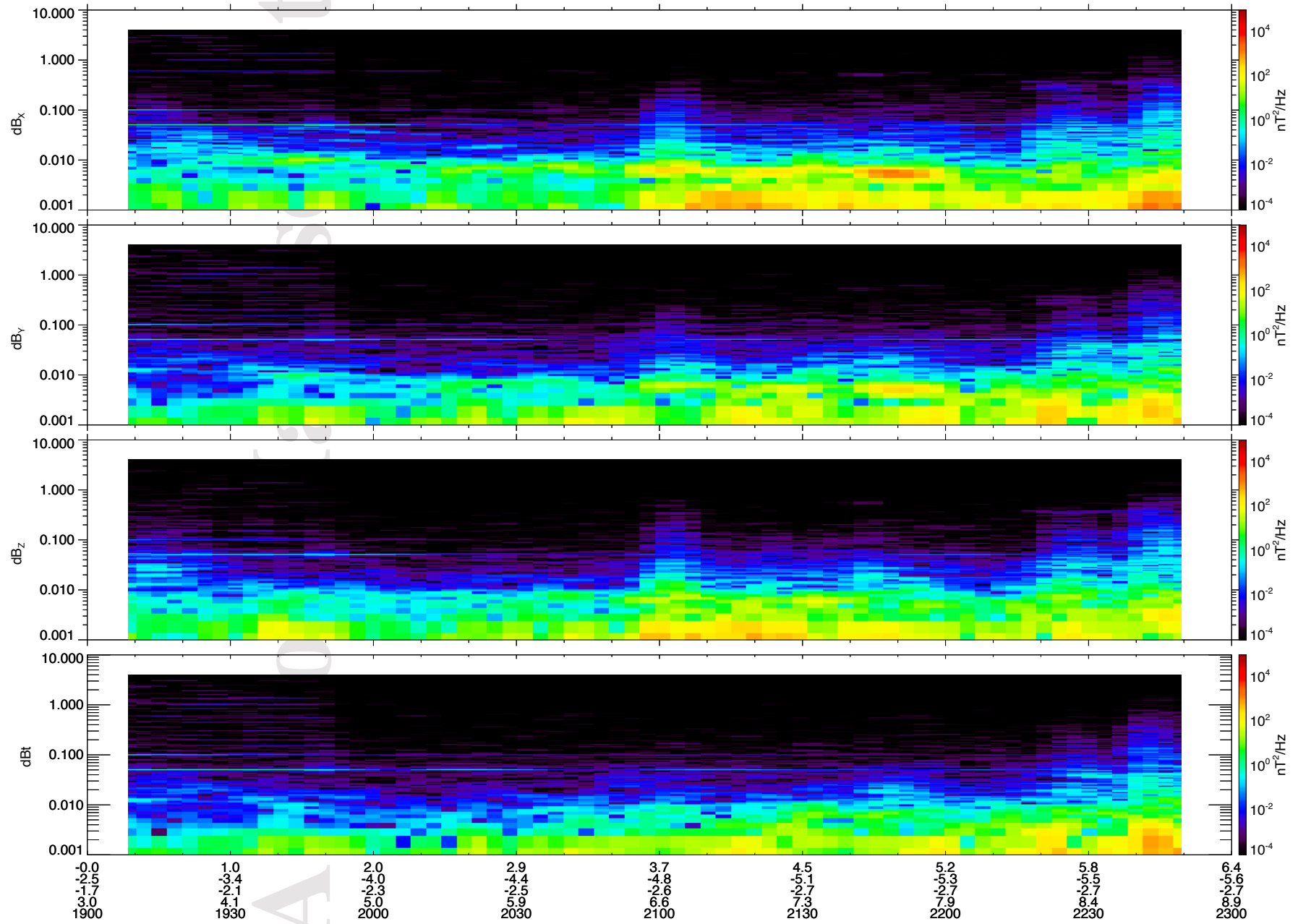




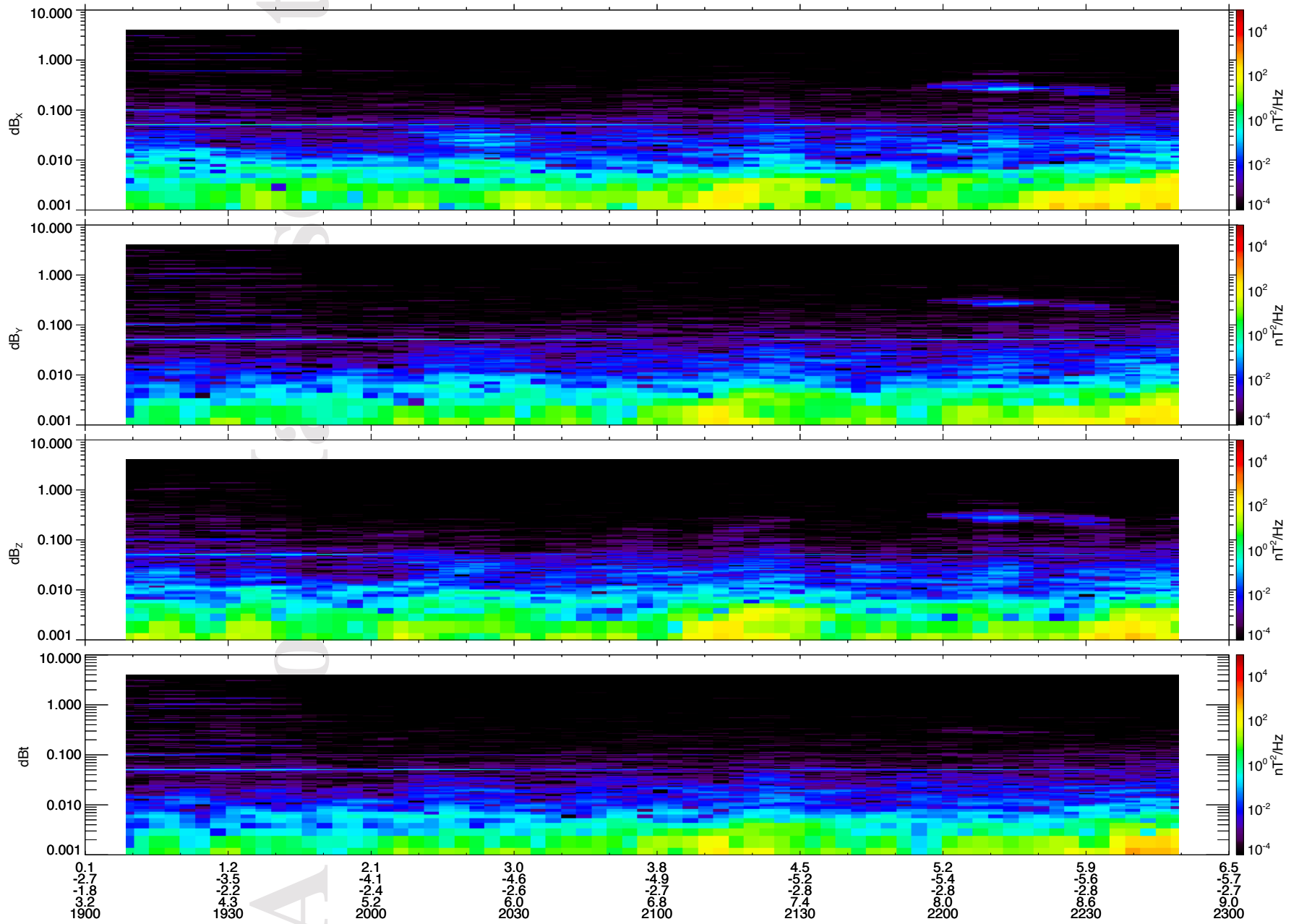
MMS1 Outbound Dynamic Power Spectrum 2017-01-22



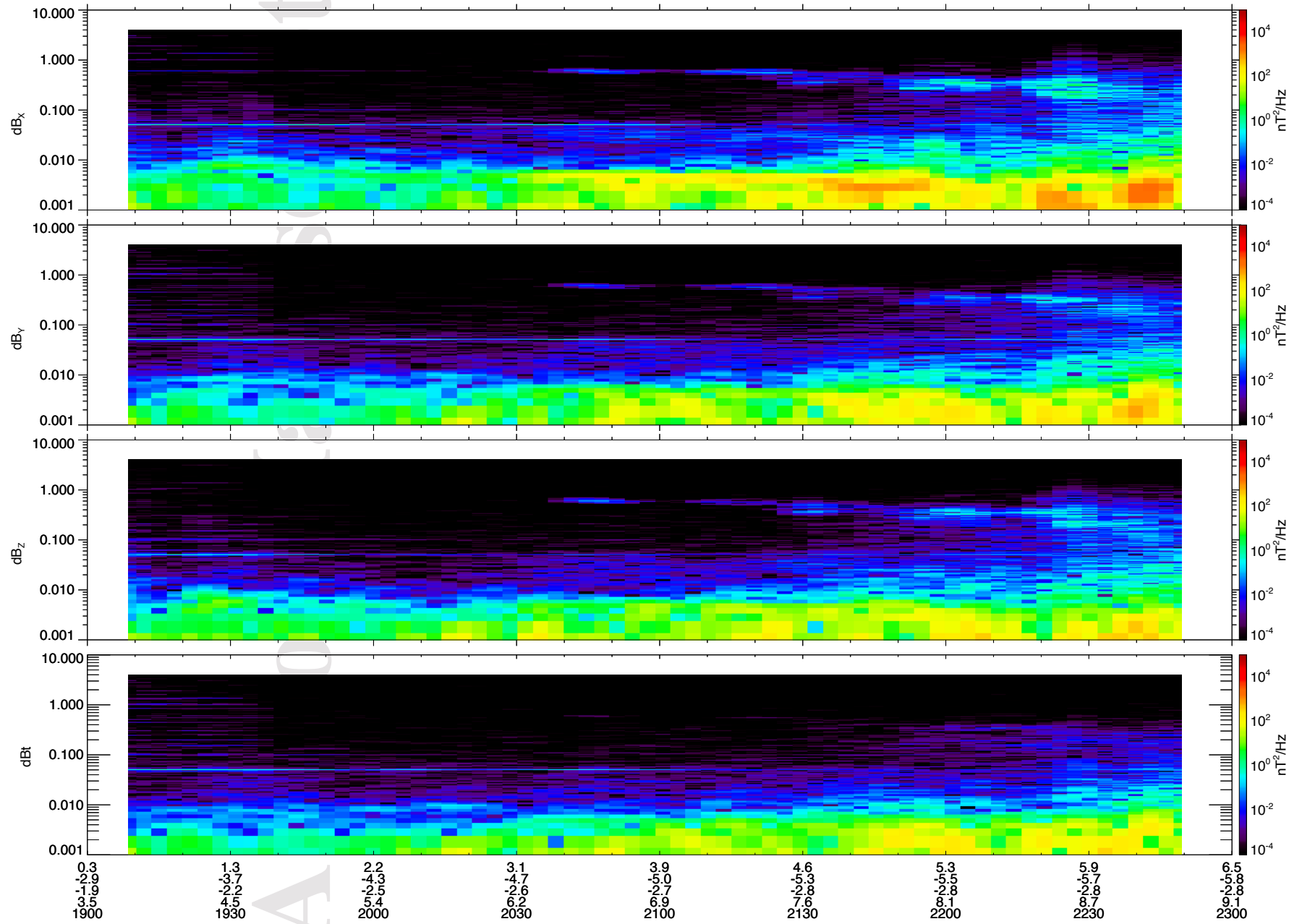
MMS1 Outbound Dynamic Power Spectrum 2017-01-23



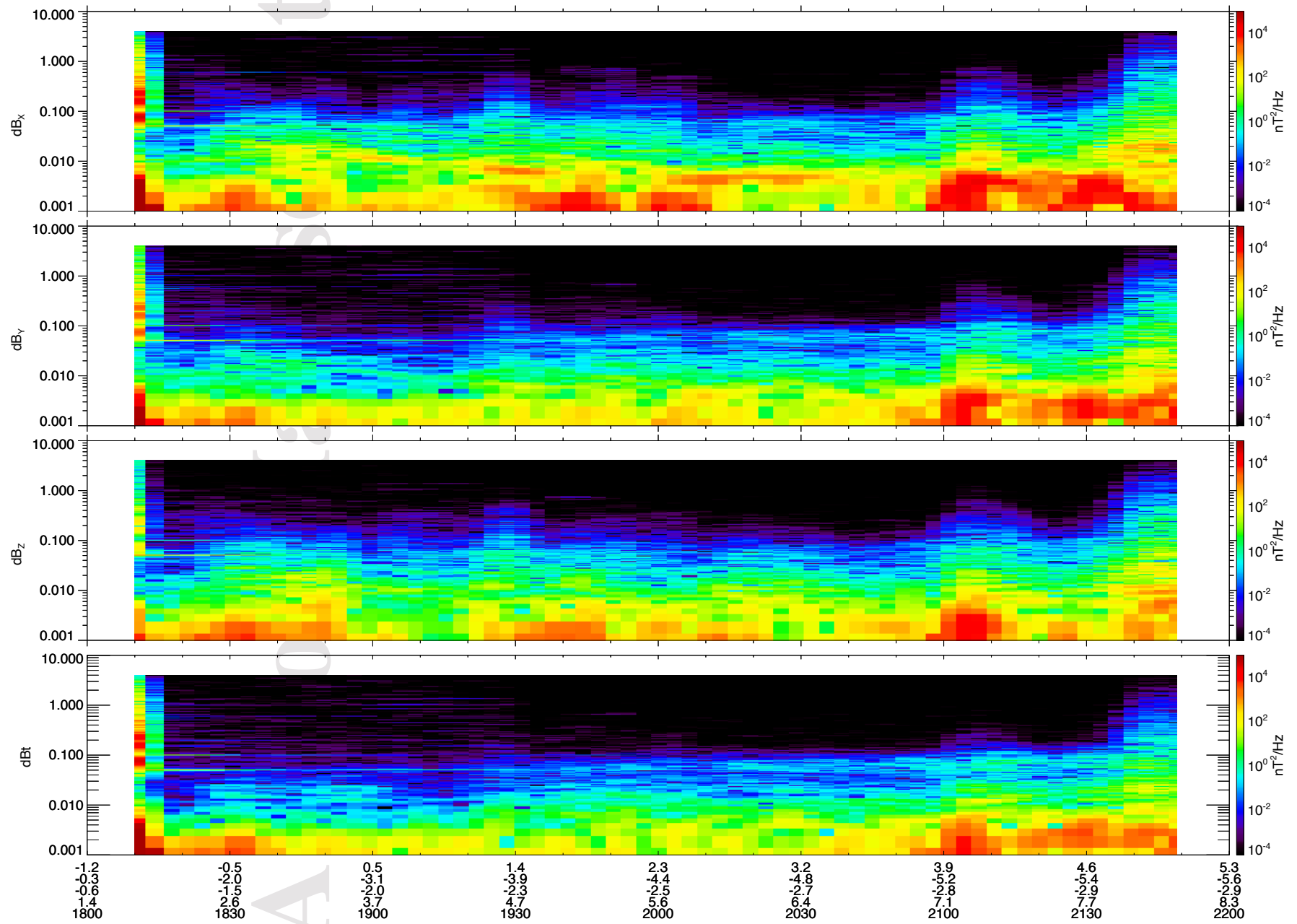
MMS1 Outbound Dynamic Power Spectrum 2017-01-24



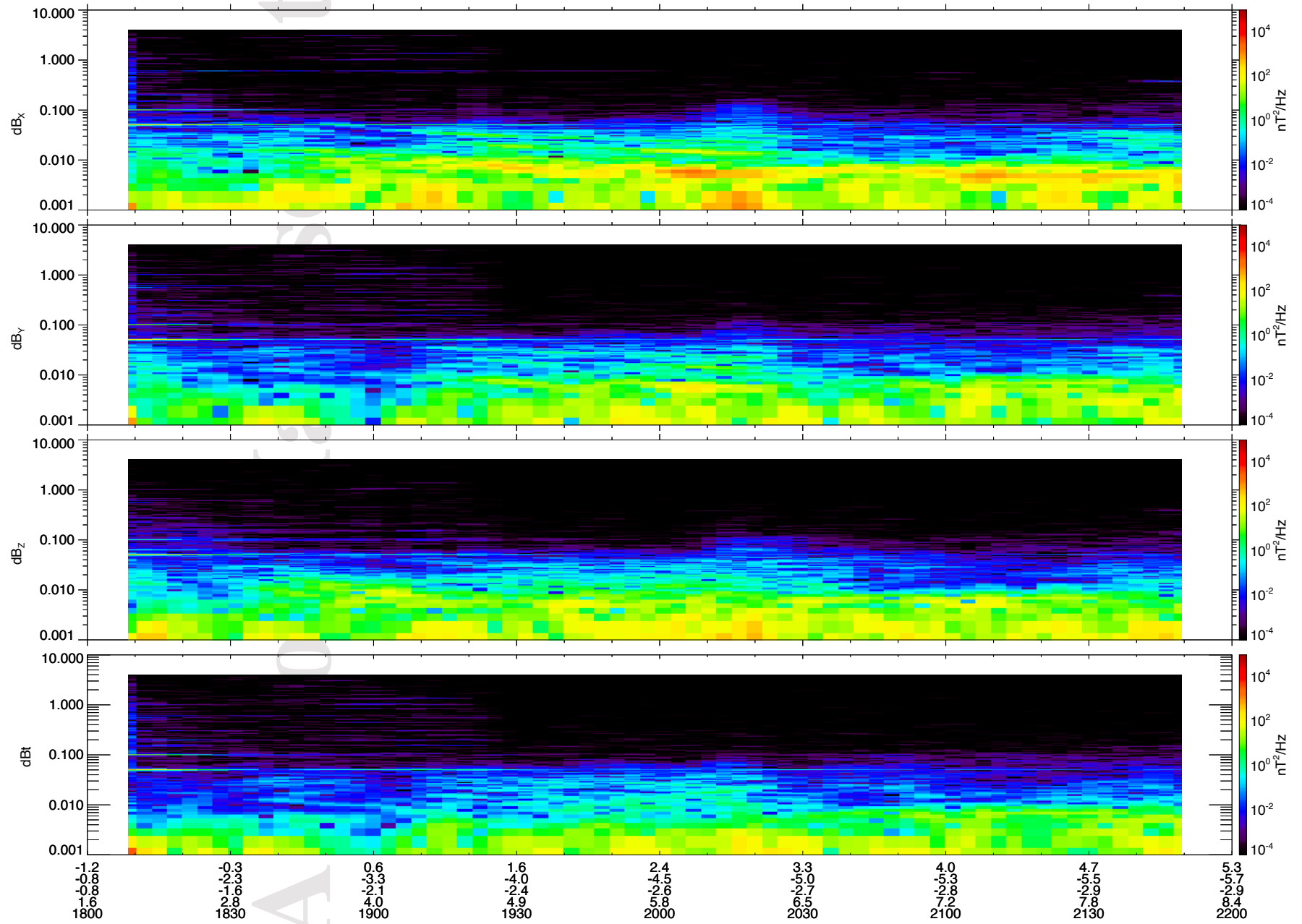
MMS1 Outbound Dynamic Power Spectrum 2017-01-25



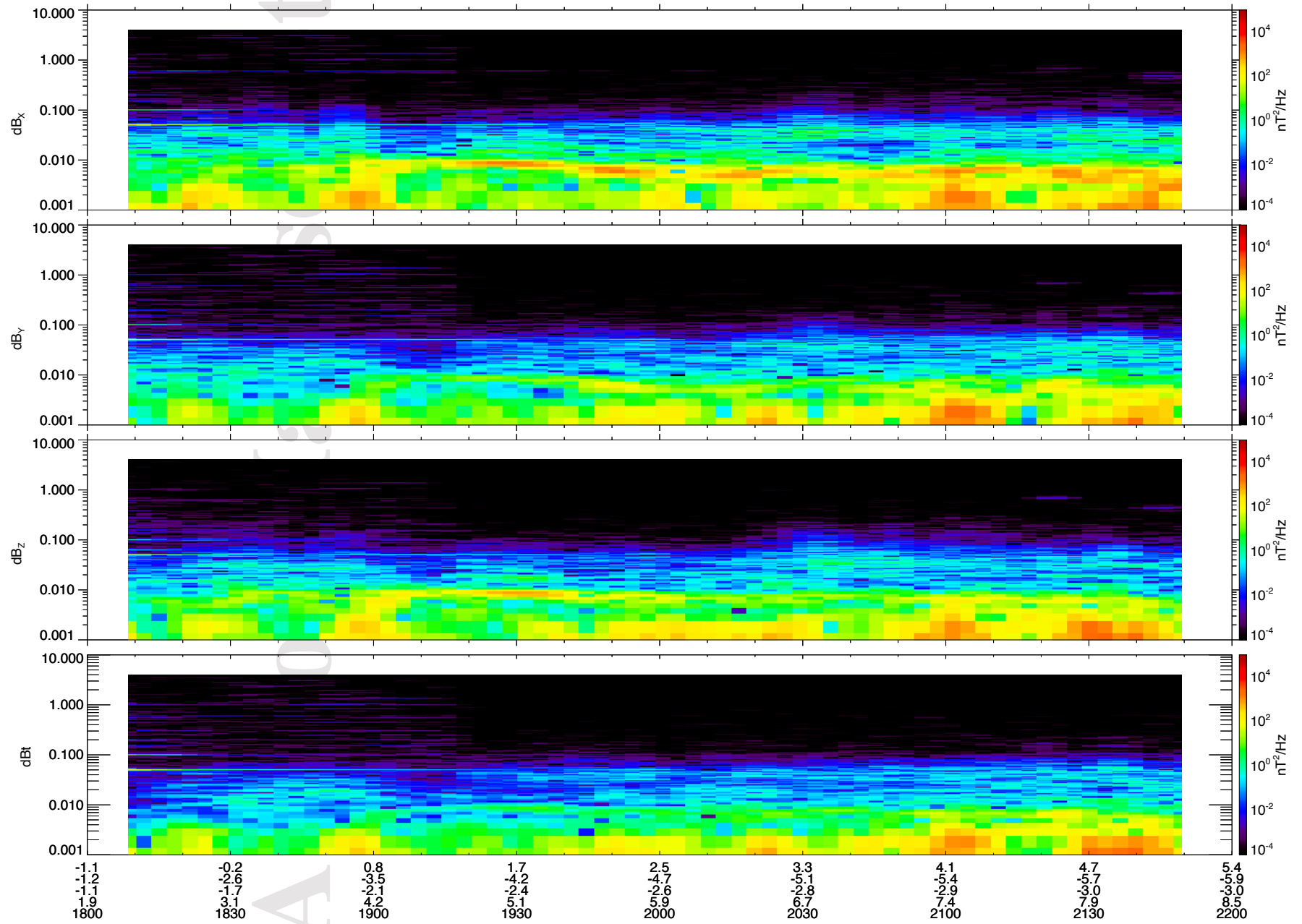
MMS1 Outbound Dynamic Power Spectrum 2017-01-26



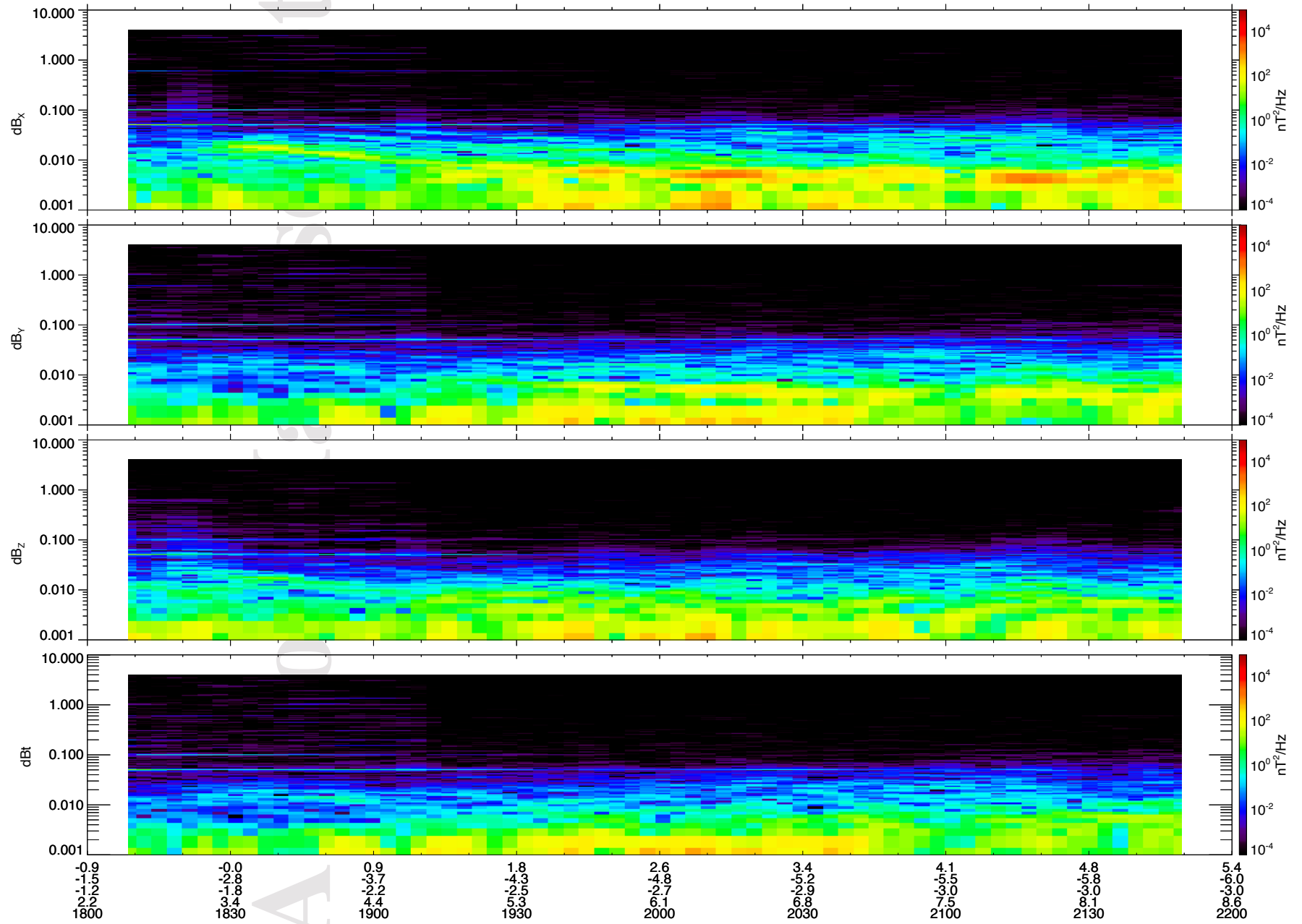
MMS1 Outbound Dynamic Power Spectrum 2017-01-27



MMS1 Outbound Dynamic Power Spectrum 2017-01-28

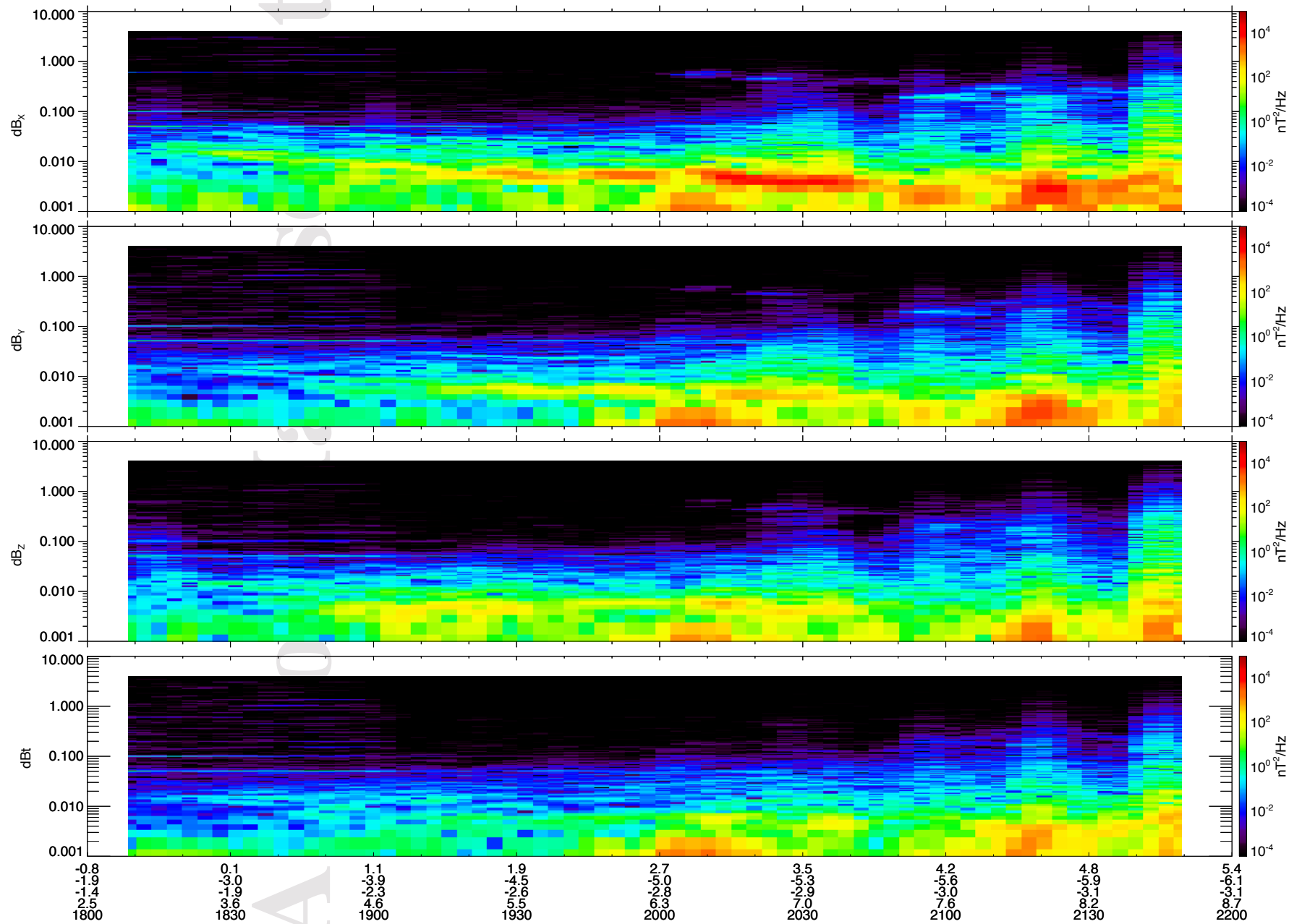


MMS1 Outbound Dynamic Power Spectrum 2017-01-29

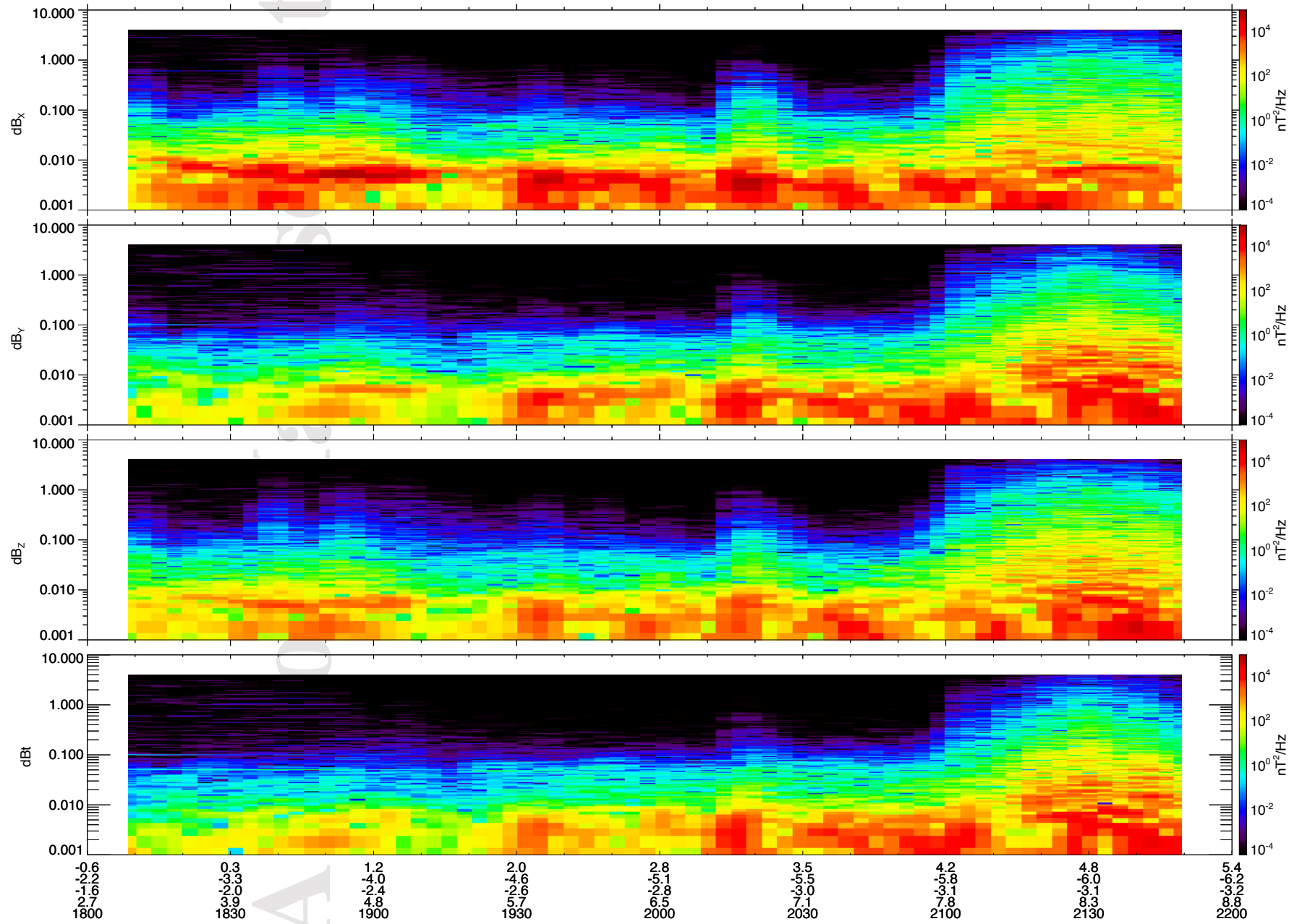




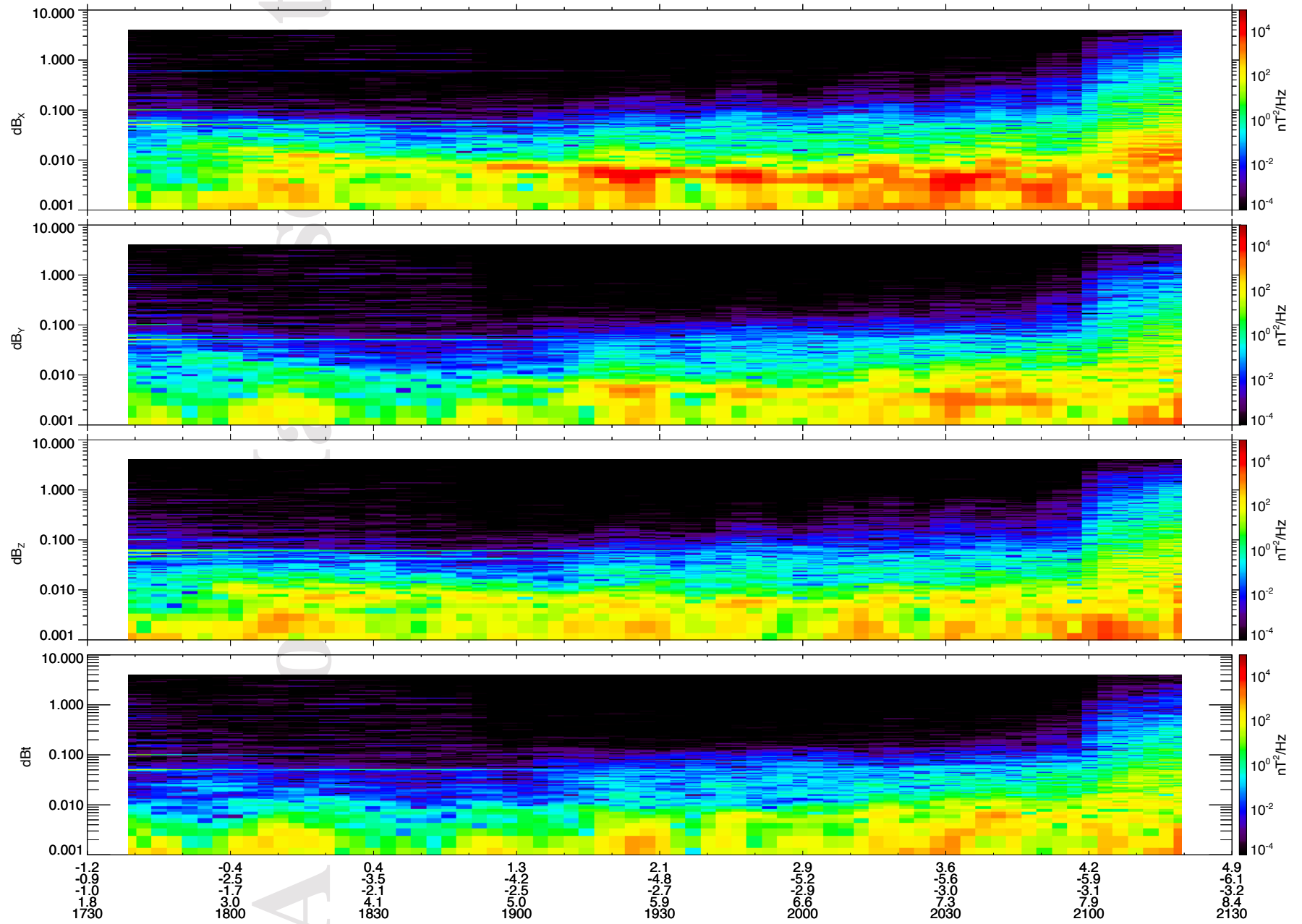
MMS1 Outbound Dynamic Power Spectrum 2017-01-30



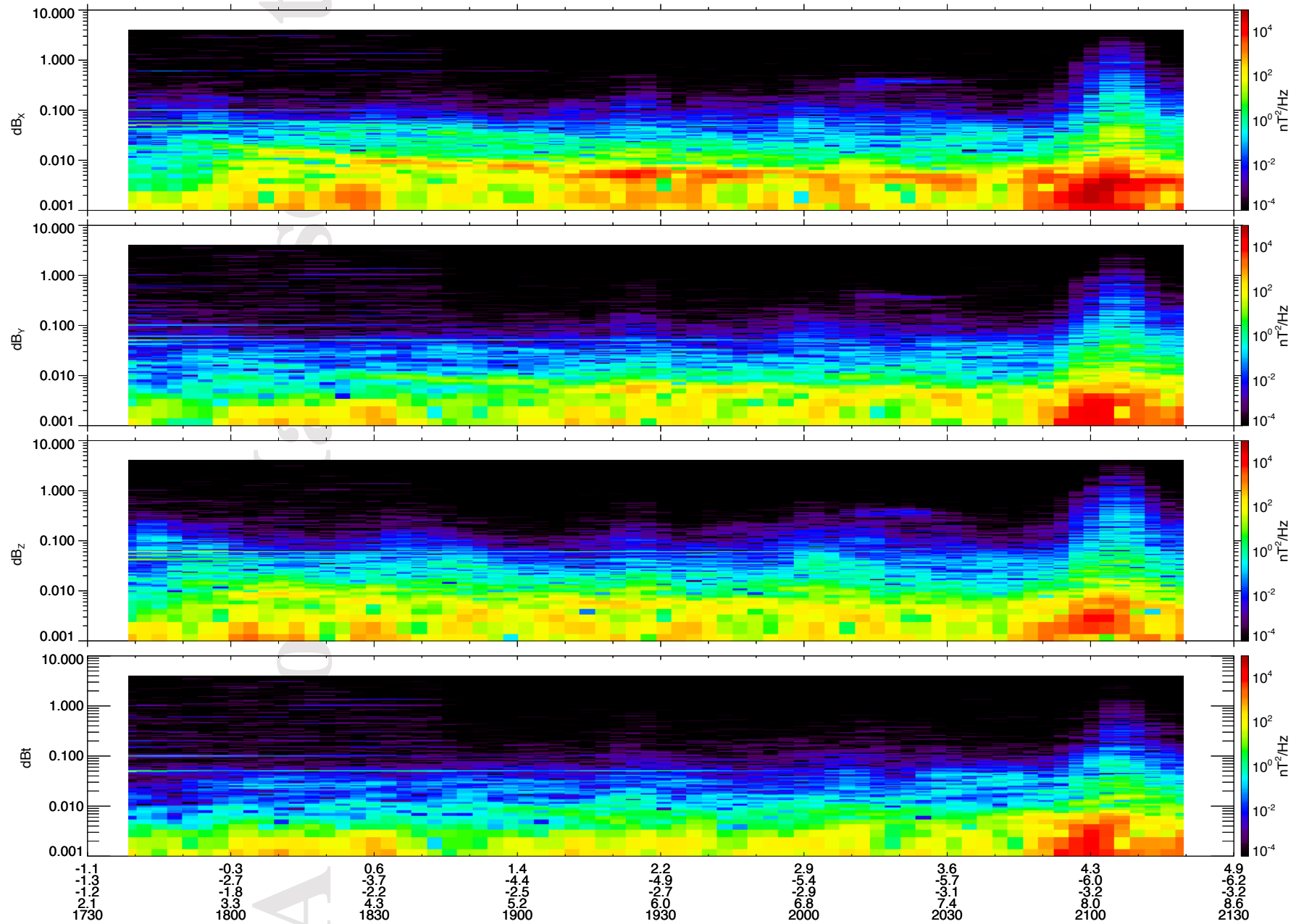
MMS1 Outbound Dynamic Power Spectrum 2017-01-31



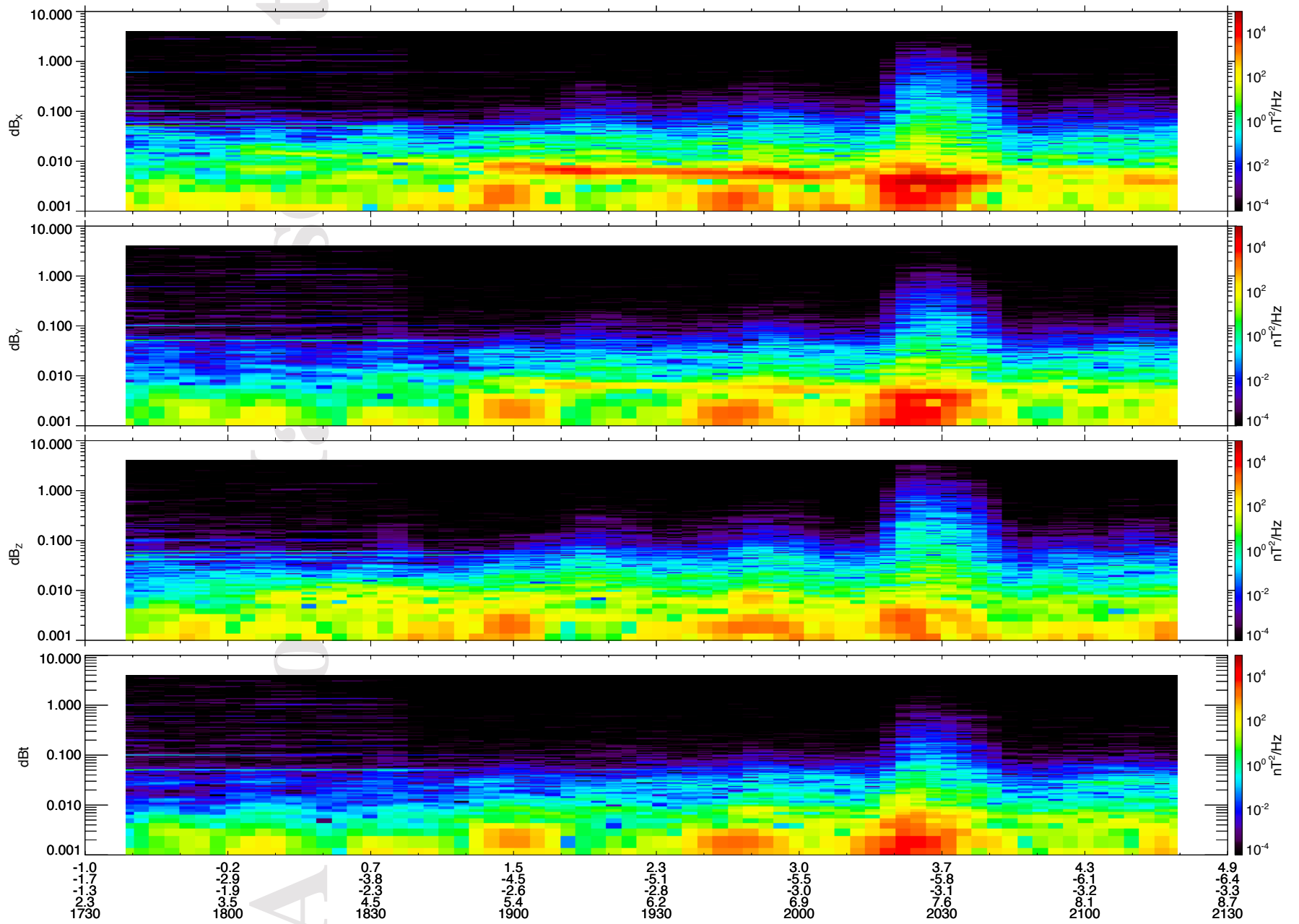
MMS1 Outbound Dynamic Power Spectrum 2017-02-01



MMS1 Outbound Dynamic Power Spectrum 2017-02-02



MMS1 Outbound Dynamic Power Spectrum 2017-02-03



MMS1 Outbound Dynamic Power Spectrum 2017-02-04

